

Martijn Asschert

Groundwater and solute transport modelling study Vosdonk Noord at Etten-Leur

Examining the effect of two implementation methodologies for highly heterogenic subsurface characteristics



AFVALZORG



This Page is Intentionally Left Blank

Groundwater and solute transport modelling study Vosdonk Noord at Etten-Leur

*Examining the effect of two implementation methodologies for highly
heterogenic shallow subsurface characteristics*

By

Martijn Asschert

In partial fulfilment of the requirements for the degree of

Master of Science
in Geo-Engineering

at the Delft University of Technology
to be defended publicly on Wednesday, September 13, 2017

Head Supervisor:	Prof. Dr. Ir. T.J. Heimovaara	TU Delft
Thesis committee:	Prof. Dr. Ir. M. Bakker	TU Delft
	Dr. Ir. J. Gebert	TU Delft
	Ir. J.B.M. van Bommel	Orvion BV
	Ir. P. Assenberg	Afvalzorg

An electronic version of this thesis is available at <http://repository.tudelft.nl/>



AFVALZORG



This Page is Intentionally Left Blank

Abstract

The industrial site of Vosdonk Noord at Etten-Leur in the Netherlands consists of a large soil contamination in combination with highly heterogenic shallow subsurface soil characteristics. In this report, we study the groundwater flow and solute transport behaviour at this project location. Throughout this process, knowledge is gathered about the interpretation of the shallow subsurface heterogeneity with a main focus on the hydraulic conductivities. It is interesting to look at the subsurface heterogeneity because of the challenge to implement it inside a model and its uncertainty in characteristics. This means the subsurface heterogeneity is part of the problem to be solved. All the components of the problem led to the following main research question: *“What is the future behaviour of the contaminated groundwater by approaching the problem with acceptable simplification and maintaining the reliability of results?”*.

A comparison of groundwater flow and solute transport results were made using kriging as an interpolation method to implement subsurface cone penetration test data directly into the model. This generated a cell by cell implementation of the subsurface characteristics. To include the possible variability of the subsurface and to increase the reliability of the results, random simulations were implemented. In practice, the “pancake” method characterises the subsurface in a commercial software like Visual Modflow. This “pancake” method uses continuous horizontal subsurface soil layers. The gathered knowledge is useful to try and tackle the in practice used “pancake” method in case of a highly heterogenic subsurface.

The difference in implementation of the subsurface heterogeneity creates a clear difference in effects on the behaviour of groundwater flow and solute transport. The most important result consists of the high and low hydraulic conductivity regions in the subsurface arising from the kriging methodology, which causes one big open top aquifer. This creates the possibility for the flow to move around the impermeable spots, which is not possible for the “pancake” implementation. These differences also resulted in large differences in the output of the solute transport between the two methodologies.

Apart from the large differences between the two implementation methods, the contaminant cis-1,2-di-chloroethene needs further evaluation. The given output values of the solute transport are uncertain because a highly simplified 1D solute transport model was used. Nevertheless, it gives an acceptable first indication on the behaviour of the contaminants. This meant high concentrations and low decay properties prevent the environment from naturally attenuating cis-1,2-di-chloroethene.

The main points of discussion in this research are the highly simplified solute transport model, the insensitive behaviour of the hydraulic conductivity and the low number of random simulations. These last two could influence the greatness of difference between the “pancake” and kriging implementation methodology. Additional research and a validation of the kriging methodology on the project location are necessary to make improvements on the results of this research .

This Page is Intentionally Left Blank

Acknowledgements

I would like to thank Orvion BV and Afvalzorg for making it possible to carry out my Master Thesis on this interesting project. The working environment within Orvion BV has been great and the interaction with Afvalzorg has always been positive.

In specific I would like to thank my daily supervisor at Orvion BV, Marc van Bommel, for his guidance and advice during the research. Also, big thanks to my main supervisor from Afvalzorg, Peter Assenberg, for the positive responses on my delivered work.

I would also like to thank my chair supervisor from the university, Prof.Timo Heimovaara, for helping me during each stage of this Master Thesis project. I am thankful to him for providing me with valuable suggestion and comments. I also appreciate the feedback obtained during the writing of this thesis work.

Moreover, I would like to thank my other thesis committee members, Prof.Mark Bakker and Dr.Julia Gebert, for taking part in my committee and providing me with feedback on my report.

Also, a word of thanks to Waterschap Brabantse Delta, the company Brabant Water and the municipality of Etten-Leur for the easy accessibility to their data sources. Without this data, the research would have been of a considerable smaller quality.

A special gratitude to my fellow students from Geo-Engineering for a great time during the Master Thesis and the helpful mindset in study rooms.

Finally, I must express my gratitude to my family and friends for supporting me throughout the complete time of the Master Thesis.

Martijn Asschert
Delft, September 2017

This Page is Intentionally Left Blank

Table of Contents

Abbreviation list	1
List of Figures	2
List of Tables.....	4
1 Introduction	5
1.1 Background.....	5
1.2 Thesis Statement	7
1.2.1 Goals.....	7
1.2.2 Research questions	7
1.2.3 Hypothesis.....	7
1.3 Project location.....	8
2 Theory	9
2.1 General groundwater flow and solute transport governing equations	9
2.2 The advection-dispersion equation	10
2.3 Geostatistics: simple, ordinary and universal kriging	11
2.4 The volatile organochlorines	13
2.5 Cone penetration testing.....	14
3 Materials and Methods.....	15
3.1 Implementing heterogeneity by box model subsurface alternatives	15
3.1.1 Constructed alternatives including layer specification parameters.....	16
3.1.2 Box modelling properties	17
3.2 Preparing groundwater model zero and upscaling of the sample data	17
3.3 Conditional simulations including the heterogenic subsurface variability.....	18
3.4 Kriging.....	20
3.4.1 Finding the most suitable type of Kriging: Simple, Ordinary or Universal Kriging	20
3.4.2 The Kriging semivariograms	21
3.4.3 The kriging calibration.....	22
3.5 Importing the kriging datasets and generating flow lines.....	23
3.6 1D solute transport MATLAB model.....	24
3.6.1 Application	24
3.6.2 Add-on for the step by step degradation of the chlorinated solvents.....	25
3.6.3 Boundary condition	25
3.6.4 Managing the exported data of the flow line	25
3.6.5 The characteristics of the contamination	26
3.7 Overview of the conducted simulations.....	28
4 Results & Discussion	29

4.1	Kriging	29
4.2	Groundwater Flow Behaviour	31
4.3	1D Solute Transport.....	34
4.3.1	Flowline locations: flowline behaviour of the random simulations	34
4.3.2	Solute Transport: examining objects.....	35
4.3.3	Solute transport concentration evolution over time	38
4.3.4	Probability curves of the contaminants travelled distances	40
4.4	General points of discussion.....	42
5	Conclusion & Recommendations	43
6	Bibliography	45
Appendix A - Groundwater model zero		49
A.1	Model Objectives.....	49
A.2	Hydrogeological Characterization	49
A.3	Model Conceptualization.....	51
A.4	Modelling Software Selection.....	53
A.5	Model Design.....	53
A.5.1	Model grid	53
A.5.2	Boundary conditions	54
A.5.3	Subsurface parameters	56
A.5.4	Ground and layering height levels	58
A.5.5	Extraction well's transient schedules.....	58
A.6	Model Calibration	59
A.7	Model Verification and future monitoring	61
A.8	Groundwater model zero resulting layer overview.....	61
Appendix B - Box model alternatives		77
Appendix C - Alternative scenario variability quantification.....		80
Appendix D - The Kriging Calibration Figures		81
D.1	Horizontal Hydraulic Conductivity	81
D.2	Vertical Hydraulic Conductivity	81
D.3	Porosity.....	82
D.4	Effective Porosity	82
Appendix E - Orvion assessment of biological degradation constants		83
Appendix F - Matlab Scripts		88
F.1	DataPrep_Random script.....	88
F.2	Kriging_VisualPrep_Layer1 script	92
F.3	Flowdata_ran function	94
F.4	Flowline1_RandomSimu script	95

Abbreviation list

<i>PER</i>	= Tetrachloroethene
<i>CIS</i>	= Cis-1,2-di-chloroethene
<i>TRI</i>	= Trichloroethene
<i>VC</i>	= Vinyl chloride
<i>ET</i>	= Ethene
<i>VOCL</i>	= Volatile organochlorines
<i>K_V</i>	= Vertical hydraulic conductivity
<i>K_H</i>	= Horizontal hydraulic conductivity
<i>Por.</i>	= Porosity
<i>Eff. Por.</i>	= Effective porosity
<i>Krig Min</i>	= Kriging simulation with the full horizontal length of impermeable layers in the box model
<i>Krig Max</i>	= Kriging simulation with the 10-meter horizontal length of the impermeable layers in the box model
<i>Groundwater Model zero</i>	= Initial constant layered groundwater model as presented in Appendix A
<i>Model Krig</i>	= Groundwater model including the kriging implementation
<i>N.A.P.</i>	= Normaal Amsterdams Peil or Amsterdam ordnance datum, which refers to the dutch reference height
<i>CPT</i>	= Cone penetration test

List of Figures

Figure 1: Project location, 1 centimeter = 2.5 kilometers (Google, 2017).	8
Figure 2: Overview of the main components at the project location (Arcadis, 2012).	8
Figure 3: Typical semivariogram (Samui & Sitharam, 2011).	12
Figure 4: Volatile organochlorines tree (Ellis & Anderson, 2017).	13
Figure 5: Simplified soil behaviour type classification for a standard friction cone (Robertson, 1990).	14
Figure 6: Robertson Diagram (Edelman, 2016).	15
Figure 7: Schematic of one box model cell for a horizontal situation.	17
Figure 8: Overview of the location of the kriging implementation.	18
Figure 9: Map with the CPT data locations.	18
Figure 10: Variability of the Nuenen Group from 0 to -10 m (left) and -10 to -20 m (right) depth N.A.P. (van Alphen, 1984, pp. 38-39).	19
Figure 11: Example of a section view on the minimum (left) and maximum (right) limits of hydraulic conductivity and porosity for a box model in Visual Modflow.	19
Figure 12: Semivariograms of a) Vertical hydraulic conductivity, b) Horizontal hydraulic conductivity, c) Effective porosity and d) Porosity.	21
Figure 13: Calibration results of the horizontal hydraulic conductivity.	22
Figure 14: Location Flowline starting points.	23
Figure 15: Ghost node overview for the Neumann boundary condition.	25
Figure 16: Hydraulic conductivities kriging results with a) Kz min left and Kz max right and b) Kxy min left and Kxy max right. The dots represent the CPT sample data points, X and Y are the coordinate locations in meters and the depth is in N.A.P.	29
Figure 17: Kriging results of a) Two random simulation outputs for Kz b) Porosity and c) Effective Porosity. The dots represent the CPT sample data points, X and Y are the coordinate locations in meters and the depth is in N.A.P.	30
Figure 18: Top view on the groundwater flow with a) and b) layer 1 (Ground level) behaviour of respectively model zero and Krig min and c) and d) layer 5 of respectively Model zero (-10 m N.A.P.) and Krig min (-20 m N.A.P.).	31
Figure 19: For groundwater model zero, layer 10 (-50 m N.A.P.) in a) presents more or less north direction of groundwater flow direction and b) layer 14 (-145 m N.A.P.) presents north western direction of flow.	32
Figure 20: Section view groundwater particle behaviour model zero.	32
Figure 21: Section view of the groundwater flow particle behaviour of the shallow subsurface layers.	32
Figure 22: Top view on the flowlines from the random simulations.	34
Figure 23: Top view of the behaviour for Flowline 1 and 2 in a) Model zero, b) Krig Min and c) Krig max. Marker = 1 year elapsed time.	35
Figure 24: Section view for Flowline 1 and 2 in a) Model zero, b) Krig Min and c) Krig max. Marker = 1-year elapsed time.	35
Figure 25: Flowline 1 object examination with a) the river Laaksche Vaart and b) the specified 175 m distance on the path.	36
Figure 26: Flowline 2 object examination for a 100-meter path distance.	37
Figure 27: Zoom in on the behaviour of vinyl chloride and ethene.	37
Figure 28: Flowline 1 concentration time steps over the distance for a) kriging models and b) model zero.	38

Figure 29: Flowline 2 concentration time steps over the distance for a) kriging models and b) model zero.....	39
Figure 30: Probability curves of travelled distance for a) flowline 1 and b) flowline 2.....	41
Figure 31: Example of the map with isohypsen in the first subsurface layer from data of the Brabant model.....	49
Figure 32: Subsurface material layering characteristics at the industrial area and the drinking water extractions at Seppe.....	52
Figure 33: Conceptual top view model.	53
Figure 34: River data point locations for implementation in Visual Modflow.	54
Figure 35: Recharge boundary zones with classification.	55
Figure 36: Section view with class colouring of the hydraulic conductivities.	57
Figure 37: Section view with class colouring of the Porosity and Effective Porosity.	57
Figure 38: AHN ground level data map (AHN, 2017).....	58
Figure 39: Drink water and Industry extraction well schedules.....	59
Figure 40: Calibration results for groundwater model zero.....	59
Figure 41: Model validation results. With a) for the year 2015 and b) for the year 2014.	61
Figure 42: Validation 2015 outlier.....	61
Figure 43: Groundwater model zero Layer 1 in 2016.....	62
Figure 44: Groundwater model zero Layer 2 in 2016.....	63
Figure 45: Groundwater model zero Layer 3 in 2016.....	64
Figure 46: Groundwater model zero Layer 4 in 2016.....	65
Figure 47: Groundwater model zero Layer 5 in 2016.....	66
Figure 48: Groundwater model zero Layer 6 in 2016.....	67
Figure 49: Groundwater model zero Layer 7 in 2016.....	68
Figure 50: Groundwater model zero Layer 8 in 2016.....	69
Figure 51: Groundwater model zero Layer 9 in 2016.....	70
Figure 52: Groundwater model zero Layer 10 in 2016.	71
Figure 53: Groundwater model zero Layer 11 in 2016.	72
Figure 54: Groundwater model zero Layer 12 in 2016.	73
Figure 55: Groundwater model zero Layer 13 in 2016.	74
Figure 56: Groundwater model zero Layer 14 in 2016.	75
Figure 57: Groundwater model zero Layer 15 in 2016.	76
Figure 58: Horizontal hydraulic conductivity kriging calibration.....	81
Figure 59: Vertical hydraulic conductivity kriging calibration.....	81
Figure 60: Porosity kriging calibration.....	82
Figure 61: Effective porosity kriging calibration.....	82

List of Tables

Table 1: Example of one of the box model alternatives with the thicknesses in meters.	16
Table 2: Resulting parameter values of the subsurface groups.	16
Table 3: Semivariogram parameter properties.	21
Table 4: Decay coefficients.	26
Table 5: Parameter values for and calculation of the retardation coefficient.	27
Table 6: Initial concentrations at the start time and location of the flowlines.	27
Table 7: calibration results 1D solute transport model.	27
Table 8: Initial and calibrated parameter results for the retardation and decay coefficients.	28
Table 9: Usable observation points of hydraulic head in 2014, 2015 and 2016.	51
Table 10: Parameter properties of the river boundary condition.	55
Table 11: Subsurface parameter values of the present formations in the model.	56
Table 12: Initial subsurface parameter values.	57
Table 13: Active years of the industrial extraction wells.	59
Table 14: Subsurface parameter values after model calibration.	60
Table 15: Recharge class values after model calibration. Class locations presented in Figure 35.	60
Table 16: Box model alternative 1 to 5.	77
Table 17: Box model alternative 6 to 10.	77
Table 18: Box model alternative 11 to 15.	78
Table 19: Box model alternative 16 to 20.	78
Table 20: Box model alternative 21 to 25.	79
Table 21: Box model alternative 26 to 30.	79
Table 22: Alternative minimum and maximum scenario variability quantification.	80

1 Introduction

1.1 Background

The company site Vosdonk-Noord at Etten-Leur in the Netherlands has been contaminated due to historical industrial activities from the 1950's and onwards. It consists of a large size soil contamination originating from five source zones present in the groundwater below the company site. The main components of the contamination can be described as volatile organochlorines characterised by tetrachloroethene, trichloroethene, cis-1,2-di-chloroethene and vinyl-chlorides (Arcadis, 2012). Groundwater is extracted for drinking water purposes at a 3.6-kilometer distance from the contaminated subsurface. It is important to get insights into the spreading behaviour of the contaminants to prevent the drinking water extraction wells from being contaminated. Industrial groundwater extractions have taken place in the past. Over the years they have been terminated or decreased in capacity. These changes can contribute to a change in the behaviour of the groundwater. The composition of the subsurface can be another influencing factor. Arcadis (2012) explains the presence of the highly heterogenic Nuenen Group in the upper range of the subsurface. This indicates a high variability in clayey and sandy subsurface areas. A modelling study shall be conducted to get insights into the behaviour of the contamination plume.

Van Alphen (1984) explains the heterogeneity of the Nuenen group as a wide variety of soil layer types over short distances in the shallow subsurface. For example, a number of small clay layers or spots are present inside a sandy soil layer. This high variety influences the permeability, which describes a measure of resistance affecting the groundwater flow moving through the subsurface. Most of the contamination is present in the upper layers and so Nuenen group. This volatile organochlorine contamination can create problems for the drinking water extractions at Seppe and the areas in and around Etten-Leur. If these locations are reached, the contaminant components have the potential to pollute them. For example, the drinking water would be no longer suitable for use (Arcadis, 2012). In some groundwater these kind of contaminations can be naturally attenuated. Ellis and Anderson (2017) explain the possibility for microbial degradation, which means the contaminant components undergo reductive dechlorination catalyzed by anaerobic bacteria. This results in a reduction of contamination concentrations, but is a time consuming process.

Numerical modelling has emerged as an effective tool for managing groundwater resources and predicting future responses, especially when dealing with complex aquifers systems and heterogeneous formations (Abu-El-Sha'r & Hatamleh, 2007). The possibility to create groundwater and solute transport models arises with the help of this numerical modelling. Kumar (2013) explains that these models provide additional insights into the complex system behaviour and can assist in developing conceptual understanding. They have been demonstrated to reasonably reproduce past behaviour, support decision-making and allow for the exploration of alternative management approaches (Kumar, 2013). The rise of these models resulted in different groundwater modelling codes. Each code has his capabilities, characteristics and limitations, which is important to realise. This is confirmed by Kumar (2012). He mentioned that it is important to determine if a particular code is appropriate or able to perform the simulations required for the project.

MODFLOW and MT3D are the most commonly used simulators for modelling groundwater flow and solute transport in the subsurface systems, respectively (Abu-El-Sha'r & Hatamleh, 2007) (Saba, Umar, & Ahmed, 2016) (Tamma Rao, Gurunadha Rao, Surinaidu, Mahesh, & Padalu, 2011). MODFLOW is a three-dimensional finite-difference groundwater flow simulator published in 1984, where MODFLOW-2005 is the most current release (Harbaugh, 2005). MT3D is a three-dimensional solute transport simulator, able to solve advection, dispersion, and chemical reactions of contaminants in saturated

groundwater flow systems (USGS, 2016). Both simulators are used widely in combination with each other, because of their good compatibility. Commercial interfaces like Visual Modflow and Groundwater Vistas are developed around these simulators to make them more applicable and easier to use for consultants.

Modelling is an effective tool to predict the future, but it is not able to predict the circumstances of solute transport and groundwater flow perfectly. Points of uncertainty are always present. The sources of uncertainty in numerical simulations of groundwater flow can be divided into model parameters, the conceptual model and observation data according to the process of system simulation (Zeng & Wu, 2013). In some way, the predictions of groundwater and solute transport systems do always deviate from observations. Kumar (2012) states an extra lack of flexibility in the input data can arise for the commercial interfaces of MODFLOW. For example in the spatial distributions of aquifer geometry and hydraulic parameters. When creating the conceptual model, checking parameter uncertainty and especially evaluating the uncertainty and so correctness of the outputs, it is important to keep this kind of situations in mind. Gaganis & Smith (2005) mentioned another important statement about the conceptual model. Errors in the model structure, although having a significant impact, cannot be avoided because they arise from our limited capability to exactly describe the complexity of a physical system. The overall challenge considering the uncertainties is to try and reach a result as close to reality as possible with the tools available.

The importance and considerable impact of respectively the hydraulic conductivity and (rainfall) recharge on groundwater flow and solute transport models was noticed in multiple case studies (Saba, Umar, & Ahmed, 2016) (Abu-El-Sha'r & Hatamleh, 2007) (Petitta, et al., 2013) (Mondal, Singh, & Sankaran, 2011). Wang and Huang (2011) and Elfeki, Uffink and Lebreton (2011) verify the importance of especially the hydraulic conductivity. They show that the solute transport process and the contaminant plume shape is highly dependent on the (spatial) heterogeneity of the hydraulic conductivity field. Dagan, as cited in Wang & Huang (2011), states that the stochastic methods are developed and used to deal with these difficulties. Arcadis (2012) explains that multiple different layers of varying hydraulic conductivities are present at the project location. These layers are not always present with clear boundaries in the subsurface. The sensitivity of the mentioned parameters implies the need for extra attention and maybe even extra measures to deal with these uncertainties as good as possible. The need for careful aquifer characterization is represented to be able to accurately estimate or predict the subsurface groundwater flow or solute transport.

In this kind of research, methods to conduct a stochastic approach are called geostatistics. Geostatistics refers to a set of statistical procedures for describing the correlation of spatially distributed random variables and for performing interpolation and a real estimation of these variables (Cooper & Istok, 1988). Geostatistics can be applied to a wide range of fields situated mainly in the geography branch. Kriging is commonly used for soil properties looking at for example Daya and Bejari (2015), Marache et al. (2009) and Webster and Burgess (1980). Kriging is an approximation method that can give predictions of unknown values of a random function, random field, or random process and is called an interpolation technique developed by a mining engineer (van Beers & Kleijnen, 2010).

1.2 Thesis Statement

The thesis statement includes the goals of the research and formulation of the research questions following the background and project location. These capture the essence of the project and set the scope of the research.

1.2.1 Goals

The main goal of this research is to predict the behaviour of the large-scale groundwater contaminant plume and to obtain insights into the effects of the highly heterogeneous subsurface on the spreading of the contaminant plume at the project location.

To reach this main goal, these subordinate goals have to be accomplished:

- *To set up and calibrate a groundwater model including transport and biodegradation of contaminants.*
- *To calculate the long-term effect of the recent termination of industrial groundwater extractions.*
- *To establish the kinetics of naturally occurring and stimulated biodegradation processes and incorporate these processes into the groundwater models.*
- *To get insights into the long-term effect of a “natural attenuation scenario” and determine possibly needed source removal in relation to the plume length and plume behaviour.*
- *Identify the effect of the spatial variations due to soil heterogeneity on long-term plume behaviour.*

1.2.2 Research questions

Main question:

What is the future behaviour of the contaminated groundwater by approaching the problem with acceptable simplification and maintaining the reliability of results?

Sub questions

1. *What is the groundwater flow behaviour in and around the area Vosdonk-Noord at Etten-Leur using the measurement and extraction data available?*
2. *How can the spatial variations in the subsurface hydraulic conductivities be translated into the model?*
3. *How can multiple scenarios of the subsurface be created and implemented to improve the reliability of the results?*
4. *What are the characteristics of the chlorinated solvent contamination at the project location?*
5. *What long term impact do the recent terminations of the industrial groundwater extractions have on the groundwater patterns and contamination plume?*
6. *How does the contaminant plume behave applying the natural attenuation scenario and which man-made attenuation or source removal could be necessary?*

1.2.3 Hypothesis

The challenge of research like this is that there is never enough detailed information available. The hypothesis is stated as follows: *“Although the lack of detailed information much knowledge can be gathered in the process of generating multiple stochastic “supported” scenarios of the subsurface and using all these individual scenarios in the models to create reliability in the results”*. This makes it possible to assign a probability to each scenario and estimate the possible outcome, resulting in a stochastic approach to predict future behaviour of the contamination. In the end, there is expected to be able to construct probability based conclusions and conduct probability based decisions

1.3 Project location

The project location is located in the Netherlands around Etten-Leur at the industrial site Vosdonk and used to conduct the research. In specific Vosdonk-Noord is the area to be investigated. Etten-Leur is located between the cities Breda and Roosendaal. They are dependent on the drinking water extracted at Seppe. The extraction area from Seppe is located 3.6 kilometres to the west of Vosdonk Noord, just above the Breda International Airport. Figure 1 presents an overview.

The estimated contaminated area is located in the southern part of Vosdonk Noord. In Figure 2 a more detailed overview of the project location is displayed. A 25 year-zone is presented to the left of the company site in between the drink water extraction area of Seppe, indicated with light blue, and the small village Hoeven. The requirement is that contaminant cannot be near this zone within 25 years counting from 2016. The company Afvalzorg is responsible for meeting this requirement. Afvalzorg has been assigned the responsibility for the contamination at the project location by the government of the Netherlands, which means they have to take measures if needed. Orvion BV is specialised in microbiological detection methods and are able to deliver solutions for purifying soil and water. They are also able to give advice on groundwater flow and solute transport problems.

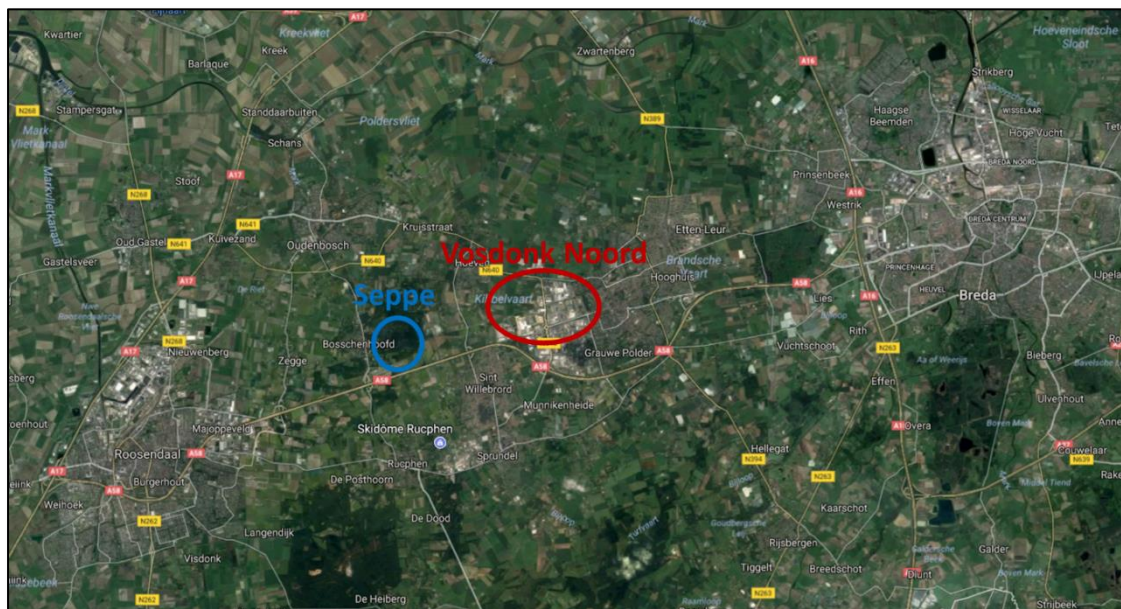


Figure 1: Project location, 1 centimeter = 2.5 kilometers (Google, 2017).

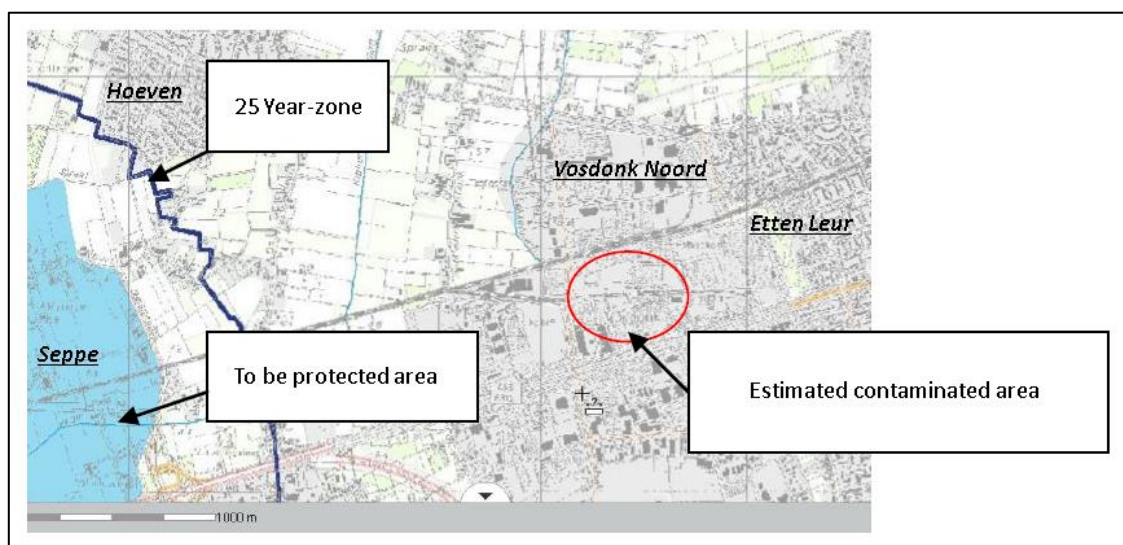


Figure 2: Overview of the main components at the project location (Arcadis, 2012).

2 Theory

2.1 General groundwater flow and solute transport governing equations

The three-dimensional governing equations for groundwater flow and solute transport are used for the calculations in the modelling software. The general form of these governing equations is given by Freeze & Cherry (1979) and can be described as in Equation 1 and 3. The general governing equation for groundwater transport is given in Equation 1.

$$\frac{\partial}{\partial x} \left(Kx \frac{\partial h}{\partial x} \right) + \frac{\partial}{\partial y} \left(Ky \frac{\partial h}{\partial y} \right) + \frac{\partial}{\partial z} \left(Kz \frac{\partial h}{\partial z} \right) - w = Ss \frac{\partial h}{\partial t} \quad (1)$$

$$\frac{\partial}{\partial x} \left(Kx \frac{\partial h}{\partial x} \right) + \frac{\partial}{\partial y} \left(Ky \frac{\partial h}{\partial y} \right) + \frac{\partial}{\partial z} \left(Kz \frac{\partial h}{\partial z} \right) - w = 0.0 \quad (2)$$

- Kx, Ky, Kz = values of hydraulic conductivity along the x, y and z coordinate axes (L/t)
 h = is the potentiometric head (L); w : is the volumetric flux per unit volume and represents sources and/or sinks of water per unit time (t^{-1})
 Ss = is the specific storage of the porous material (L^{-1})
 t = is time (t)

Setting the right part of Equation 1 to zero achieves a steady state situation. This is presented in Equation 2. With Equation 2 the transmissivities can be calculated. The transient state can be solved by using the calculated transmissivities and right part of the Equation 1, whereafter solving it for the storage coefficients (Abu-El-Sha'r & Hatamleh, 2007).

Equation 3 gives the partial differential equation for three-dimensional transport of contaminants in groundwater (Freeze & Cherry, 1979).

$$\frac{\partial C}{\partial t} = \frac{\partial}{\partial x_i} \left[D_{ij} \frac{\partial C}{\partial x_j} \right] - \frac{\partial}{\partial x_i} (v_i C) + \frac{q_s}{\theta} C_s + \sum_{k=1}^N R_s \quad (3)$$

- C = the concentration of contaminant dissolved in groundwater
 x_i = the distance along the respective Cartesian co-ordinate axis
 D_{ij} = the hydrodynamic dispersion coefficient
 t = is time (t)
 v_i = the seepage or linear pore water velocity
 q_s = the volumetric flux of water per unit volume of aquifer representing sources (positive) and sinks (negative)
 C_s = the concentration of the sources or the sinks
 θ = the porosity of the porous medium
 R_s = chemical reaction term

The governing equation for the transport model describes the transient changes of the solute concentration in the groundwater. To be able to obtain this solution an initial condition is necessary. Equation 4 presents the initial condition, where $c_0(x,y,z)$ is a known concentration distribution and Ω indicates the entire model domain (Zheng & Wang, 1999).

$$C(x, y, z, t) = c_0(x, y, z) \text{ on } \Omega; t = 0 \quad (4)$$

To solve the governing solute and transport equations a specification of the boundary condition is required. Zheng and Wang (1999) give the three general types of boundary conditions. These include

the Dirichlet condition, Neumann condition and a combination of the two called the Cauchy condition. They are given in respectively Equation 5, 6 and 7. The Γ denotes the specified concentration boundary, $f_i(x,y,z,t)$ is a known function representing the dispersive flux normal to the boundary Γ and $g_i(x,y,z,t)$ represents a known function for the total flux normal to the boundary Γ . Dirichlet handles the concentration known along the boundary, Neumann handles the concentration gradient known across the boundary and Cauchy specifies both.

$$C(x, y, z, t) = c(x, y, z, t) \text{ on } \Gamma_1 ; t \geq 0 \quad (5)$$

$$\theta D_{ij} \frac{\partial C}{\partial x_j} = f_i(x, y, z, t) \text{ on } \Gamma_2 ; t \geq 0 \quad (6)$$

$$\theta D_{ij} \frac{\partial C}{\partial x_j} - q_i C = g_i(x, y, z, t) \text{ on } \Gamma_3 ; t \geq 0 \quad (7)$$

2.2 The advection-dispersion equation

The advection-dispersion equation presented in Equation 3 consists of a couple of different terms. The main components are the advection term of Equation 8 and the dispersion term presented in Equation 9. Advection describes the transport of the miscible contaminants at the same velocity as the groundwater, where the dispersion is defined as the spreading of contaminants over a greater region than would be predicted solely from the average groundwater velocity vectors (Zheng & Wang, 1999).

$$\text{Advection term} = \frac{\partial}{\partial x_i} (v_i C) \quad (8)$$

$$\text{Dispersion term} = \frac{\partial}{\partial x_i} \left[D_{ij} \frac{\partial C}{\partial x_j} \right] \quad (9)$$

Assuming a 1D steady state condition for the transport equation from Equation 3, results in a reduced transport equation given in Equation 10. This is presented in van Genuchten and Alves (1982) given that the steady state implies the volumetric moisture content and the volumetric flux remaining constant in time and space. Retardation, first order decay and zero order production are present besides the presence of advection and dispersion. Retardation includes the rate of solution velocity to the contaminant velocity. The μ and γ term can simply be crossed out in case no first order decay or zero-order production are present, which results in Equation 11.

$$D \frac{\partial^2 c}{\partial x^2} - v \frac{\partial c}{\partial x} - R \frac{\partial c}{\partial t} = \mu c - \gamma \quad (10)$$

$$R \frac{\partial c}{\partial t} = D \frac{\partial^2 c}{\partial x^2} - v \frac{\partial c}{\partial x} \quad (11)$$

Where:

- D = Dispersion coefficient (L^2/T)
- c = Solution concentration (M/L^3)
- x = Distance (L)
- v = Pore-water velocity and in the model the average linear (seepage) velocity (L/T)
- R = Retardation factor (-)
- t = Time (T)
- μ = Rate constant for first-order decay in the liquid and solid phases of the soil ($1/T$)
- γ = Rate constant for zero-order production in the liquid and solid phases of the soil ($M/L^3 T$)

The dispersion term is complex and consists of a mechanical and molecular component. The mechanical dispersion acts on a microscopic scale and results of the deviated velocity from the average groundwater velocity. These deviated velocities arise due to two factors. The groundwater flow is faster in the centre of the pore space, compared to the flow close to the wall of the grain particles. Secondly, differences in a path around the individual grains result in variations of groundwater flow velocities. Molecular diffusion can be included in addition to these two factors. It presents the mixing occurring due to the random motion of the molecules present in the fluid. This molecular diffusion happens when species move from higher to lower concentrations and is influenced by the tortuosity in the porous medium. The two fundamental processes for modelling dispersion includes the effects of mechanical dispersion and molecular diffusion (Anderson, 1984) (Fitts, 2013).

Advection tends to disperse mass in the process of transferring it from one to another location. Different directions of dispersion arise due to the variation in flow velocity. This variation can be divided in the longitudinal and transverse direction. For example, only longitudinal spreading arises for perfect steady laminar groundwater flows. In practice, the solute transport consists of transient variations of velocity and molecular diffusion contributing to the transverse spreading. Advection in combination with dispersion causes spreading of a solute plume in all three dimensions (Fitts, 2013).

Heimovaara, Keijzer, and Velstra (2004) found that for their 1D solute transport model, using the advection-dispersion equation, the dispersion parameter showed more or less trivial behaviour. The research consisted of a couple of assumptions. The solute transport was assumed to occur along the streamlines in a large-scale groundwater model. Also, a limited number of sources were assumed. The dispersion turned out to have trivial behaviour, after optimising the parameters with a limited data set. Not enough data was available to quantify the dispersion parameter. The governing equation is further simplified by leaving out the complex dispersion term, because of similarities in the 1D solute transport approach and data availability for this research.

The decay, μ , is taken into account in the governing equation. This parameter can be implemented easily and can be quantified using literature. This results in Equation 12 for the 1D solute transport governing equation.

$$R \frac{\partial c}{\partial t} = -v \frac{\partial c}{\partial x} - \mu c \quad (12)$$

2.3 Geostatistics: simple, ordinary and universal kriging

The simple, ordinary and universal kriging methods are examined. Kriging describes an interpolation technique and makes use of a variogram to get to its results. The main idea is that during the prediction the sample points close to the point of estimation get more weight than sample points at a further distance. This results in an improved estimate. It is also called an optimal or best linear unbiased prediction, which implies there is a final unbiased estimate having a minimal error variance among the unbiased linear predictors (Lichtenstern, 2013).

Ordinary kriging estimates a constant mean value from the data used in the kriging neighbourhood, whereafter simple kriging is done with residuals from this implicitly estimated mean. Simple kriging only uses the mean from the entire data set, which results in less accurate and smoother results (Deutsch, 2002). Universal kriging uses the principles of the ordinary kriging, but makes it also possible to take into account a trend in the mean over a spatial region. For this reason, it is also called kriging in the presence of a drift (Lichtenstern, 2013). Universal kriging was developed to identify and calculate these trends in the data, which can result in a better approximation of the subsurface (Mesic Kis, 2016).

Compared to universal kriging, the ordinary kriging assumes a stationary when looking at the mean. In reality, this value varies across the subsurface and is not the same for the complete area. There is assumed that this mean can have a functional dependence on the spatial location in case of universal kriging (Kumar, as cited in Mesic Kis, 2016).

Franklin (2014) describes the full solutions of the ordinary and universal kriging equations. He presents a helpful overview of the equations with the corresponding process. Lichtenstern (2013) chapter 6, 7 and 8 gives insights into the process for the simple, ordinary and universal kriging. He describes the complete models for all three kriging methods.

The correct use of variograms is important to be able to carry out and receive reliable results with the kriging method. Gringarten and Deutsch (2003) define the variogram as the expected squared difference between two data values separated by a distance vector h , where the semivariogram $\gamma(h)$ is one half of the variogram $2\gamma(h)$. It is a measure of variability and it increases as samples become more dissimilar. The variogram is mathematically expressed in Equation 13 (Mesic Kis, 2016):

$$2\gamma(h) = \frac{1}{N(h)} \times \sum_{n=1}^{N(h)} [z_n - z_{n+h}]^2 \quad (13)$$

Where:

$N(h)$ = number of data pairs at distance “ h ” (inside the searching neighbourhood area).

z_n = value at location “ n ”.

z_{n+h} = value at location $n + h$.

In Figure 3 a semivariogram with its characteristics is presented. Several parameters define most variograms. The nugget (C_0), range (a) and the sill ($C(0)$) (MathSoft Inc., 2013):

- The nugget effect represents micro-scale variation or measurement errors. It is estimated at a value of $h = 0$ for the semivariogram function ($\gamma(h)$) as can be seen in Figure 3.
- The sill defines the variance of the random field. So the sill is $\lim_{h \rightarrow \infty} \gamma(h)$.
- The range represents the distance at which the data are no longer autocorrelated.

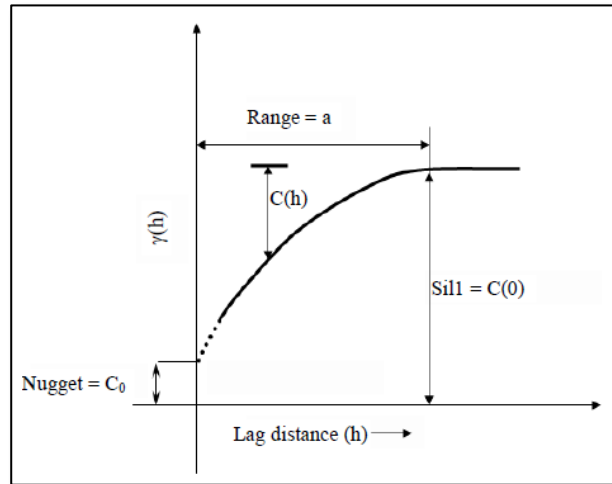


Figure 3: Typical semivariogram (Samui & Sitharam, 2011).

Samui and Sitharam (2011) describe the three elements of information the semivariograms contain. They give an autocorrelation distance that represents the radius of influence of a measurement made at a given point, provide the type of variability that indicates how values fluctuate in space and are an appreciation of dispersion of the parameters equating to the half variance. These three elements show the large influence of the semivariogram for the results of the kriging and indicate the necessity for careful implementation.

Different theoretical models are available for the semivariograms. These are the so called experimental variograms and are estimated from the data (Oliver & Webster, 2014). For example, Samui and Sitharam (2011) use the Gaussian theoretical model, as does Mesic Kis (2016), where Marache et al. (2009) develops an isotropic nested variogram implementing a nugget effect, the spherical model and an exponential model. No specific models for geological parameters are given by literature because

each data set differs. The exponential, spherical and Gaussian models are the most commonly used theoretical models for the interpretation of geological parameters and variables (Mesic Kis, 2016).

Equation 14, 15 and 16 represent the exponential, spherical and Gaussian semivariogram models respectively (Oliver & Webster, 2014).

Exponential

$$\gamma(h) = c_0 + c \left(1 - e^{-\frac{h}{a}}\right) \text{ for } h > 0 \text{ and } \gamma(h) = 0 \text{ for } h = 0 \quad (14)$$

Spherical

$$\gamma(h) = c_0 + c \left\{ \frac{3h}{2r} - \frac{1}{2} \left(\frac{h}{r}\right)^3 \right\} \text{ for } r \geq h > 0, \quad (15)$$

$$\gamma(h) = c_0 + c \text{ for } h > r \text{ and } \gamma(h) = 0 \text{ for } h = 0$$

Gaussian

$$\gamma(h) = c_0 + c \left(1 - e^{-\frac{h^2}{a^2}}\right) \text{ for } h > 0 \text{ and } \gamma(h) = 0 \text{ for } h = 0 \quad (16)$$

2.4 The volatile organochlorines

Most of the volatile organochlorines ended up into subsurface due to human activities. This happened mainly in the last century and mostly due to ignorance. In the Netherlands, around 200 different kinds of industries were found to use some sort of volatile organochlorine component. Examples are the electronical, graphical and metal industries and the production of PVC. In the last 25 years awareness and legislation have heavily restricted emission of these contaminants to the subsurface (Nipshagen & Praamstra, 2007).

When groundwater flows through a source zone with pure product of volatile organochlorines it gets contaminated. The volatile organochlorines dissolve in the groundwater. Although solubility is not high, it is considerably high compared to soil remediation standards. For example, Nipshagen and Praamstra (2007) present the tetrachloroethene standard is only 40 µg/L, but the maximum solubility of tetrachloroethene is 150.000 µg/L. The movement of volatile organochlorides is slower as the groundwater flow and is defined by retardation, dispersion and advection. This was explained in Chapter 2.2. Due to slow solubility rates, contaminant plumes can be up to multiple hundreds of meters length. This means the volatile organochlorine sources could last for hundreds of years (Nipshagen & Praamstra, 2007).

The present volatile organochlorines mentioned in Chapter 1.1 stand in relation to each other due to microbiological degradation. The individual contaminant components connect due to anaerobic degradation in the subsurface, which indicates a possibility for natural attenuation. This depends on the microbiological characteristics of the groundwater at the project location. The order of

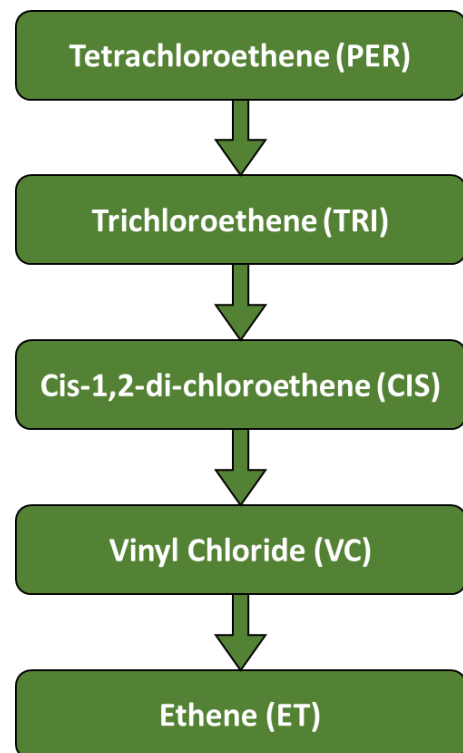


Figure 4: Volatile organochlorines tree (Ellis & Anderson, 2017).

degradation, the anaerobic volatile organochlorines tree, is given in Figure 4. The first component in the tree is tetrachloroethene, which can be used to clean electronic parts, machinery or clothing. In the industrial branch also called perchloroethene. Besides cis-1,2-di-chloroethene also a Trans-1,2-di-chloroethene type is possible within this volatile organochlorine tree (Ellis & Anderson, 2017).

The components of Figure 4 can affect the human and environmental health. The most aggressive components are trichloroethene, cis-1,2-di-chloroethene and vinyl chloride. Overconsumption of these contaminants can result in cancer in mainly the kidneys, affection of the nerve system, liver and kidney damage and lead to birth defects. High amounts even result in death. Ethene is not considered harmful to the human health and tetrachloroethene only causes minor effects like headaches or sleep problems. It is important to be careful with, in specific the middle three, components of Figure 4 in our society (ATSDR, 1996) (ATSDR, 2016) (ATSDR, 2014) (ATSDR, 2006) (ATSDR, 1990).

2.5 Cone penetration testing

Noce and Holzer (2003) explain the characteristics of cone penetration testing (CPT). A rapid exploration of shallow subsurface conditions is carried out. The depth of this exploration is mostly less than 30 meters. Retrieval of subsurface materials is minimized during the exploration of the subsurface. The CPT uses sensors, which are pushed into the ground at a slow and constant velocity. This is called the direct push method. With the use of standard engineering correlations geotechnical properties of the layers can be inferred. These correlations are based on the gathered CPT parameters, which include the friction number and the cone resistance. Robertson (1990) presents one of the most popular methods to interpret the CPT data using these two parameters. This is presented in the chart of Figure 5, which makes it possible to infer the soil behaviour type. At last, Noce and Holzer (2003) state a CPT is a reliable and efficient method for stratigraphic profiling and obtaining soil-engineering parameters for geotechnical design, as well as being widely accepted and encouraged by regulators as an effective environmental-investigation technology.

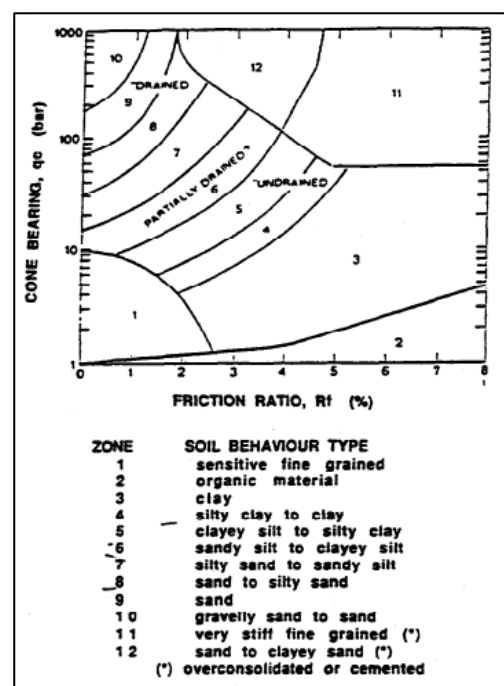


Figure 5: Simplified soil behaviour type classification for a standard friction cone (Robertson, 1990).

3 Materials and Methods

A groundwater model was constructed, calibrated and validated in advance of the conducted steps in this chapter. No suitable groundwater model was yet available for the area Vosdonk Noord at Etten-Leur. The name of this groundwater model is groundwater model zero, as it forms the basis for this and further research. Groundwater model zero is presented in Appendix A. This chapter gives a step by step explanation on how the models were constructed using the kriging.

3.1 Implementing heterogeneity by box model subsurface alternatives

Creating a method to implement the CPT data is the first step in the process. The CPT data gives detailed information on the soil type of the small vertical layers present in the heterogenic subsurface. Figure 6 presents the robertsion diagram to gather the soil type information. This information can be used to infer the hydraulic conductivity. TNO (2017) and the municipality of Etten-Leur delivered the CPT information. Different box model alternatives of a specified size are created to implement layers up to 5 centimetres of thickness. This specified size of the box model has to coincide with the dimensions of the individual cells of groundwater model zero to make implementation possible. A box model cell depth of 5 meters is applied. This depth interval turned out to be the most suitable considering time efficiency to manually interpret the CPT data. Layers of the box model of smaller than 5-centimeter are difficult to interpret by hand, which resulted in the choice of minimum 5-centimeter thickness to be sure input error in minimized. The chosen cell depth does not coincide with the depth interval of groundwater model zero, so an adjustment was made and. The adjustment is explained in Chapter 3.2. The individual cell width and length match with the cells of the groundwater model zero, which is presented in Appendix A.5. This cell characteristic results in a 20 meters box length and width.

The aim is to get as much detail of the subsurface heterogeneity into the model as possible. The box models include CPT data layers of minimal 5 centimetres thickness, due to the detailed layering in the z-axis. This thickness results in one hundred layers of 5 centimetres. The discretization for the x-axis and y-axis is 100 by 100 cells, which results in cells of 20 by 20 by 5 centimetres inside the box models.

A system of alternatives is created to limit the number of different box models. The CPT data consists of a wide range of possibilities in layering and numbers of different layers. The alternatives are constructed during the process of CPT interpretation following the chosen 5-meter depth intervals. Many alternatives appeared to come back completely or consisted of about the same composition. This indicated the possibility to reuse the result of different alternatives in multiple 5-meter depth intervals found in various CPT data.

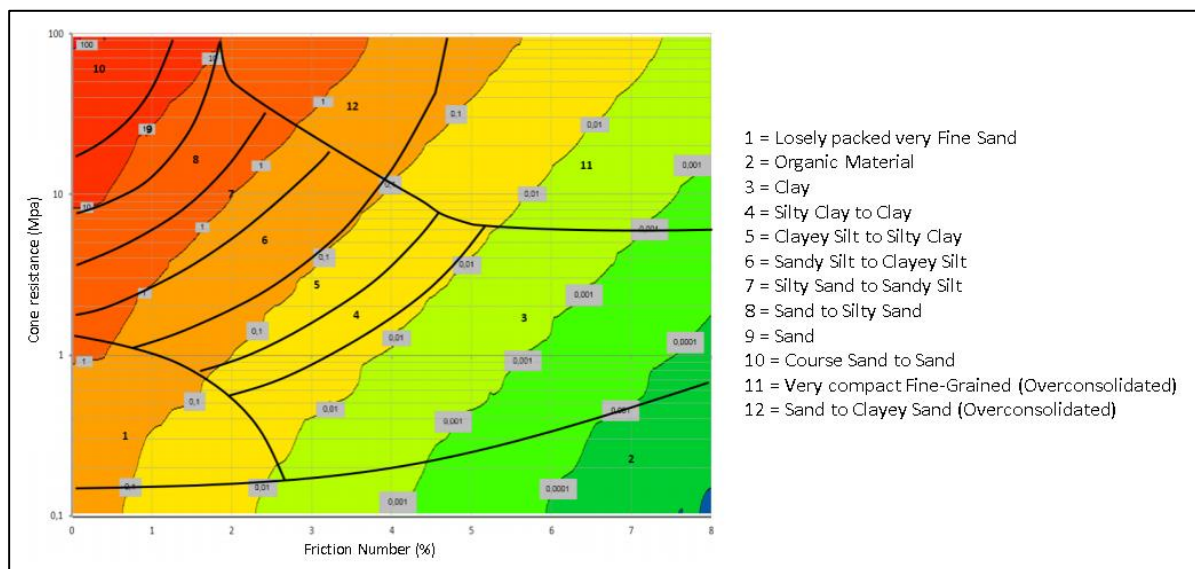


Figure 6: Robertson Diagram (Edelman, 2016).

3.1.1 Constructed alternatives including layer specification parameters

The first step was to specify the various types of layers with their corresponding hydraulic conductivity and porosity parameter values. The earlier mentioned Robertson diagram of Figure 6 is used to determine the layer specifications during the process of CPT interpretation (Edelman, 2016). The variability in the depicted layers of the Robertson diagram is related to the texture of the soil, which relates it to its grain size distribution. Layers are quantified using the cone penetration value and friction number gathered from the CPT data. The numbers in the grey boxes of Figure 6 represent the vertical hydraulic conductivity value. The specific vertical hydraulic conductivity value per layer type is estimated, based on how often particular values came forward during the classification. Two different sand groups are created, because of the noticeable difference between course sand and mild sand in the subsurface at the project location. Table 2 presents the final layer specification values.

Alternative	10
Short sentence	1SMd0.5 4SiS1.5 2SSi0.5 1CSi0.2 3SiC1.5 1C0.8
Layer 1	SMd
Thickness 1	0.5
Layer 2	SSi
Thickness 2	0.5
Layer 3	SiS
Thickness 3	0.4
Layer 4	SiC
Thickness 4	0.3
Layer 5	CSi
Thickness 5	0.2
Layer 6	SiC
Thickness 6	0.3
Layer 7	SiS
Thickness 7	0.4
Layer 8	SiC
Thickness 8	0.9
Layer 9	SiS
Thickness 9	0.2
Layer 10	C
Thickness 10	0.8
Layer 11	SiS
Thickness 11	0.5

Table 1: Example of one of the box model alternatives with the thicknesses in meters.

Multiplying the vertical hydraulic conductivity by a factor of two to ten determines the horizontal hydraulic conductivity parameter value. These factors relate respectively from sand to clay (Bot, 2011). In addition, comparisons to horizontal hydraulic conductivity values for different groups of subsurface material have been used. Yu, Kamboj, Wang, and Cheng (2015) presents the effective porosity and porosity values in Table 2. The porosity presents the total void space and the effective porosity includes the total void space minus isolated pores and the occupied pore volume. The remaining storage coefficient, S_s , and specific yield, S_y , are kept constant for the standard value of Visual Modflow. This gives $S_s = 1E-5$ and $S_y = 0.2$.

In total 38 alternatives are used specifying every 5-meter depth interval from CPT data more or less precisely. This consists of thirty self-assembled alternatives and the eight alternatives of Table 2. Table 1 presents alternative 10 as an example. The only possible difference in interpretation between the situation in practice can result from the number of layers in the alternative, but the layer thicknesses are accurate. Accepted interpretation differences in layer thickness are only 5-10 centimetre. A system with numbers and short words gives an overview of the layers in the alternatives. The short word is located between two numbers. The number in front represents the number of layers of that material sort and the number behind gives the total thickness of the layer. In case of, for example, multiple sand layers it represents the total thickness of the layers combined. The definitions of the short words are given in Table 2. Appendix B gives the 30 self-assembled alternatives.

Layer	Alternative number	Short word	K_v (m/day)	K_h (m/day)	Por. (-)	Eff. Por. (-)
SandCourse	31	SCr	20	40	0.40	0.30
SandMild	32	SMd	8	32	0.40	0.30
Silty Sand	33	SiS	5	20	0.40	0.25
Sandy Silt	34	SSi	0.75	6	0.45	0.20
Clayey Silt	35	CSi	0.30	2.5	0.45	0.20
Silty Clay	36	SiC	0.05	0.5	0.45	0.15
Clay	37	C	0.005	0.05	0.45	0.10
Peat	38	P	0.0005	0.001	0.90	0.44

Table 2: Resulting parameter values of the subsurface groups.

3.1.2 Box modelling properties

Every box model alternative is modelled separately for the horizontal and vertical direction. This is needed to gather the average horizontal and vertical hydraulic conductivities for each alternative. In addition, the average effective porosity and porosity are gathered.

In Figure 7 a schematic of a box model is given, including its characteristics. A specified head

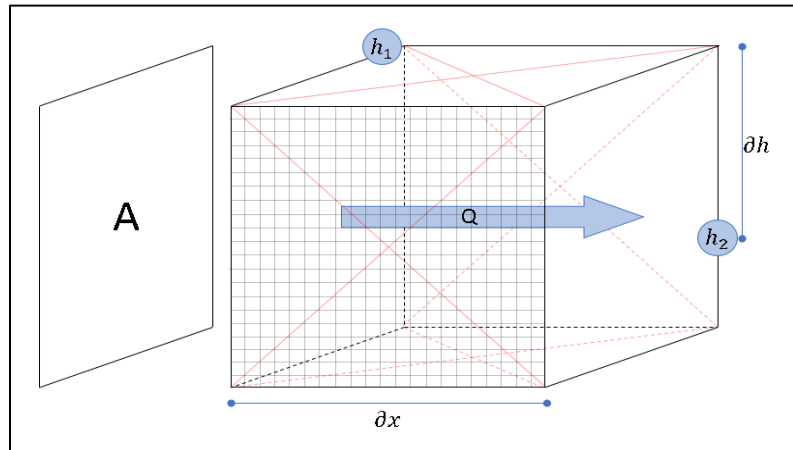


Figure 7: Schematic of one box model cell for a horizontal situation.

on each of the permeable sides creates a stationary flow through the box model. This results in a known gradient for each cell in the box. Boundary conditions have to be implemented to create this behaviour. Except for one direction, every boundary is made impermeable. This is shown for a horizontal flow situation in Figure 7. The impermeable boundaries are zero-flux boundaries and displayed with the red crosses. The specified head values for the vertical calculations are 15 meters at the top and 13 meters at the bottom, creating a 2-meter head difference. To create the stationary flow for the horizontal calculations, the head on the left is 15 meters and the head on the right is 13 meters. The parameter values and discretisation are applied as determined at the beginning of Chapter 3.1. Visual Modflow calculates the box models, whereafter back calculation of the average vertical or horizontal hydraulic conductivity is carried out using Darcy's law from Equation 17 (Freeze & Cherry, 1979).

$$Q = K \cdot \frac{\partial h}{\partial x} \cdot A \quad (17)$$

Where:

- Q = Discharge through the box (m³/day)
- K = Hydraulic conductivity (m/day)
- ∂h = Head (m)
- ∂x = Distance (m)
- A = Flow surface for the discharge (m²)

3.2 Preparing groundwater model zero and upscaling of the sample data

The area for the kriging methodology is chosen around the contaminant plume, due to the limited amount of CPT data in the groundwater model zero extent. The kriging extent is located around the industrial area of Vosdonk as presented in Figure 8. This area is 2.46 by 2.46 kilometres or 123 by 123 cells in the groundwater model. Only the first 25-meter depth is used for the implementation because the available CPT data does not reach deeper. The first big aquitard is located around 30 meters depth. This means this implementation uses the top aquifer in the system.

The groundwater model zero needed small adjustments for the implementation of the 5-meter depth intervals. In Figure 8 adjustment to this layering are displayed. The top layer varies in thickness, which results from the varying ground level. Most of the industrial area has a ground level of more or less 5-meters above N.A.P. This does not cause any problems for the data implementation. No sample data points are implemented when the ground level is higher or lower as respectively 5.2 or 4.8 meter. This is considered the best approach, because of the availability of only 5-meter depth alternatives. Otherwise, the error in interpretation is prone to get large.

Upscaling of the data is possible with all the different individual alternatives calculated. The various individual alternatives are piled up to recreate the sample data of the CPTs. For example, with a CPT of 20 meters depth four alternatives, interpreting each 5-meter depth of the CPT, are piled up together. This results in four points of sample data values in the model extent, which generate data with x-, y-, z- coordinate, hydraulic conductivity and porosity values. The process is repeated until every available CPT from Figure 9 is interpreted, which creates the complete sample data set for the kriging.

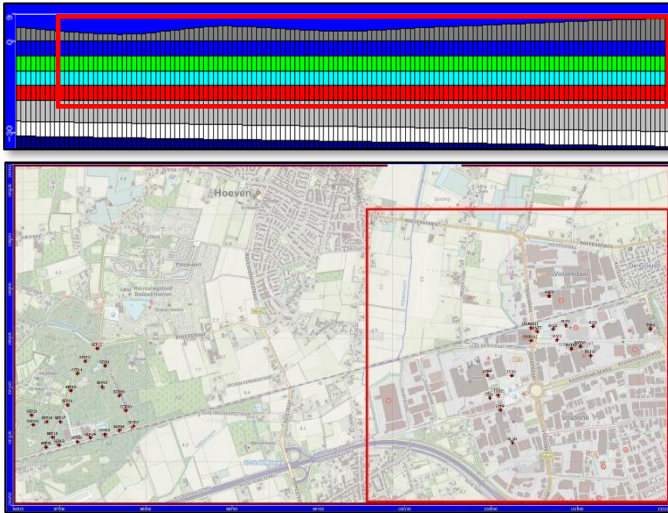


Figure 8: Overview of the location of the kriging implementation

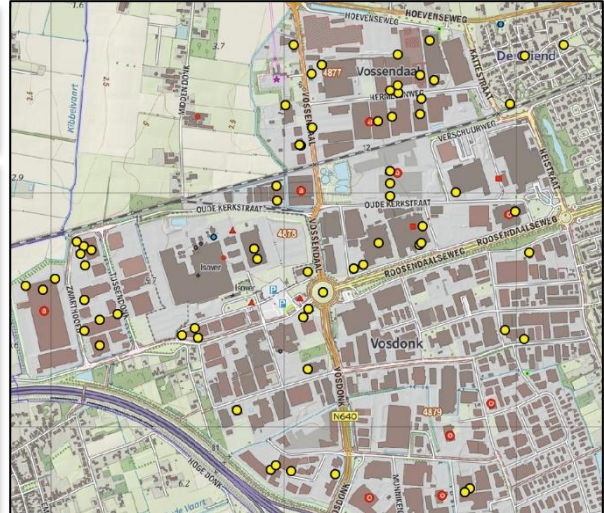


Figure 9: Map with the CPT data locations

3.3 Conditional simulations including the heterogenic subsurface variability

The very heterogenic Nuenen Group is present in the extent for the implementation of kriging. Conditional simulations are used to take into account this heterogeneity. These conditional simulations are individually called a scenario. The scenarios simulate the range of outcomes between a determined minimum and maximum situation. A stochastic analysis is created with this approach, which makes it possible to assign probabilities to a travelled distance of flow or contaminant.

Kriging with its use of semivariograms is a technique based on a stochastic model, but generates one single model as a result and is, in that sense, deterministic (Dubrule, 2003). It indicates the need for an extra step to produce conditional simulations with kriging. To accomplish this, the minimum, maximum and randomly generated sample data set of the scenarios need to be generated. Due to import limitations with Visual Modflow the randomly simulated scenarios are only applied to the hydraulic conductivities, which is elaborated further on.

The scenario for the minimum and maximum hydraulic conductivity is based on the research from van Alphen (1984) on the Nuenen Group near the city Best in the Netherlands. He stated that the minimum width of impermeable layers is 10 meters and the maximum is 100 meters. He also stated almost no presence of constant impermeable layers of substantial horizontal distance from -4 till -25 meters N.A.P. This indicates an open aquifer for the first 25 meters. The characteristics of the Nuenen Group found by van Alphen (1984) are given in Figure 10.

The modelled minimum and maximum scenario are sketched based on the research of van Alphen (1984). They are presented in Figure 11. The minimum hydraulic conductivity scenario is calculated using the complete length of impermeable layers, indicated with the blue colours. The width of the impermeable layers reaches 100 meters and the box model is 20 meters in width, which results in the choice of full width in the box models. Widths of the impermeable layers for the maximum situation are 10 meters. Every box model alternative is calculated with this minimum and maximum scenario.

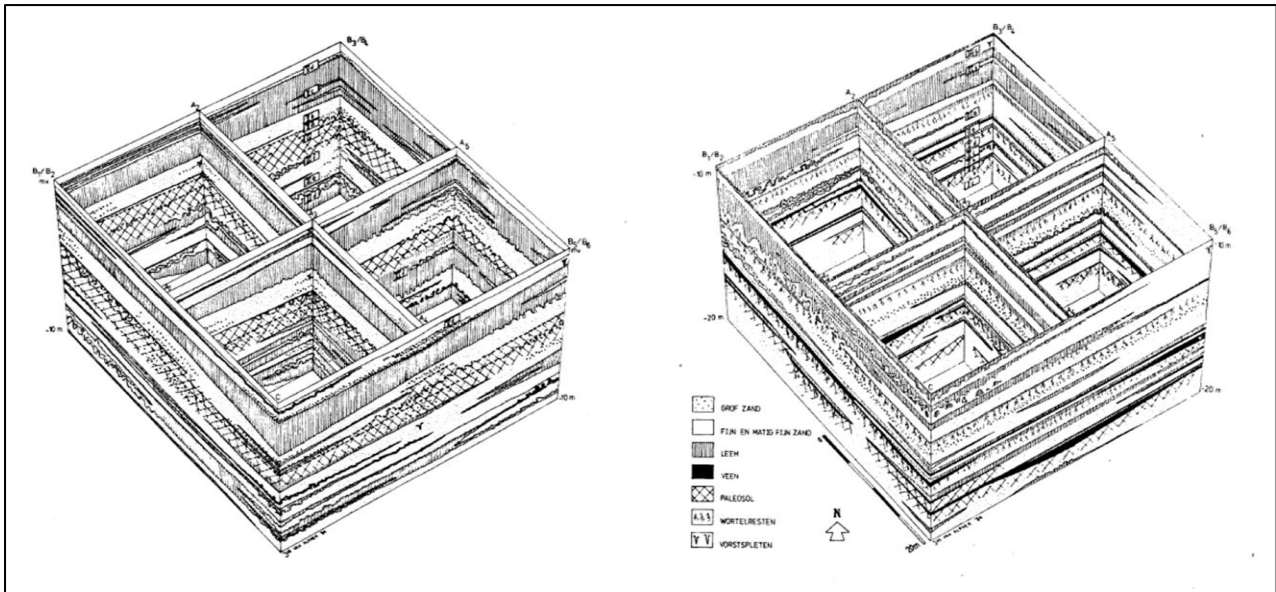


Figure 10: Variability of the Nuenen Group from 0 to -10 m (left) and -10 to -20 m (right) depth N.A.P. (van Alphen, 1984, pp. 38-39)

Results for the variability of the vertical and horizontal hydraulic conductivity, porosity and effective porosity are given in Appendix C. The sample data of these scenarios can be gathered after individual upscaling for both the minimum and maximum scenario.

MATLAB with its rand function is used to calculate the random scenario sample data. This rand function generates a random number between zero and one. A random number is created between the minimum and maximum hydraulic conductivity for each box model alternative. This repeats for each generated random scenario of sample data and results in continuously new hydraulic conductivity alternative values. As explained, upscaling is conducted afterwards generating multiple random sample datasets. The process is repeated using a for-loop in MATLAB and generates these datasets in a matter of seconds. The MATLAB code is given in Appendix F.1.

No conditional simulations are included for the porosity and effective porosity. Problems with import limitations and more time-consuming importation processes arose during the research. This was not expected at first instance. Chapter 3.5 gives a further elaboration on this topic. The variability of the porosity and effective porosity between the minimum and maximum box model values turned out to be small. This made it possible to use the averaged value to create one overall sample data set. The variability is presented in Appendix C. Only a small part of the box model cell (effective) porosity values get a change in grain structure. This explains the low box model variability for these two parameters, when looking at the average box model values. Kriging of the effective porosity and porosity is performed on the averaged data set and results are used in combination with all the random scenarios of the hydraulic conductivities.

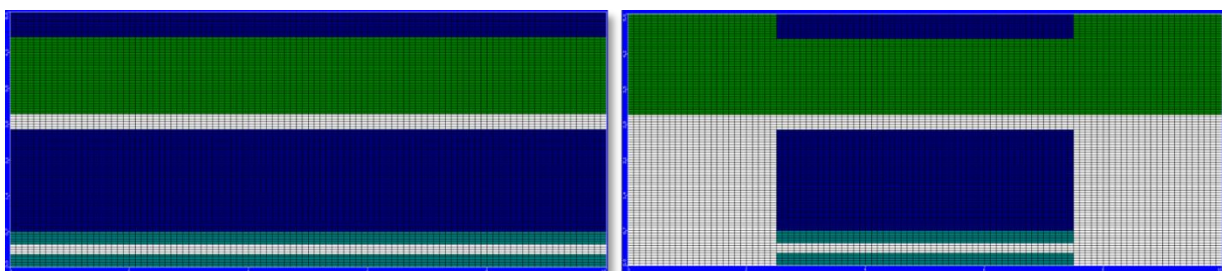


Figure 11: Example of a section view on the minimum (left) and maximum (right) limits of hydraulic conductivity and porosity for a box model in Visual Modflow.

3.4 Kriging

This section is divided in an explanation of the choice for the type of kriging, the chosen semivariograms and the calibration of the kriging. The kriged parameters are the hydraulic conductivities, effective porosity and porosity. Appendix D gives an overview of the results related to the calibration of the kriged parameters.

EasyKrig3D is consulted to perform the kriging (Chu, 2004). This tool is developed for the MATLAB interface. It includes a broad range of semivariogram models and kriging methods. In first instance, PyKrige was determined suitable for this research. PyKrige was preferred due to the relation to the open-source software Python (Murphy, 2014). PyKrige did not deal with the vertical direction of kriging correctly. Big datasets made the tool unstable and unreliable to use in this research.

3.4.1 *Finding the most suitable type of Kriging: Simple, Ordinary or Universal Kriging*

Deutsch (2002) states that ordinary kriging is used widely in map making, because of its robustness concerning trends. He based this on multiple observations from literature. Kleijnen and van Beers (2005) also notice this robustness from their numerical examples. The ordinary kriging method shows good results in relation to comparable estimation methods, especially when looking at the mean square error (Isaaks & Srivastava, 1989). Samui and Sitharam (2011) presented that the ordinary kriging obtained a better estimation of its results compared to the simple kriging method. They even state ordinary kriging is superior over simple kriging for observations of reduced levels of rock at unknown locations. Looking at accuracy, Daya and Bejari (2015) show the advantages of ordinary kriging over simple kriging. The simple kriging method obtains a loss in accuracy, because it estimates the low true values higher and the high values lower. Ordinary kriging shows to be favourable over simple kriging, which indicates a choice must be made between the universal and ordinary kriging.

Mesic Kis (2016) advises the universal kriging because it takes into account the identification and calculations of trends in the data. Universal kriging could be the better method when a clear trend is present in the input data. Input data for the subsurface consists of structural maps, bore logs and CPTs and is strongly related to the soil type of subsurface layers. This seems like a convincing statement to go for universal kriging, but Webster and Burgess (1980) convince to go for the ordinary kriging instead. They state that universal kriging is by no means universally applicable in soil survey. It only appears to be the most general and powerful interpolation method for mapping from sample data.

Webster and Burgess (1980) explain the universal kriging approach is only suitable for soil data in case measurements over contiguous volumes of soil are made. Mesic Kis (2016) works with height data on a single fault. That indicates small changes in drift, which makes the universal kriging method favourable. This research consists of points observations. These are described as measurements of soil data considering small widely separated volumes of soil. Webster and Burgess (1980) describe the high probability of some large nugget effects in the semivariograms for this type of observation data. They state it makes a simple or ordinary kriging method the better choice. The large nugget effects prevent any distinction between a constant and changing drift. The subsurface consists of clay layers decreasing in thickness over the width and length of the model extent, which would be estimated incorrectly by the universal kriging. Mesic Kis (2016) also mentioned the ordinary kriging can still be considered the “best linear unbiased estimator”. She clarifies that the ordinary kriging is also a useful method for the data sets she had available. The ordinary kriging suits this research data best taking into account the findings from the literature.

3.4.2 The Kriging semivariograms

Insights in the suitability of semivariograms for the hydraulic conductivity, porosity and effective porosity were gathered from Chapter 3.2. The spherical, exponential and Gaussian semivariograms are used most often for subsurface parameters. The exponential cosine semivariogram model fitted the hydraulic conductivities best, which represents an extended variant of the exponential semivariogram. Chu (2004) already included this semivariogram in the EasyKrig3D tool. The general exponential semivariogram model created the best fit for the effective porosity and porosity. Table 3 includes the semivariogram model and parameter results.

Parameter	Model	Nugget (-)	Sill (-)	Range (-)	Lag distance (-)	Hole effect (-)
K_z	Exponential-cosine	0.38193	0.91871	2.2007	1.0	6.1349
K_{xy}	Exponential-cosine	0.12404	0.9199	0.39803	0.97828	5.4224
Eff. Por.	Exponential	0.034272	1.0944	0.1623	0.95	-
Por.	Exponential	0.16075	1.0478	0.16608	0.95	-

Table 3: Semivariogram parameter properties.

Equation 18 presents the extended exponential-cosine semivariogram model (Chu, 2004). A new parameter, b , is present, which represents the length scale for the hole effect. Ma and Jones (2001) state a hole-effect semivariogram typically exhibits sinusoidal waves that form peaks and troughs and convey the cyclicity of the underlying phenomenon. The cosine function is multiplied by the exponential variogram to incorporate it correctly. This provides the wavelength and phase cyclicity in the model, which interprets the hydraulic conductivity data well. Figure 12a and Figure 12b present the nice fit at both the start and the end of the semivariogram.

$$\gamma(h) = c_0 + c \left(1 - e^{-\frac{h}{a}} \cdot \cos(b \cdot h) \right) \text{ for } h > 0 \text{ and } \gamma(h) = 0 \text{ for } h = 0 \quad (18)$$

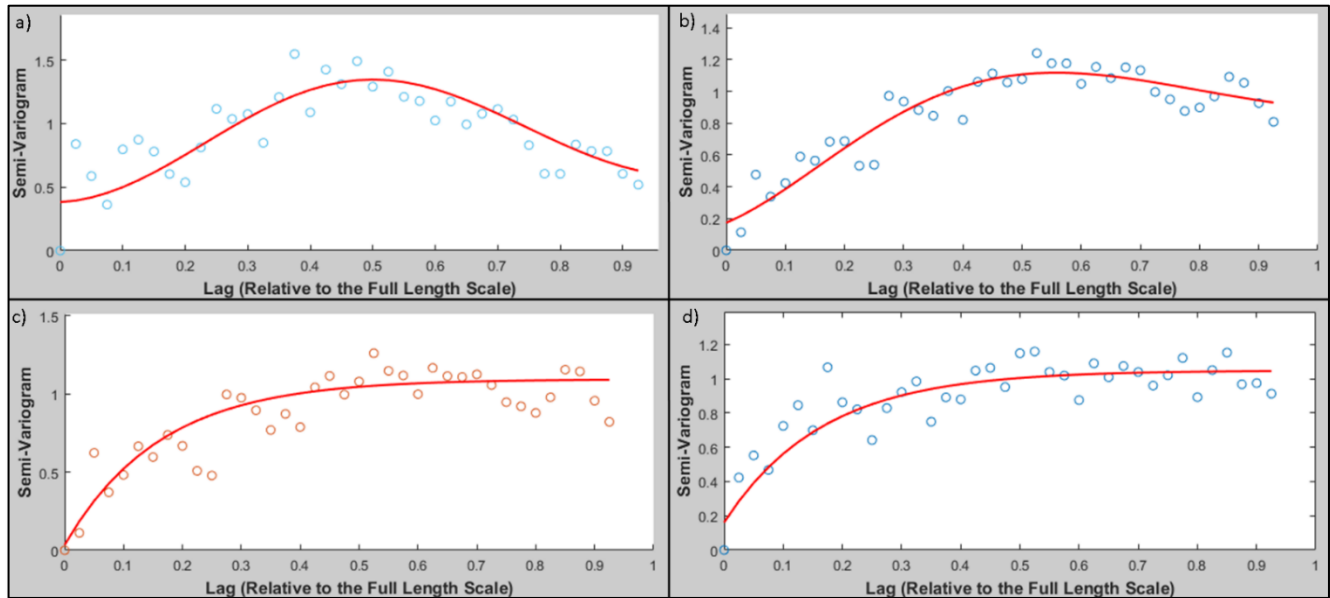


Figure 12: Semivariograms of a) Vertical hydraulic conductivity, b) Horizontal hydraulic conductivity, c) Effective porosity and d) Porosity.

3.4.3 The kriging calibration

EasyKrig3D consists of a couple of calibration tools, which help to validate the accuracy of the kriging. Kriging is calibrated with two cross-validations, Q1 and Q2. Q1 checks the statistics of the mean of the residual error and approximately follows the distribution. Q2 checks the statistics of the variance of the error $Q2 * (n-1)$ and approximately follows the chi-square distribution with parameter $n-1$. Double kriging gives a third validation, which compares the observed data sample data points with the calculated kriging values. The following two steps result in the best possible kriging validation. First, the closest semivariogram fit is applied by hand. Secondly, the LSQ-fit option in EasyKrig3D is used to implement small adjustments. The LSQ-fit option consists of the least square fit and optimises the semivariogram fit (Chu, 2004).

Q1 is the most important validation tool. Every kriging parameter reached the acceptable region, which consists of the 0.025 and 0.975 percentile. Q2 was difficult to calibrate, due to the variety of sample data values in the parameters. The horizontal conductivity, porosity and effective porosity could not reach within the acceptable region. To accomplish the closest fit to an acceptable region in Q2, a significant amount of time was spent. Reproducing the peak values in the double kriging validation turned out to be impossible. The kriging appears to smooth out these peaks. Nevertheless, there was tried to make the best possible fit for the double kriging validation. Figure 13 gives the calibration of the horizontal hydraulic conductivity as an example. Appendix D gives the calibration results of all kriged parameters. The well-calibrated fits for the validation data of Q1 makes the kriging data acceptable, despite some unfavourable observations in the double kriging and Q2

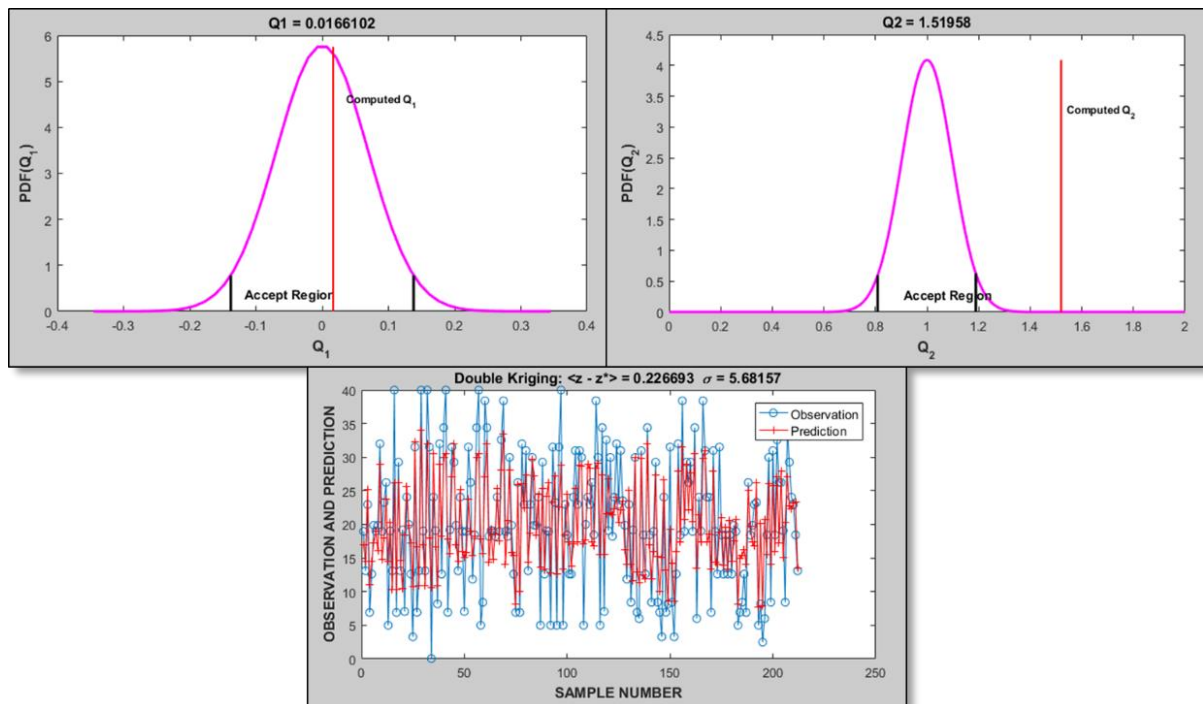


Figure 13: Calibration results of the horizontal hydraulic conductivity.

3.5 Importing the kriging datasets and generating flow lines

After the calculation of all the subsurface scenarios, the kriging data sets need to be imported in the Visual Modflow software. A batch kriging function in EasyKrig3D kriged all the random scenarios of the hydraulic conductivities at the same time. As explained, these are used in combination with the averaged effective porosity and porosity kriging data sets. The minimum and maximum scenarios are imported with respectively their minimum and maximum kriging datasets. Direct importation of the kriging data sets in Visual Modflow was not possible. The dataset needs a suitable import structure for Visual Modflow.

Finding an appropriate import structure which would not overload Visual Modflow turned out to be a big challenge. Test runs were conducted in advance of the start of the research but included smaller datasets. This proved the possibility of importing each of the five 5-meter depth intervals at the same time, but with the datasets of this research the Visual Modflow software suddenly kept on crashing. The import structure needed to be switched, due to an overloading problem. First, the structure was, with columns from left to the right, x-, y-, z-coordinate followed by the hydraulic conductivity values. The structure is changed to row, column and layer number in the groundwater model extent followed by the hydraulic conductivities. This import structure includes a big disadvantage. Only layer by layer importation is possible, which increases the import time consumption with a factor of five. These five layers have to be imported individually instead of as a group. The developed MATLAB script of Appendix F.2 converted the kriging datasets easily and quickly.



Figure 14: Location Flowline starting points.

In total 22 groundwater models are developed, which each include unique subsurface characteristics. Twenty random simulation scenarios are developed and the remaining two models consist of the minimum and a maximum scenario. The start locations of the flowlines are assigned in each scenario to make the step from groundwater model to 1D solute transport. Locations are chosen in consultation with Afvalzorg and presented in Figure 14.

Flowline calculations are conducted using MODPATH in the Visual Modflow Software. The complete groundwater model needs to run before MODPATH simulation is possible, because of the calculation of hydraulic heads in the model. Appendix A presents an example of the results for these hydraulic heads. The flowlines need start times, which are chosen taking into account the available initial concentration data of the contaminants. Further elaboration on this matter is given in Chapter 3.6.4. The total simulation time for each groundwater model is 35 minutes, which includes both simulations. The batch run function of Visual Modflow included a glitch, which the manufacturers could not solve either. This resulted in manually running all 22 simulations. The generated flow lines were exported from Visual Modflow in two shapefiles. One shapefile includes an overview of the 2D travel path and the other shapefile contains the travel time and travel distance data points.

Due to a couple of problems, not as many simulations were conducted as was preferred in first instance. This was caused by the explained import problems and batch run glitch, which increased the time consumption of the complete process a lot. Visual Modflow also stored the simulation data very inefficient, which is important to mention. Each simulated groundwater model takes up 13 gigabytes of storage.

3.6 1D solute transport MATLAB model

This section explains the methodology and materials used for the 1D solute transport model. First, the application of the governing equation, the used boundary condition and the implementation the progressive degradation add-on for contaminants are presented. This is followed by insights into the needed contaminant data and data management of the exported flowlines. At last, the calibration of the model is explained. The complete solute transport model is developed using MATLAB. An example of the 1D solute transport model for flowline 1 is presented in Appendix F.4. This code is also suitable for flowline 2 or groundwater model zero exports after easy adjustments.

3.6.1 Application

Simplifying the model by disregarding the dispersion has the biggest impact on the solute transport model. This important influence of dispersion is especially present in multi-dimensional large-scale solute transport modelling, which was explained in Chapter 2.4. Including the dispersion at 1D scale is out of the time scope of this research, because it adds considerable complexity to the problem. In addition, Heimovaara, Keijzer, and Velstra (2004) found difficulties in quantifying the dispersion with limited amounts of sources and data available, which resulted in a more or less trivial behaviour. Results of this research added to the choice to disregard the dispersion, due to similar aspects between the researches.

MATLAB is used to create a numerical solution. An explicit finite-difference formulation with a first-order upwind scheme is used to perform the calculations. Clement et al. (1998) state the simplicity of the explicit method. They also mention the computational efficiency for advection dominated problems if the transport step sizes do not limit the stability constraints. To reach convergence of the model the time step and grid cells are refined until differences in output are not significantly noticed. The governing equation presents an advection dominated problem and is given in Equation 12. Following the statements of Clement et al. (1998), it is considered a suitable approach to construct the model.

It is import to realise the effects and presence of numerical dispersion for advection dominated problems. The first-order upwind explicit method includes this numerical dispersion, caused by truncation error. Truncation error causes similar effects as with physical dispersion. The numerical dispersion causes problems smearing of the concentration fronts when the physical dispersion is not present. These concentration fronts should normally consist of sharper appearances (USGS, 2016).

The explicit finite-difference method is expressed as given by Equation 19, 20 and 21 (Zheng & Wang, 1999).

$$R \cdot \theta \cdot \frac{C^{n+1} - C^n}{\Delta t} = L_{ADV}(C^n) + L_{RCT}(C^n) \quad (19)$$

$$L_{ADV}(C^n) = v_x \cdot \frac{\partial C}{\partial x} \quad (20)$$

$$L_{RCT}(C^n) = \lambda C \quad (21)$$

R is the retardation coefficient, θ is the porosity, Δt is the time step, C are the concentration values, L_{ADV} is the finite-difference operator for the advection term and L_{RCT} is the finite-difference operator for the chemical terms. The chemical terms consist of the decay and the add-on of the RT3D principle for the 1D system. This add-on is explained in the next section. Equation 22 results in a one-step calculation format for the progression of the steps.

$$C^{n+1} = C^n + \frac{\Delta t}{R \cdot \theta} [L_{ADV}(C^n) + L_{RCT}(C^n)] \quad (22)$$

Attention is paid to the stability of the system. The stability of the system for the advection and chemical term is presented in respectively Equation 23 and Equation 24 (Zheng & Wang, 1999).

$$\Delta t \leq \frac{R}{|v \cdot \Delta x|} \quad (23)$$

$$\Delta t \leq \frac{1}{|\lambda_1 \cdot \lambda_2|} \quad (24)$$

The specific velocity is given by v (including the porosity term) and λ_1 and λ_2 are the decay terms for respectively the gas and liquid phase. Only the liquid phase applies in this research, which gives $\lambda_2 = \lambda$. The calculation of the stability components in the 1D solute transport equation are conducted for each active cell.

3.6.2 Add-on for the step by step degradation of the chlorinated solvents

The degradation of one of the components of the chlorinated solvents reacts to a next form of the chlorinated solvent in the chain of chemical reactions. Chapter 2.2 introduced this system, which is present at the project location and taken into account in this research. The governing equation changes for the contaminant component after the first group of chemical reactions, which is done in Equation 25 (Clement, Hooker, Sun, & Petersen, 1998).

$$R \frac{\partial c_1}{\partial t} = -v \frac{\partial c_1}{\partial x} - \mu_1 \cdot c_1 + \mu_2 \cdot Y \cdot c_2 \quad (25)$$

Two first order degradation rates μ_1 and μ_2 are included in Equation 25. μ_1 is the degradation rate, decay, for the contaminant concentration of the current component in the system c_1 . μ_2 is the degradation rate for the concentration of the contamination component with the previous advective and chemical reactions (c_2). Y represents the yield coefficient, which is a value for the part of the degraded contamination c_2 , which results in an added amount of concentration for c_1 . Simulations of the 1D solute transport in this research are conducted with the governing equation of Equation 25.

3.6.3 Boundary condition

A Neumann boundary condition is applied to the model, which gives fixed flux boundary conditions. The Neumann boundary condition needs ghost nodes. These ghost nodes make it possible to create a zero gradient across the boundary. Figure 15 illustrates the ghost nodes (Zheng & Wang, 1999).

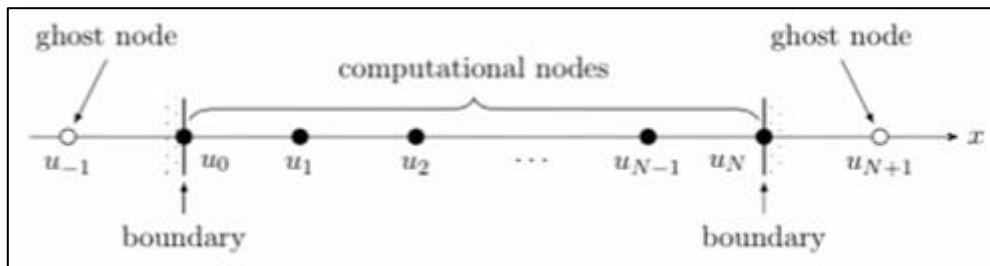


Figure 15: Ghost node overview for the Neumann boundary condition.

3.6.4 Managing the exported data of the flow line

The generated flowlines needed data management and pre-exporting preparation to perform a proper solute transport calibration in the future. The start time of both flowlines is determined beforehand, which is based on the available initial contaminant concentration data. This concentration data is received from the database of Afvalzorg. Flowline 1 and 2 start respectively at 2001 and 2011. The chosen time step for the export of data is two months and keep the 1D solute transport model stable. The 2-month time step needs to be inserted in Visual Modflow before flowline data is exported.

The velocity per time step is calculated using the known constant time step and resulting travelled distance data. The travelled distance structure of the exported data is based on the start point of the

flowlines. This means the travelled distances calculated by Visual Modflow includes the distance between a travelled point and the starting point. The successive travelled distance between the time steps is needed for the 1D solute transport model. These are calculated using a developed MATLAB function given in Appendix F.3. The exported 2D and 3D travel distances are converted to the successive 2D and 3D travelled distance data between time steps. These are used for the calculation of the velocity data. The 1D solute transport model uses the 3D travelled distance and velocity data.

3.6.5 The characteristics of the contamination

Three input parameters of the 1D solute transport model are gathered from the literature. These are the yield, retardation and the decay coefficients of the contaminants. The initial concentration values are gathered from available data delivered by Afvalzorg. This section gives an overview of the methodology regarding the quantification of the parameters and the calibration of the 1D solute transport model.

Specification of the initial contaminant parameters

The yield coefficients result from the stoichiometric relations between the different chlorinated solvents. The following yield coefficient values result from the reactions. PER to TRI gives $Y_{PCE/TCE} = 0.79$, TRI to CIS gives $Y_{TCE/CIS} = 0.74$, CIS to VC gives $Y_{CIS/VS} = 0.64$ and VC to ET gives $Y_{VS/ET} = 0.45$ (Clement, Hooker, Sun, & Petersen, 1998).

Wiedemeier et al. (1998) page 290 and 291 gives extensive research on the first-order biodegradation rate constants. The collected range of values for the decay coefficients is provided in Table 4. No decay value for ethene is considered so that it can function as a tracer. Ethene is also considered the last contaminant in the system regarding this research.

Solute	Decay_{Initial}
PER	0.00068-0.54
TRI	0.0001-0.021
CIS	0.0001-0.026
VC	0.0003-0.012

Table 4: Decay coefficients.

The retardation coefficient needs to be calculated. It is not directly gathered from the literature. Wiedemeier et al. (1998) page 178 and 179 presents a methodology to determine the retardation coefficient using Equation 26 and Equation 27 to conduct calculations.

$$R = 1 + \frac{\rho_b \cdot K_d}{n} \quad (26)$$

$$K_d = K_{oc} f_{oc} \quad (27)$$

ρ_b represents the bulk density of the aquifer, n presents the porosity and K_d is the distribution coefficient. This distribution coefficient is calculated with the help of K_{oc} , the soil sorption coefficient normalized for total organic carbon content and f_{oc} , the fraction of total organic carbon in milligrams organic carbon per milligrams soil. These parameters are obtained from Wiedemeier et al. (1998) and Nipshagen and Praamstra (2007).

On average, the overall subsurface includes a silty sand to medium sand. This indicates the average particle size present in the model and gives a total fraction of organic carbon of 0.5%. The most transmissive aquifer zones generally have the lowest total organic carbon concentration, because the majority of dissolved contaminant transport occurs in the most transmissive portions of the aquifer. The choice for this value gives a conservative prediction of the contaminant retardation. A coinciding porosity value is estimated around 0.40 and the bulk density is 1.6 Kg/L (Wiedemeier et al., 1998).

Wiedemeier et al. (1998) page 180 states literature values for K_{oc} are reliable. It is normally not necessary to conduct laboratory tests. Numerous authors conducted experiments to determine these values for common contaminants. Nipshagen and Praamstra (2007) gives K_{oc} values for the contaminant components present at the project location. These values are presented in column 5 of Table 5.

Contaminant	ρ_b (Kg/L)	n (–)	f_{oc} (–)	K_{oc} (L/Kg)	K_d(L/Kg)	R (–)
PER	1.6	0.4	0.005	240	1.2	5.8
TRI	1.6	0.4	0.005	110	0.54	3.2
CIS	1.6	0.4	0.005	72	0.245	2.44
VC	1.6	0.4	0.005	33	0.285	1.66

Table 5: Parameter values for and calculation of the retardation coefficient.

As mentioned in Chapter 3.6.4, decisions on the start time of the generated flow lines are based on available initial contaminant concentration data. The initial contaminant concentration data is provided by Afvalzorg. A well-chosen start time is necessary, because of the possibility to relate a future calibration value to a reliable start concentration. The initial concentrations for flowline 1 originate from surrounding contaminant concentration values in and around well log 2710 in the year 2001. Initial contaminant concentrations for flowline 2 originate from surrounding concentrations around well log 101, 103 and 104 in the year 2011. The initial concentration values are given in Table 6 and Figure 14 presents the start location.

The release of contaminant is estimated to have a duration of approximately 29 years. Grontmij (2002) shows the contamination release started around 1965 and ended in 1994. This indicates an ending to the spread of contaminant. The end of contaminant spreading is processed in the model. This is achieved by restating initial conditions to zero for every contaminant, 29 years after the end of the estimated contaminant spreading in 1994. The back of the plume possibly arrives around 2023, because a 29-year distant spread is present from 1994 onwards.

Flowline	PER (µg)	TRI (µg)	CIS (µg)	VC (µg)	ET (µg)
1	11000	130000	12500	1000	0
2	27	1900	27000	170	0

Table 6: Initial concentrations at the start time and location of the flowlines

Calibrating the specified contaminant parameters of the 1D solute transport model

The calibration process is conducted with Flowline 1 and used to determine the characteristic values for the decay and retardation coefficients in the area Vosdonk Noord at Etten-Leur. Two locations with field measurements are implemented in the calibration process. The concentration data from bore log 2710 and 2714 are used. Bore log 2714 coincides with flowline 1 further on the travel path and bore log 2710 consists of the initial concentration data. The fit of the model values to the field measurement data was accomplished by calibrating the decay and retardation parameters. Preferably only the decay parameter was changed, but the retardation coefficient also needed adjustments to find an acceptable fit.

Solute	Field data at 2714 (mg/L)	Calibrated Model (mg/L)	Difference (mg/L)
PER	1.3	3.3983e-10	1.2999
TRI	150	147.2582	2.7418 (1.82%)
CIS	1700	1732.9	32.9 (1.94%)
VC	7.7	7.2686	0.4314 (5.6%)
ET	0	76.4199	76.4199

Table 7: calibration results 1D solute transport model.

The results of the calibration are presented in Table 7. Fitting PER and ET turned out to be impossible in this 1D application. ET is mainly used as a tracer, due to the chosen retardation of 1 and decay of 0. This means the fit for ET does not matter so much. The calibration of PER is acknowledged for this research because it is only present in small amounts and is not considered the most aggressive contaminant. The three most important contaminants at the project location are well calibrated. VC was a difficult contaminant component, but in the end a decent fit is accomplished.

Solute	R_{initial} (-)	R_{calibrated} (-)	Decay_{Initial} (-)	Decay_{calibrated} (-)
PER	5.8	5.8	$6.8 \cdot 10^{-4} - 5.4 \cdot 10^{-1}$	$1.26 \cdot 10^{-3}$
TRI	3.2	2.605	$1.0 \cdot 10^{-4} - 2.1 \cdot 10^{-2}$	$1.0 \cdot 10^{-4}$
CIS	2.44	2.74	$1.0 \cdot 10^{-4} - 2.6 \cdot 10^{-2}$	$1.0 \cdot 10^{-7}$
VC	1.66	1.66	$3.0 \cdot 10^{-4} - 1.2 \cdot 10^{-2}$	$6.0 \cdot 10^{-4}$
ET	1	1	0	0

Table 8: Initial and calibrated parameter results for the retardation and decay coefficients.

The initial and calibrated values for the retardation and decay coefficients are presented in Table 8. The retardation coefficients are still within reach of plausible values. This is shown for the possibilities in K_{OC} values by Wiedemeier et al. (1998). The decay values of TRI, CIS and VC consist of very low values. Decay values below those indicated in literature are inserted because otherwise no acceptable fit could be reached. Research from Orvion BV proved the acceptability of these decay values. Appendix E includes the report from Orvion BV.

The results of Appendix E show a potential for biological dechlorination, which can be characterized as follows:

1. Partial degradation to DCE is expected to occur at a slow rate in source zones with the pure product of PER or TRI.
2. Complete reductive dechlorination may not take place everywhere but can be expected to occur in some places. This happens at a slow rate, especially in the deep(er) more reduced groundwater.
3. Micro-aerophilic dechlorination of CIS and VC can be expected to occur, but only at a very slow rate

The conclusions of the report of Orvion approve the calibrated first order degradation rates. The subsurface characteristics of the contamination are gathered and presented in Table 8. All calculations for the 1D solute transport model have been conducted using the calibrated parameter values. The calibrated model is presented in the MATLAB code of Appendix F.4.

3.7 Overview of the conducted simulations

Three variants of data about the contaminant behaviour are delivered with the help of graphs. The first type consists of concentration data over the complete length of the flowline at a specified year in the model. The second type contains concentration data over the time at an in the model specified travelled distance located on the flowline. The data reaches from the start year of the flowline until 2066. Concentration values are given in $\mu\text{g/L}$. They can easily be adjusted to a mass flux value. This is accomplished by multiplying the concentration values times the velocity and corresponding advection coefficient. The mass flux is given in $\mu\text{g/m}^2\text{d}$.

The third type of data consists of the probability distributions of the contaminants, which includes the range of travelled distance in the specified year in the model. The measurement detection limit from the data of Afvalzorg is used to recognise the arrival of contamination. This limit is $0.1 \mu\text{g/L}$ and can be easily adjusted.

4 Results & Discussion

This chapter is divided into the three main components of the research. It begins with the results and discussion of the kriging for the hydraulic conductivity, porosity and effective porosity parameters. Secondly, the groundwater flow behaviour for the model zero and kriging input is reviewed and discussed. Finally, the 1D solute transport is examined.

4.1 Kriging

The variability between the minimum and maximum values of vertical hydraulic conductivity is clearly visible. This most noticeable kriging result is presented in Figure 16a. Spots of high conductivity mix up with spots of lower conductivities. This indicates a considerable difference compared to the assumption of the “pancake” approach for groundwater model zero. The complete kriged model area includes a presence of this variability in spots. Over the horizontal distance, no constant low conductivity layers are not found. This indicates the presence of one big open aquifer over the first 25 meters of the kriged models.

The horizontal hydraulic conductivity shows the same characteristic as for the vertical hydraulic conductivities, but contains a smaller difference between the minimum and maximum condition. This difference in values is hard to see, but the variability is confirmed by Table 22 in Appendix C. The characteristics of the subsurface explain the lower variability in comparison to the variability of the vertical hydraulic conductivity. The horizontal flow was already able to move in the higher conductivity layers before the implementation of the horizontal variability. This resulted in less flow advantage from the applied decrease in low conductivity layer width. Both directions of hydraulic conductivity include a visible range of variability, which confirms the presence of the heterogenic Nuenen group.

The spots with specifically high or low hydraulic conductivities are not always present at the same location for the different random conditional simulations. A clear example is presented in Figure 17a. Two random simulation kriging boxes are created and ready for implementation. The left simulation displays a low conductivity area inside a high conductivity spot within the red circle. At this same position, the simulation to the right displays a very high conductivity spot. This effect results in different speeds and movements of flow.

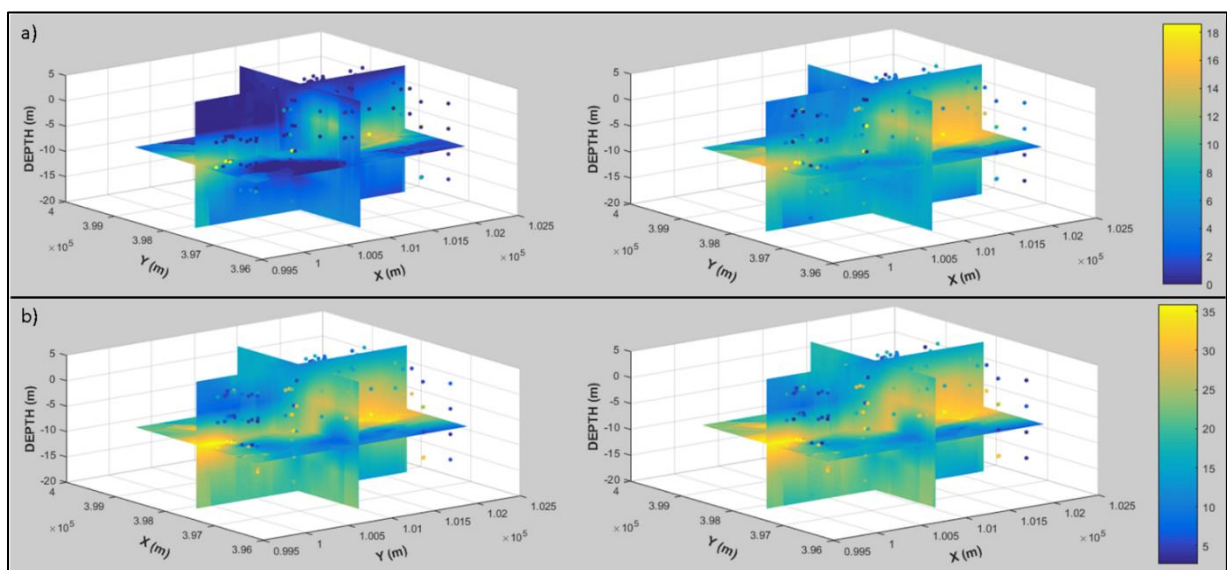


Figure 16: Hydraulic conductivities kriging results with a) K_z min left and K_z max right and b) K_{xy} min left and K_{xy} max right. The dots represent the CPT sample data points, X and Y are the coordinate locations in meters and the depth is in N.A.P.

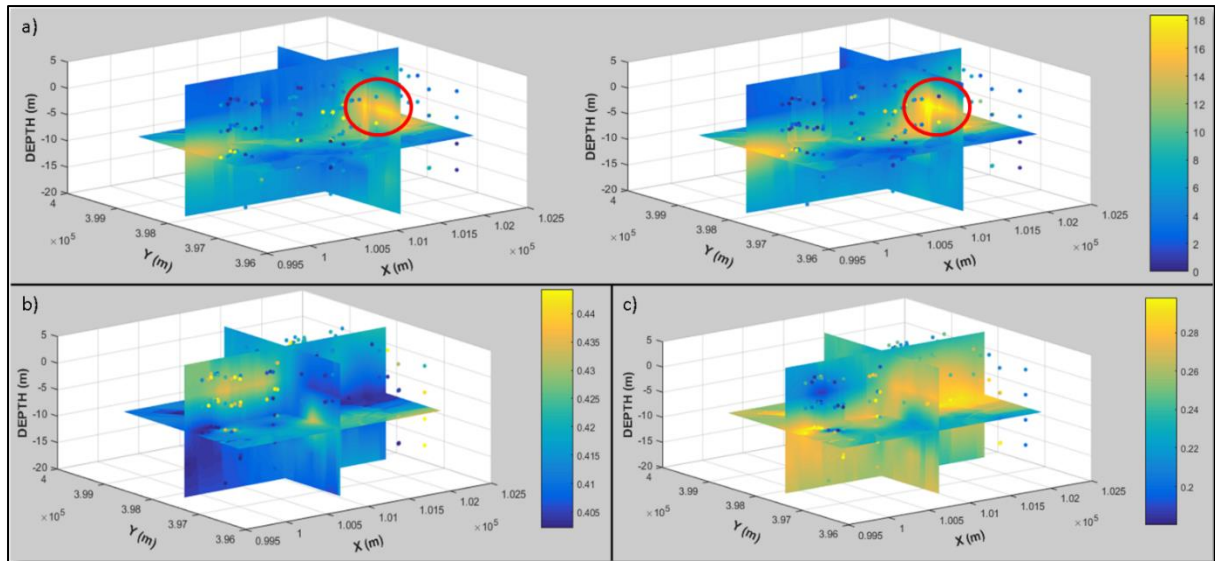


Figure 17: Kriging results of a) Two random simulation outputs for K_z b) Porosity and c) Effective Porosity. The dots represent the CPT sample data points, X and Y are the coordinate locations in meters and the depth is in N.A.P.

Comparable situations arise throughout the complete area for both low and high hydraulic conductivities. The uncertainty in variability is taken into account nicely by the kriging method. This represents the constant possibility of regions with lower or higher hydraulic conductivity values in the subsurface.

The values of the porosity and effective porosity indicate the most common layer type found in the subsurface. The variability in values over the model area is shown in Figure 17b Figure 17c. The upper left area has a high chance for lower hydraulic conductivities characterising clay because the porosity and effective porosity are at respectively 0.45 and 0.15. Lower left and mid-range areas are likely to have higher hydraulic conductivities representing sandy layer types, due to values of 0.4 and 0.3 for respectively the porosity and effective porosity. Observations of more or less reliable indications of the most common layer types can be done, although these kriged datasets consist of the averaged values between the minimum and maximum condition.

The three points of discussion related to the kriging methodology are the amount of CPT data, the detail of the vertical grid and the smoothing of the sample data peaks. For every project, the amount of subsurface data available is considered too small. This research also consists of a limited amount of data, which spread nicely over the kriged area. Still, the chance of missing some spots of certain hydraulic conductivity is present because the horizontal width of impermeable layers ranges from 10 to 100 meters in a kriged model area of 2.3 by 2.3 kilometres. The same principle applies to the 5-meter depth interval of CPT interpretation. Decreasing the depth interval could obtain more detail in interpreting CPT values. This results in disadvantages considering an increased amount of work, pressure on the Visual Modflow software and time consumption to get to the results. At last the kriging interpolation method showed smoothing of the peak values, which could create higher and lower values as found in practice and take away detail. This is illustrated in Appendix D. Only a small impact on the results is expected, because of the validity of the kriging calibration. The kriging method consists of a fair representation of the practical situation. Only very high amounts of detailed subsurface data create the possibility for a very close representation to the real life situation.

4.2 Groundwater Flow Behaviour

Simulating particles flowing through the model gathers insights in the groundwater flow behaviour. In Figure 18, Figure 19, Figure 20 and Figure 21 each marker on the flowlines represent an elapsed amount of time of ten years.

The top layers of both groundwater model zero and the kriged model include a strong flow towards the rivers in a north-western direction. An overview of the layers at ground level is presented in Figure 18a and Figure 18b. This effect arises until a depth of -10 m N.A.P. for the groundwater model zero. The flow of the kriged models is drawn to the river until at least a depth of -30 m N.A.P. This is presented in Figure 21. Groundwater model zero has no flow inside the river from below -10 m N.A.P., which results in a north direction of flow. The groundwater flow of the kriged model still drains to the river at these depths. This can be explained by the kriging result with one open top aquifer, which was found in Chapter 4.1. The comparison of the flow directions at these deeper layers is given in Figure 18c and Figure 18d. The model results reveal a significant role of the river as a draining factor for the groundwater flow in mainly the top layers. The kriging implementation increases this influence due to the presence of one open top aquifer.

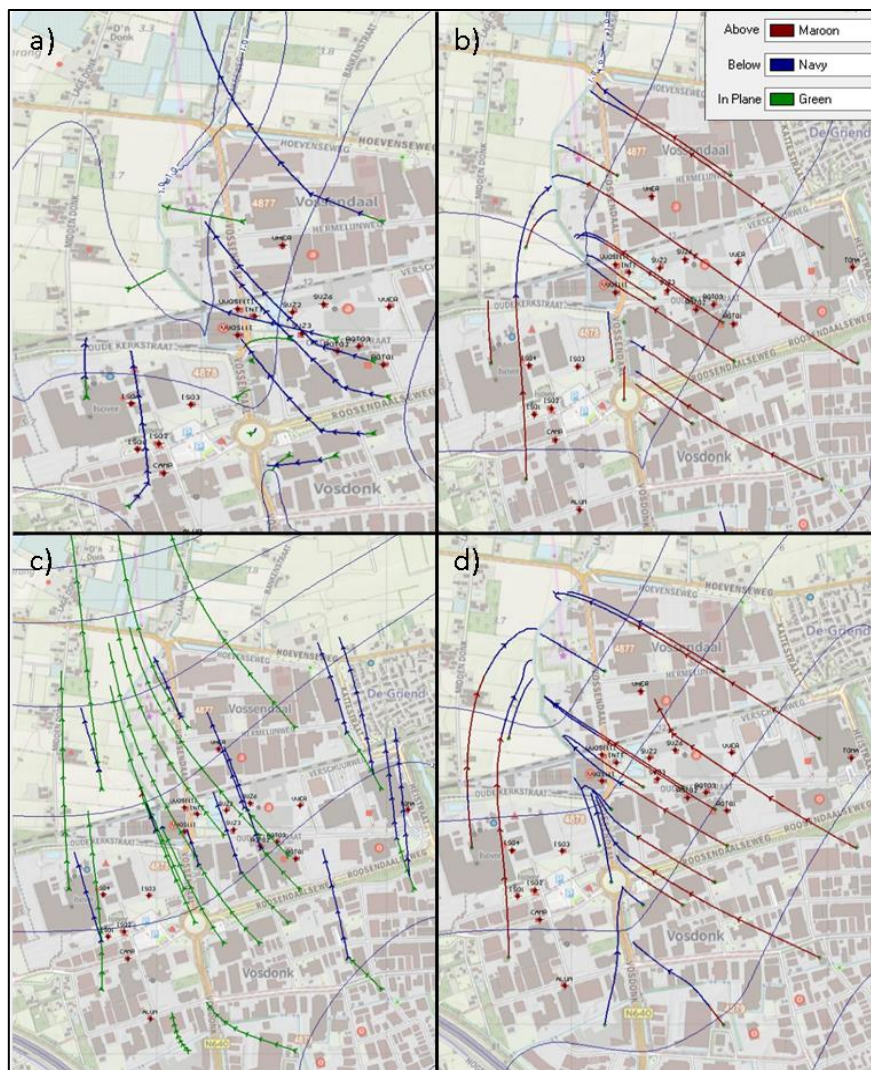


Figure 18: Top view on the groundwater flow with a) and b) layer 1 (Ground level) behaviour of respectively model zero and Krig min and c) and d) layer 5 of respectively Model zero (-10 m N.A.P.) and Krig min (-20 m N.A.P.).

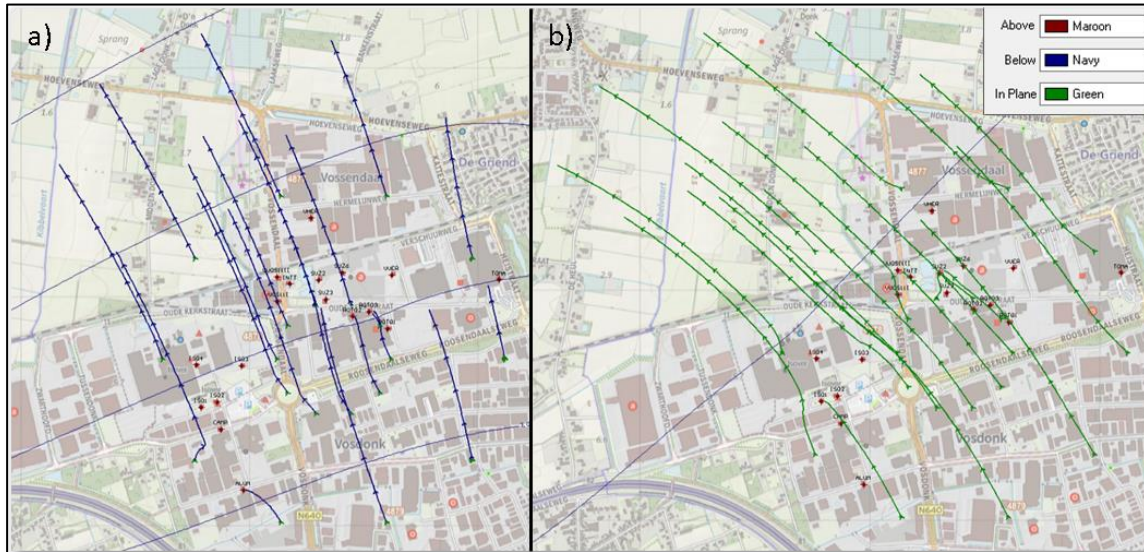


Figure 19: For groundwater model zero, layer 10 (-50 m N.A.P.) in a) presents more or less north direction of groundwater flow direction and b) layer 14 (-145 m N.A.P.) presents north western direction of flow

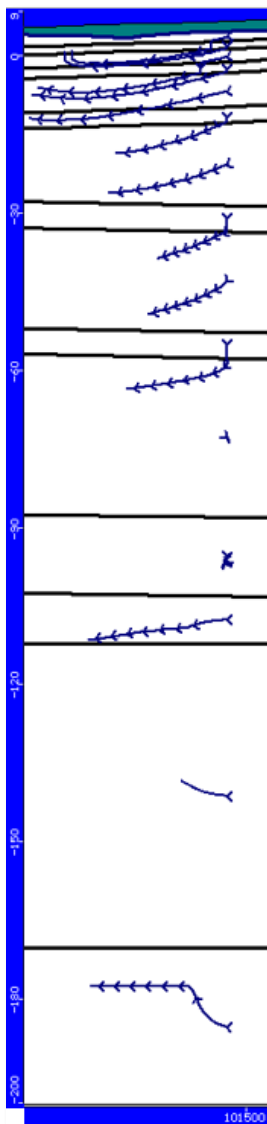


Figure 20: Section view groundwater particle behaviour model zero.

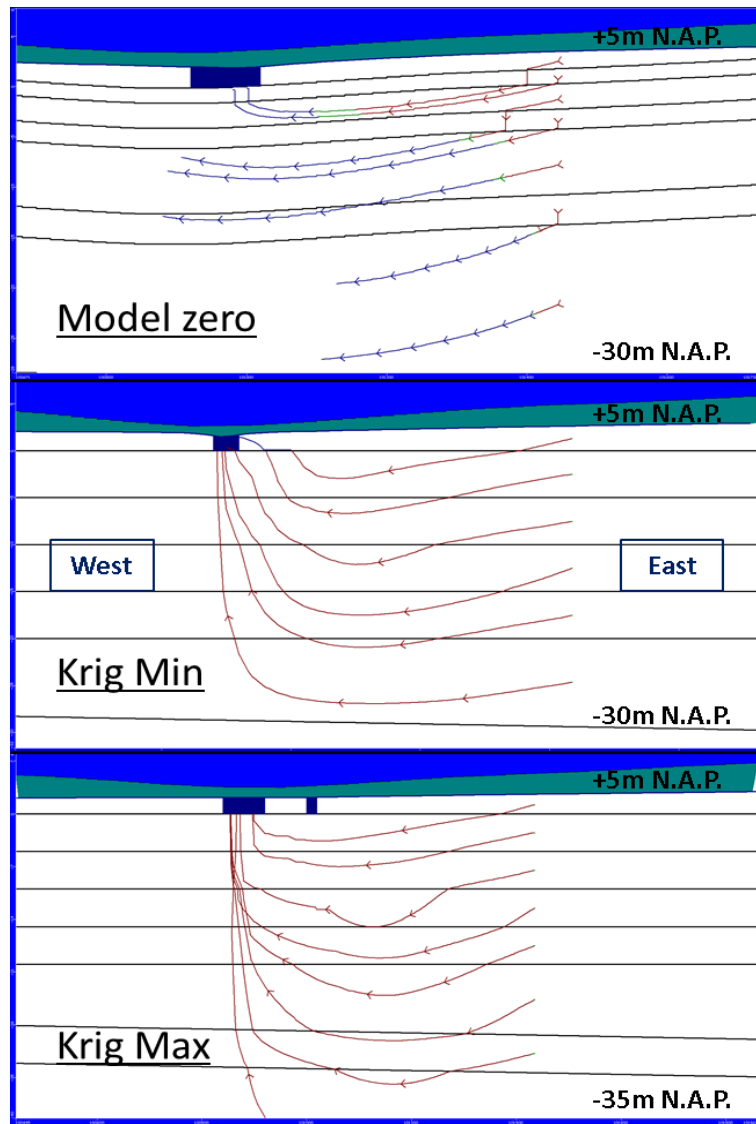


Figure 21: Section view of the groundwater flow particle behaviour of the shallow subsurface layers.

The modelling results for the deeper layers reflect the presence of the industrial and drinking water extraction. A slight north-western movement is noticed around -50 m N.A.P., which is caused by the drinking water extractions at the west side of the model. These drinking water extractions create a clear north-western flow at depths of around -145 m N.A.P. The movements of the flow are presented in Figure 19a and Figure 19b. The industrial extractions catch the flowline located most south in Figure 19. This is also noticed in Figure 20. Flowlines in the deeper layers stop after a short amount of time, which indicates they did flow into a well. The water extractions clearly influence the flow in deeper layers. The groundwater flow in mid and upper range layers do not have a noticeable influence, which could be explained by the presence of the deeper continuous clay layers compensating the effect of these extractions.

The kriged models and groundwater model zero show differences in direction and speed of the flow. This is observed in Figure 21. The effect of the river is visible, which was already seen in Figure 18. Model krig max even attracts flow from beneath the first continuous aquitard, which starts at -30 m N.A.P. This is considered a point of discussion. The river can extract groundwater flow from the top and mid-depth layers, which is shown particularly in the kriged models. Again, the consequence of one open top aquifer is presented. The travel times of the flow are influenced by the different hydraulic conductivities and layering in the models, which includes lower travel times for the kriged models in comparison to the groundwater model zero.

Coming back at the point of discussion, the krig max model illustrates a very permeable situation. The river extracts flow until a great depth through one of the main aquitards with a continuous low conductivity, which can be considered unrealistic. Detailed river data is collected from the Waterschap Brabantse Delta and is assumed correct and accurate. These parameters are implemented into the model exactly as delivered, which means the modelled intrusion influences at the river should be acceptable. Maybe the 10-meter minimum horizontal width for the impermeable layers is a too harsh assumption, although gathered from the literature. This possibly creates a too conductive aquifer. The chance for an overestimation is present, which could give faster travel times and probably faster solute transport as in practice. Extra knowledge about a possible overestimation was gathered, which is still considered safer as underestimating permeable situations.

Another influence is related to the interpretation of the horizontal hydraulic conductivity. The groundwater model zero showed to have less sensitivity to varying the horizontal hydraulic conductivity than varying the vertical hydraulic conductivity. The consequence is the possibility for an input error in the groundwater model zero, which results in lower or higher horizontal travel velocities. The kriged models should include a more accurate hydraulic conductivity compared to the “pancake” methodology in groundwater model zero, because it is directly interpreted and used from CPT data. As was just mentioned, the collected river data is assumed correct and accurate. This means no false influences on the horizontal hydraulic conductivity should result from the river data. The groundwater model zero flow travels slower as the groundwater flow of the kriged models, which is still a logical outcome. It slows down due to a lot of clay layer disruption, where less clay layer disruption is present in the kriged models and the flow can find a way around the impermeable subsurface spots.

4.3 1D Solute Transport

This section consists of four sections with results regarding the 1D solute transport. The first section gives an overview of the flow directions and locations of the studied flowlines and also includes the differences between the random simulations. The second part includes the solute transport reaching a certain object. The object consists of a specified travelled distance on the flowline or the river Laaksche Vaart. The third part gives a view on the evolution of the concentration of the contaminants at different time steps over the full-length of the flowline. At last, the probability of the travelled distance of the front of the contaminant plume is examined.

4.3.1 Flowline locations: flowline behaviour of the random simulations

The randomly simulated flow lines form groups of path directions around the krig max and krig min model. This is observed in Figure 22. The grouping forms two main paths resulting in a difference in path length and direction. Hydraulic conductivities prove to influence path behaviour, which is illustrated in Figure 24b and Figure 24c. Flowlines in the krig min model need more effort to choose a path compared to krig max, which has more “wobbly” characteristics. The groundwater model zero shows even more difference in path behaviour because it includes more lower conductivity areas. This is presented in both Figure 23 and Figure 24. Especially flowline 2 presents the effects nicely. The characteristics of the hydraulic conductivity could affect the chosen pathway, but there is also a chance that it results from the low amount of random simulations.

The generated flow lines show a difference in velocity between the kriged models and groundwater model zero. This was expected considering the groundwater flow results. The influence of the clay layers and absence of inflow in the river is clearly noticed for groundwater model zero, which is presented in Figure 24a. For krig min, some disrupted behaviour from lower hydraulic conductivity zones is shown and the krig max model displays quite permeable behaviour. Both flowlines from the kriging model flow into the river. These observations are made in Figure 24b and Figure 24c. The same reasons explain this behaviour as in the groundwater flow results. The difference in flow path behaviour, considering the path and velocity, are going to be noticed in the results for the 1D solute transport.

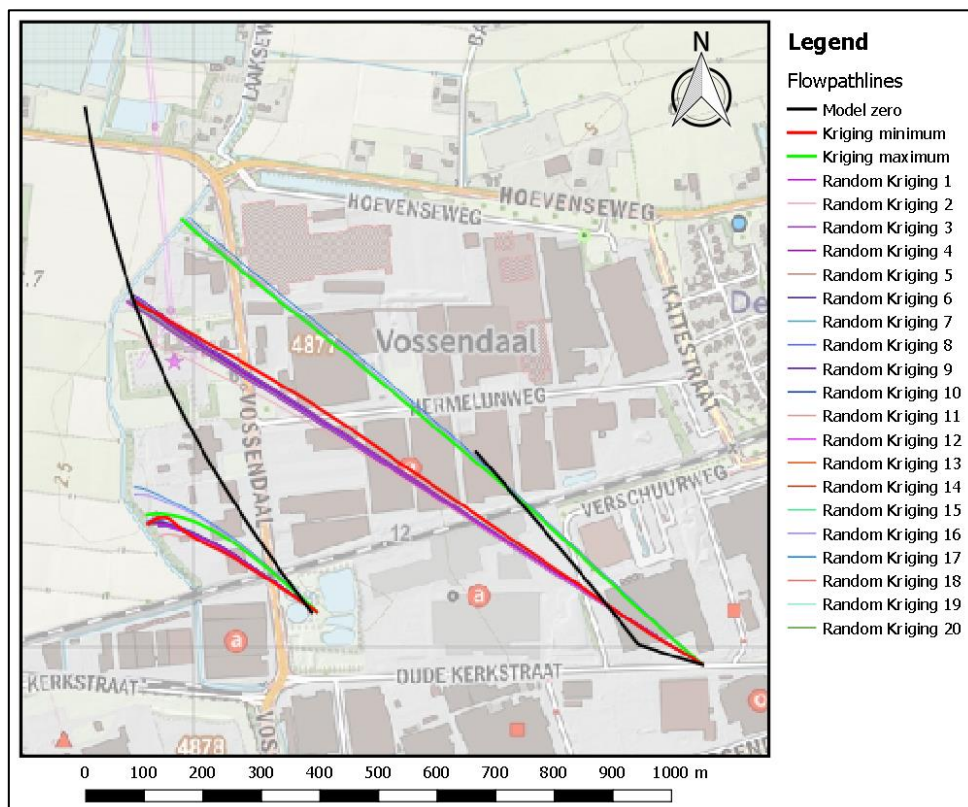


Figure 22: Top view on the flowlines from the random simulations.

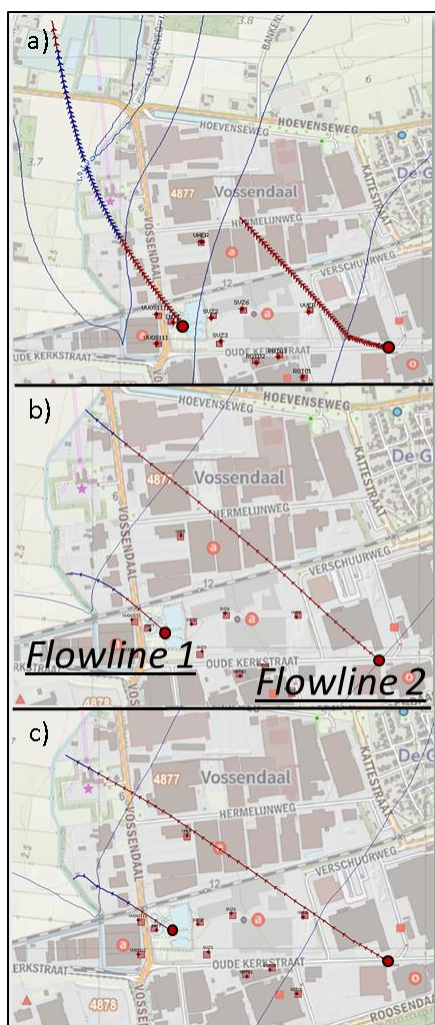


Figure 23: Top view of the behaviour for Flowline 1 and 2 in a) Model zero, b) Krig Min and c) Krig max. Marker = 1 year elapsed

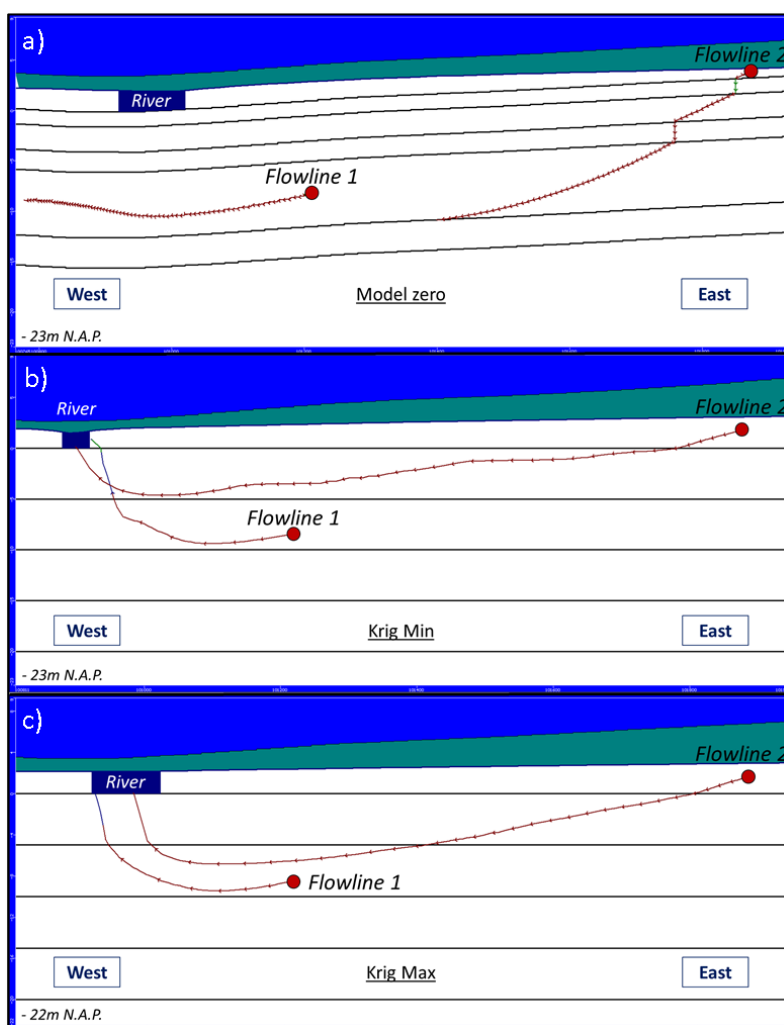


Figure 24: Section view for Flowline 1 and 2 in a) Model zero, b) Krig Min and c) Krig max. Marker = 1-year elapsed time.

4.3.2 Solute Transport: examining objects

The arrival times of ethene indicate a high time difference of arrival of contaminants between the model zero and kriging models. This time difference of arrival includes 30-35 years. The river Laaksche Vaart and a 175 meter-travelled distance are taken as the objects. Figure 25 presents the results. Ethene is the only contaminant reaching the river for groundwater model zero. The flowline from groundwater model zero does not flow into the river, which is important to mention. This is illustrated in Figure 24, but Figure 19 already presented the almost nihil chance for the groundwater flow to reach the drinking water extractions within 50 years in case the rivers do not attract the flow. The location under the river represents the object. For a chosen object of 175 meters travelled distance the differences in arrival times are more or less the same, which indicates that using a location under the river gives more or less the same output. The locations at which the models arrive at the objects differ. This happens mainly between groundwater model zero and the kriged models, which creates the biggest part of the difference in arrival time. Flow speed differences take into account the other part of the difference in arrival time. In conclusion, these are, as was expected, the two most important influencers creating arrival time differences at the object and are related to the variability in hydraulic conductivity and pathway of the flowlines.

Noticeable differences in flux values are present between the groundwater model zero and kriging models, but also between the individual random simulated kriging models. The differences between the random simulations are explained by the flow speed of the contaminant at the location of inflow at the object. A slower inflow and so lower hydraulic conductivity results in a lower flux and vice versa. This is especially noticed for trichloroethene and cis-1,2-di-chloroethene in Figure 25 and Figure 26.

The differences in flux between the groundwater model zero and kriged model have to do with the later inflow time. The decay has a longer time to attenuate the contaminants, which results in lower contaminant concentration values for the flowlines of groundwater model zero. Secondly, the inflow speed for the flowline of groundwater model zero below the river is most certainly lower, because of the presence of more force on the flow close to the river. The properties of flow around the object influence flux value highly.

The inflow of contaminants in the river Laaksche Vaart is possibly happening at this moment. Concentration measurements did not yet show active concentrations around the river in 2009 at concentration well log N5. This is also the case for the modelled 1D solute transport in Figure 25a, which gives a small verification for arrival times in the model. It is important to consider a possible infiltration of contaminants into the river Laaksche Vaart, because the results of Figure 25a indicate a presence of contaminant particles around this river in current years.

For flowline 2 the time difference between the models, considering the contaminants reaching the object, is around ten years smaller compared to the time differences for flowline 1. An overview is given in Figure 26. The impact of the hydraulic conductivities must still be present because the flowline starts from ground level. This gives differences in pathway and flow speeds, which was observed in Figure 23. The top views of the pathways are quite similar, so the only remaining significant influence results from the draining effect of the river. The 100-meter point for flowline 2 is located much further from the river, which probably explains the smaller time differences. The river attracting the flow can have a high influence on the travel times as long as the flow is close enough to the river, but the hydraulic conductivity remains to be the main influencer.

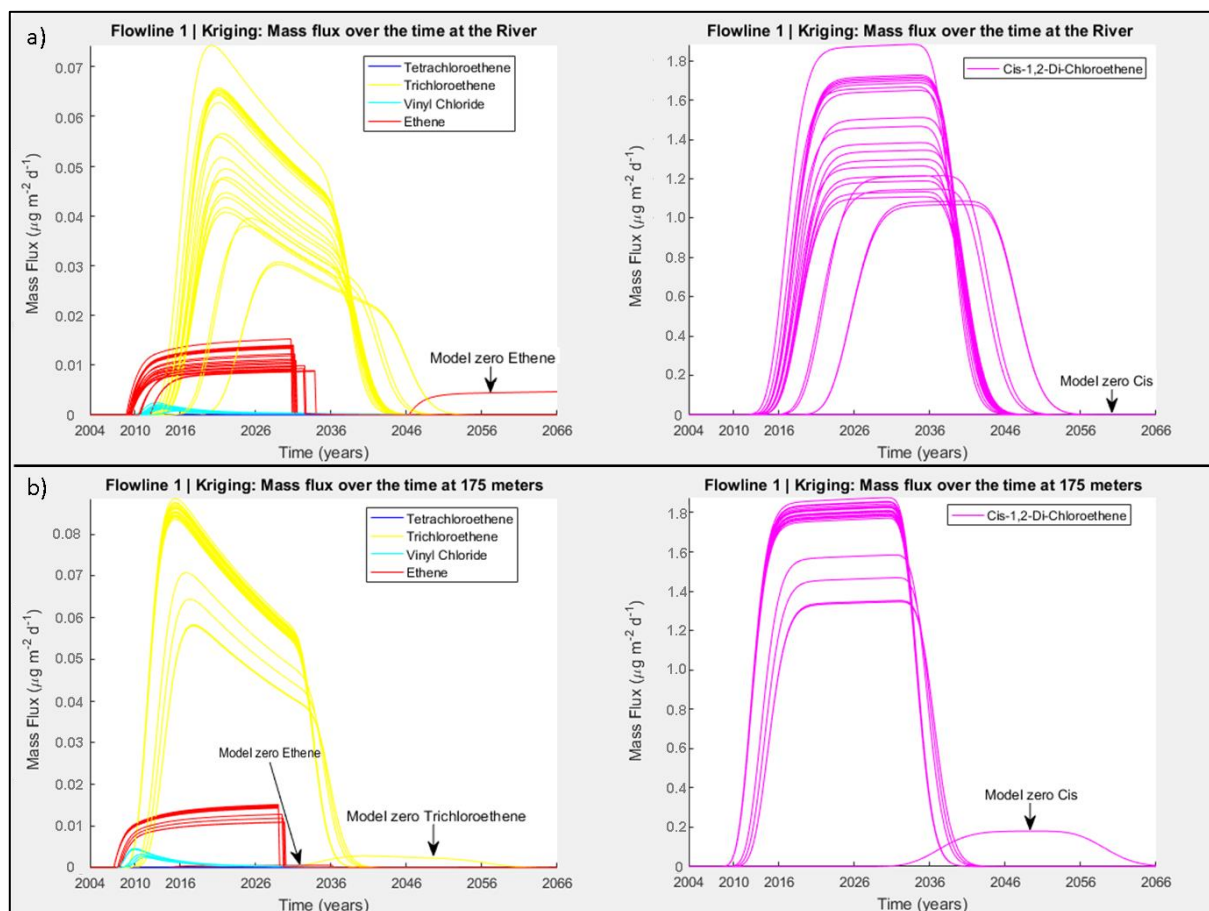


Figure 25: Flowline 1 object examination with a) the river Laaksche Vaart and b) the specified 175 m distance on the path.

The flux inflow values for trichloroethene and cis-1,2-di-chloroethene are quite high for respectively flowline 2 and flowline 1 and 2. At the peak, a flux inflow of on average 1.5 to 2.5 $\mu\text{g m}^{-2}\text{s}^{-1}$ flows inside the object. This inflow is probably present for a long duration of time, because of the duration the contaminants are released in the subsurface. It is important to examine the effects of this inflow on for example the river Laaksche Vaart.

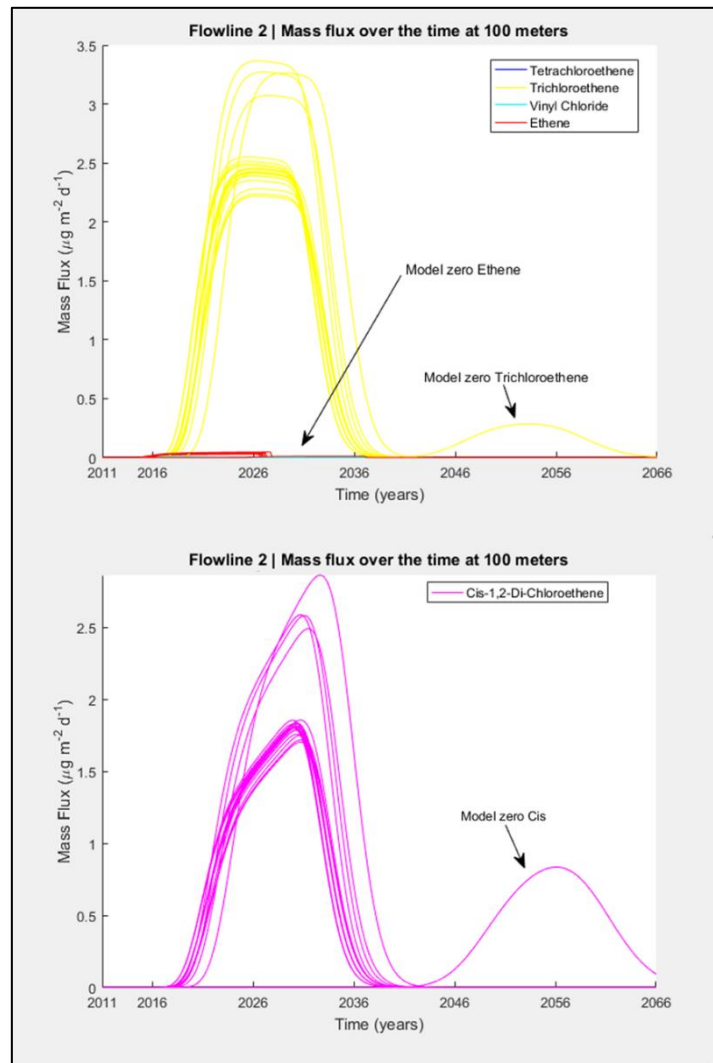


Figure 26: Flowline 2 object examination for a 100-meter path distance.

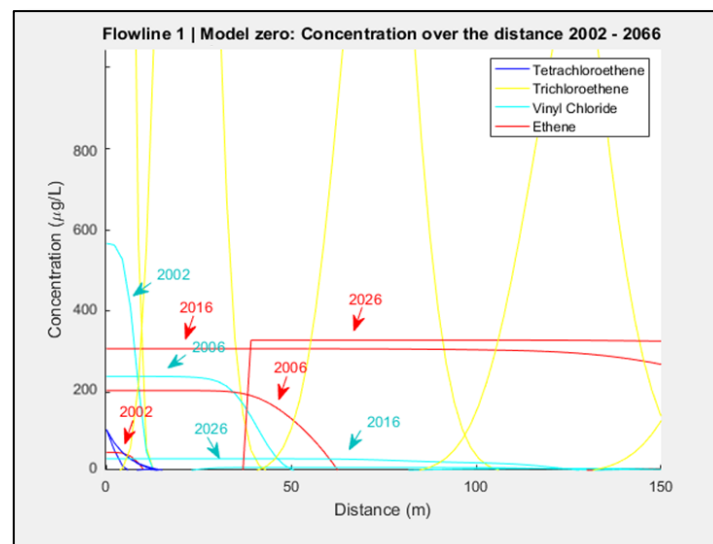


Figure 27: Zoom in on the behaviour of vinyl chloride and ethene.

4.3.3 Solute transport concentration evolution over time

The results of Figure 27, Figure 28, and Figure 29 represent a concentration value on the y-axis instead of a flux value. This choice is made to get insights in the modelled amounts of solute concentration over the distance of the flowline. No object is stated to be reached, which makes the solute concentrations more interesting.

The strong effect of decay on trichloroethene is visible looking at the progression over time. Figure 27 and Figure 28 present this effect. Over the range of 60 years, the concentration decreases with a percentage of 80%. This strong decay is favourable for natural attenuation. Small amounts of trichloroethene could attenuate to acceptable concentrations by the environment, but need to keep within acceptable boundaries of travelled distance.

The high decay values of trichloroethene result in a high generation of cis-1,2-di-chloroethene, which is not characterized by high decay rates. A buildup of cis-1,2-di-chloroethene arises. Figure 29b presents this situation, where the concentration for model zero rises during all 60 simulated years. In Figure 28b an increase is presented until 2036. After 2036 the generation of the contaminant is lower as the effect of the decay, which results in a small decrease in concentration. The back of the plume arrives and concentration levels of the upper component in the system leave, which explains the fact of less generation of contaminant particles from the upper component. The difficulties considering cis-1,2-di-chloroethene indicate a continuous spread of high concentration over the coming decade, which cannot be attenuated by the environment.

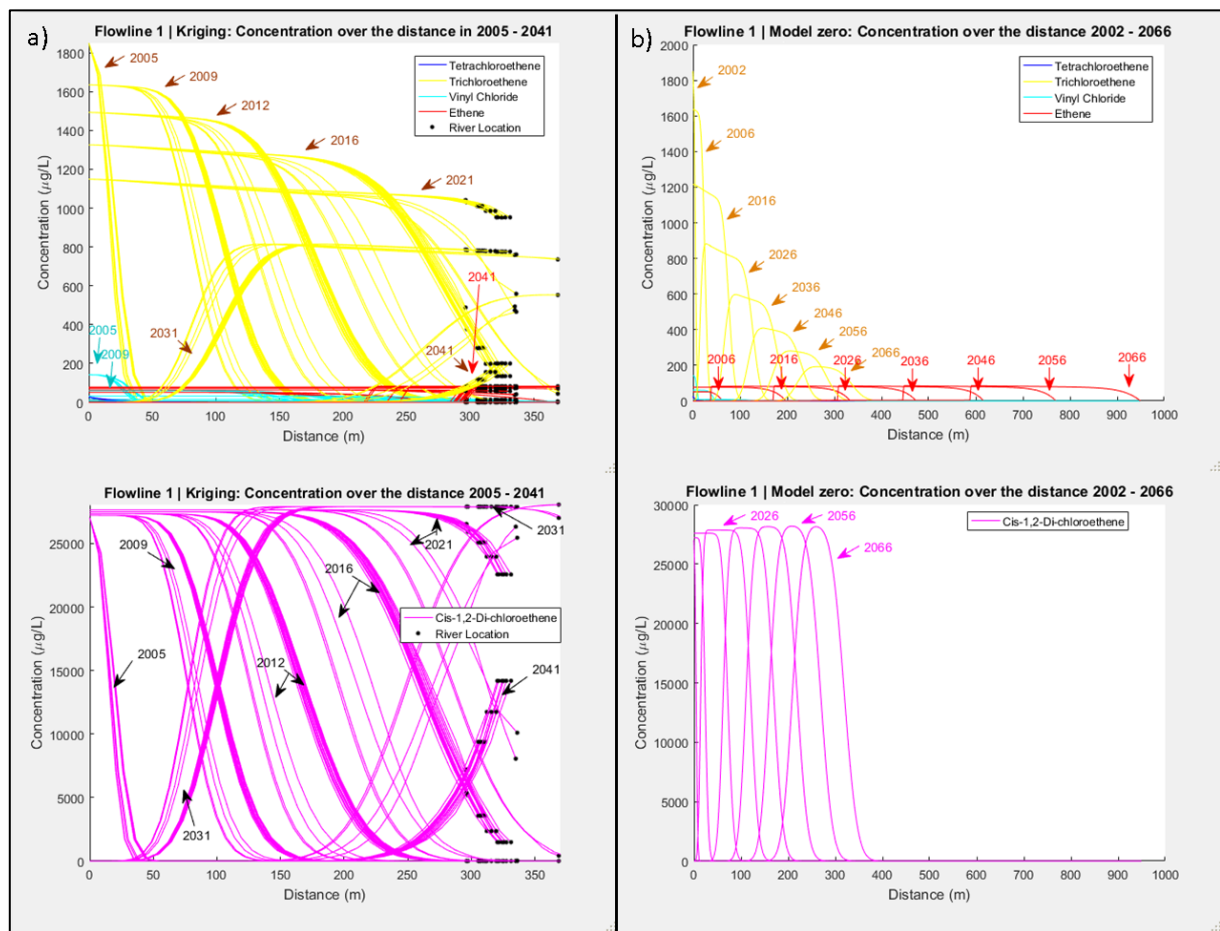


Figure 28: Flowline 1 concentration time steps over the distance for a) kriging models and b) model zero.

Vinyl Chloride is a fast disappearing step in the biological solute transport process and generates the increasing concentration of ethene. The end product ethene follows from vinyl chloride, which is explained in Chapter 2.3. This process is noticed in Figure 27 and Figure 29b. The fast decay of vinyl chloride results in the generation of ethene, which explains the steep curve at the back of the ethene plume. Suddenly a small amount of vinyl chloride is transferred to ethene because the start concentration attenuated and the back of the ethene plume has arrived. Ethene is not harmful to human kind or the environment, which means no problems arise from this remaining component. This was also mentioned in Chapter 2.3. The environment attenuates vinyl chloride within approximately 20 years. The small amounts of vinyl chloride generated from the decay of cis-1,2-di-chloroethene are also attenuated quickly. The low retardation value of vinyl chloride results in short travel distances, which indicates, in combination with the decay properties, the environment could naturally attenuate vinyl chloride.

The solute transport model presents a nice overview of the front and back of the contaminant plumes. In Figure 28a the end of the 2005 plume and beginning of the 2031 plume are located at almost the same distance. They indicate the time length of the contamination plume. The length of the contaminant plume is estimated around 25 to 30 years.

The kriged models and model zero give notice of differences in the travelled distance again. Most of the kriged model contaminants of flowline 1 reach the river around 2016, which is presented in Figure 28a. Flowline 1 of model zero arrives below the river around a travelled distance of 450 meters, which is only reached by ethene. Results are presented in Figure 28b. Most contaminants of the kriged models in flowline 2 travelled one kilometre or more from start to the year 2066. The contaminants in

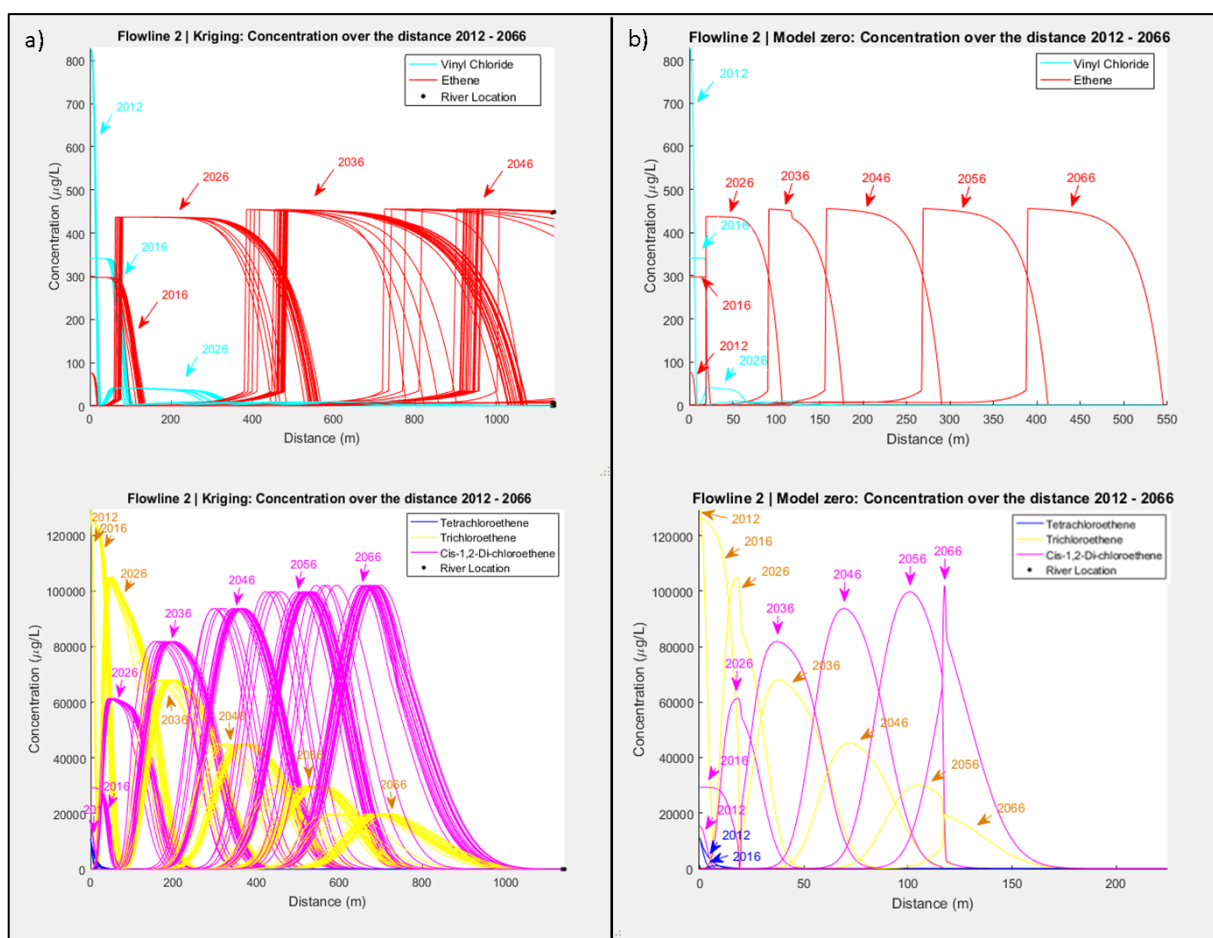


Figure 29: Flowline 2 concentration time steps over the distance for a) kriging models and b) model zero.

model zero travelled much less distance during this time. This is illustrated in Figure 29. The noticed differences in travel distances between the models are the most important part of these results. The numbers of years and travelled distances presented have to be taken with great caution because the 1D solute transport model is a very limited representation of the practical situation. This is further discussed in Chapter 4.4. The influence of the interpretation of the subsurface characteristics presents itself again, due to the observed differences between the kriged models and model zero.

4.3.4 *Probability curves of the contaminants travelled distances*

As time progresses, an increase in differences of travelled distance arises between model zero and the spread of distance of the kriged models. This is illustrated in Figure 30. The arrows indicate the travelled distances of model zero and the probability distributions relate to all the kriged models. The same indications considering the difference in travelled distances is found again, which results in confirmation after confirmation for the effects of hydraulic conductivity subsurface characterisation.

The progression in travelled distance for flowline 1 displays a probability of the contaminants reaching the river at this moment, which is based on kriged models only. Figure 30a presents this. In earlier results from Figure 25a, this situation was already noticed. The peak of the probability distributions is quite low. The probability of the travelled distance at the peak is only 2.5% to 6%. This indicates a probability of 94% to 97.5% that specific travelled distance has not occurred. To state if a contaminant has reached the river a big part of the probability distribution needs to pass this travelled distance, otherwise the total probability is too low.

The probability of ethene reaching the river only results from the kriged models of flowline 2. Cautious statements need to be given for these far travelled distances, due to the limitations of the solute transport model. The probability distribution presents ethene reaching the river around 2056 for the 1D solute transport model used in this research. Still, the probability distribution shows a considerable area of possible travelled distances before the river. The same principle for chances applies as just discussed. No certainties are given on the arrival of ethene at the river for flowline 2, due to the assumptions made in the 1D solute transport model

The contaminant probability distance distributions distribute more or less normally at the start of the contaminant flow, but skew to the right and even show bimodal behaviour as time progresses. The bimodal behaviour is expected to result from the differences in path direction, which arises as the flow paths progress forward. The gap between krig min and krig max arising as explained in Chapter 4.3.1, creates the gap in the probability distribution. Although the presence of a small number of random simulations, flowline 2 shows a quite clear view of grouping. This indicates the possibility for this situation to occur in practice. The differences in the height of the probability curves can be questioned, due to the lack of a high number of random simulations. The surrounding subsurface characteristics influence the shape of the probability curves as time progresses.

The uncertainty of the probable travelled distance increases over time, which the width of the probability distribution curves represents. This is presented in Figure 30. For example, ethene consists of a width of 500 meters in 2036 after a width of only 60 meters in 2016. Tetrachloroethene stays stable around 45 meters from the beginning onwards because the decay prevents it from reaching further as 45 meters. Tetrachloroethene also consists of a property of continuous inflow. Higher uncertainty in the travelled distances of the front of contaminant plumes arises as time progresses, because of the difference in subsurface characteristics between the kriged models.

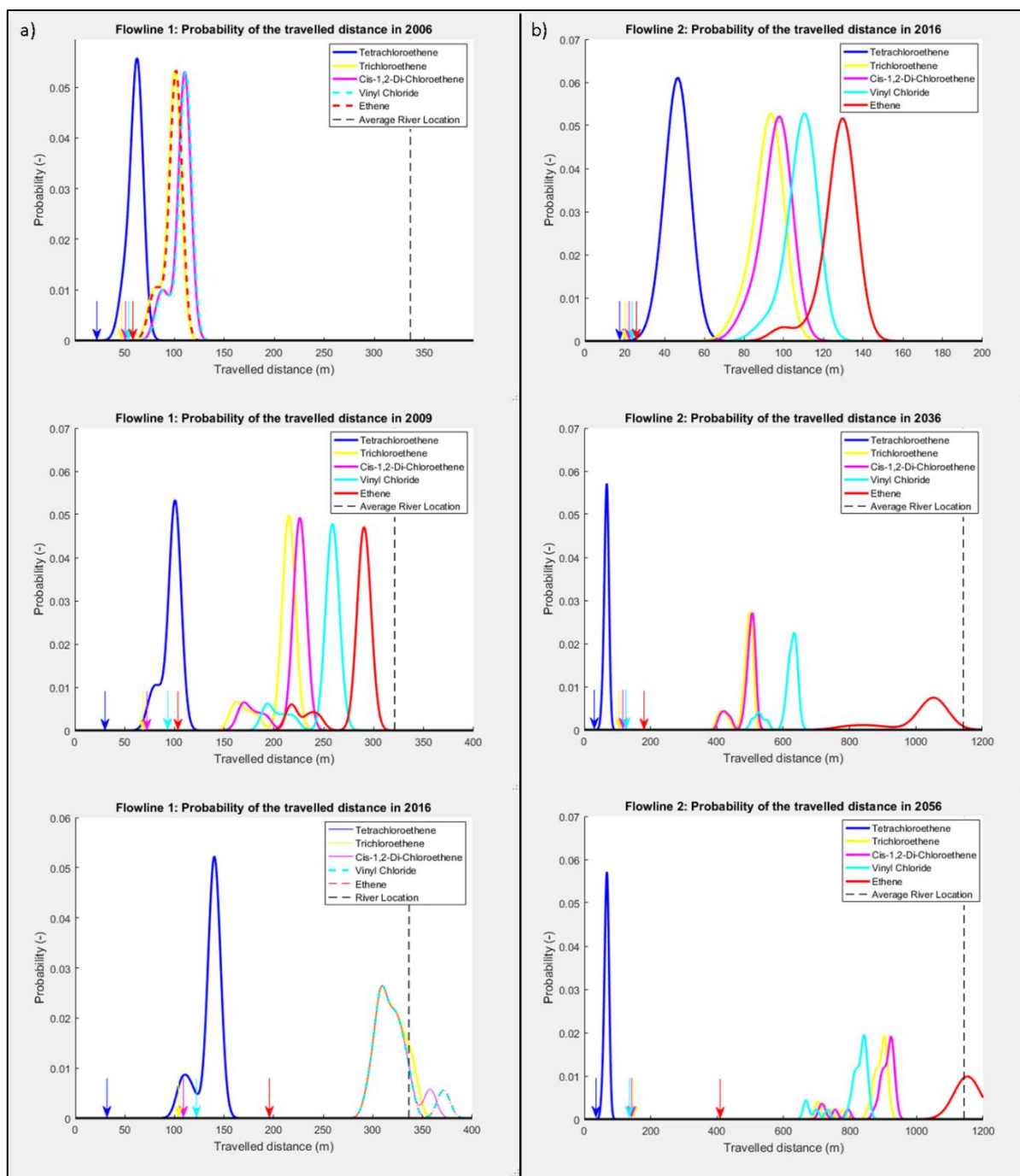


Figure 30: Probability curves of travelled distance for a) flowline 1 and b) flowline 2.

4.4 General points of discussion

Although the presented work only evaluates the uncertainty in the hydraulic conductivity other parameters influence the subsurface groundwater flow and solute transport as well. The impact of these parameters on our results can include an additional influence on the characterisation of the subsurface, which could result in for example slightly slower or faster travelled distances of the groundwater and contaminant components. By performing kriging on the average values of the porosity and effective porosity these parameters were included a little bit. Ruling out the other subsurface parameters made it possible to relate conclusions and results to the examination of the hydraulic conductivities. The literature in Chapter 1.1 stated the hydraulic conductivity parameter gives the main influence on the system concerning subsurface heterogeneities, which was the basis for the choice of examining the hydraulic conductivity over the other subsurface parameters.

The choice for a 1D solute transport model resulted in a limitation of the description of reality. In reality processes and contaminant sources are taken into account in 3D throughout the complete project area. A lower dimension 1D interpretation is only taking into account the point in front and after the specified point. Higher dimension interpretations also consider the points to the left, right, bottom, top, etc. An example easily explains the limitation. A contaminant source present at the left of 1D solute transport modelling is not taken into account in the calculation but would have been implemented in the calculations for a 3D model. The disadvantage of these higher dimension solute transport models consists of its complexity and time-consuming process. It was impossible to construct a higher dimension model in this research, because of the time scope and pre-work for groundwater model zero. To compare both implementation methodologies of the subsurface characteristics there is no urgency for more accuracy, but for more detailed and accurate insights in the contaminant behaviour time should be invested to include the complexity. For now, only the acceptable first indications for the behaviour of the contaminant particles and differences between the implementation of subsurface characteristics can be gathered using the developed 1D solute transport model, but for more accuracy to the real life.

Another limitation of the description of reality arose by disregarding the dispersion in the 1D solute transport governing equation. Adding the dispersion could, for example, result in longer travel distances. The choice to disregard the dispersion term was made, because of the similarities in assumptions and data availability with the research of Heimovaara, Keijzer and Velstra (2004), the complexity of the term and to save time. Heimovaara, Keijzer and Velstra (2004) found the somewhat trivial behaviour of the dispersion term, which resulted from their assumptions and data availability. The importance of the dispersion term in especially solute transport models with higher dimensions arose from the theory of Chapter 2.2. Dispersion takes into account the longitudinal, but also the transversal behaviour of flow, which is very useful in 3D solute transport models. The longitudinal influence indicates that the dispersion term could improve 1D solute transport results. This means it would have been useful to invest time and include the complexity, but was not possible within the time scope of this research. Neglecting the dispersion term is acceptable for the 1D solute transport model in this research but results in unacceptable simplifications for models of higher dimensions.

Only an amount of 20 random simulations were conducted, which is a small amount considering the possibilities in the variability of the subsurface characteristics. Increasing the number of simulations can result in a change of the shape and height of the probability distribution curves. Conclusions concerning the heights of the probability curves in Figure 30 are stated unreliable. The probability distributions of the travelled distance give a reliable indication of the spread in travel distance for the contaminants, which was discussed in Chapter 3.4.3. The difference in paths behaviour also gives indications for the possibilities of bimodal shapes.

5 Conclusion & Recommendations

This research created insights for the groundwater flow and contaminant behaviour in the area Vosdonk Noord at Etten-Leur in the Netherlands. Throughout this process, the gathered knowledge about the interpretation of the shallow subsurface heterogeneity mainly focused on the hydraulic conductivities. A comparison in groundwater flow and solute transport results was made using the kriging interpolation method to implement subsurface CPT data directly into the model. This generated a cell by cell implementation of the subsurface characteristics. In practice, the “pancake” method characterises the subsurface in commercial software like Visual Modflow. The gathered knowledge is useful to try and tackle this in practice used “pancake” method in case of a highly heterogenic subsurface.

The difference in implementation of the subsurface heterogeneity creates a clear difference in effects on the behaviour of groundwater flow and solute transport, which was reviewed by using the kriging and “pancake” methodology. Higher and lower hydraulic conductivity regions arise in the clay layers of the shallow subsurface for the kriging approach, which implements cell by cell subsurface data directly into the model. These conductivity regions are not present in the “pancake” method, which approaches the subsurface with continuous horizontal clay layers. Clear differences in output are found between the two approaches, which was noticed in multiple results from Chapter 4. Groundwater and contaminant behaviour, especially closer to the river, are also influenced differently by the strong draining effect of the river, which is related to these differences in methodology. This includes changes in the travel direction and travel velocities. The main difference in the results comes from the higher and lower hydraulic conductivity regions in the subsurface, which create one big open top aquifer in the kriging models.

The horizontal conductivity appeared to be a difficult parameter. This gives influences on the results of the greatness of differences between the implementation methods of the subsurface characteristics. The variability could also be slightly influenced. The impact of the hydraulic conductivity on the calibration of the “pancake” model is very low, which makes it sensitive to input errors. Horizontal flow speeds are related to this conductivity parameter. The kriging situation with the maximum variability values showed the unrealistic deep extracting behaviour of the flow towards the river. This is related to a possible overestimation of the characteristics of the impermeable layer widths, which van Alphen (1984) presented. The situation in practice can probably be estimated somewhere in between the kriging and “pancake” implementation methodology.

The solute transport of the kriged models shows the possibility for contaminants to flow in the river Laaksche Vaart at this moment. For model zero the solute transport arrival times at the river were only noticed for ethene. Large differences also arise for arrival times of the solutes transport, which is again related to the big differences in subsurface interpretation between the kriging and “pancake” method. There is a presence of higher uncertainties for larger travelled distances of contaminant, because during the progression of time the range of the probable travelled distances increases. A higher amount of random simulations could improve this range of uncertainty. Due to the lack of a higher amount of these random simulations no certainties can be given for the height of the probability peaks, but the indications on the range of travelled distance are acceptable. High concentrations and low decay properties of cis-1,2-di-chloroethene prevent the environment from naturally attenuating this component, which makes it the contaminant to examine further. Although no certainties on exact values can be given using this 1D solute transport model, the contaminant behaviour in and around the river Laaksche Vaart should be evaluated for mainly cis-1,2-di-chloroethene.

It is impossible to use the 1D solute transport model as a representation of reality, because of the applied simplifications. Including 3D modelling and dispersion, can already give a much better representation of reality. These add much complexity to the model. They could not be included, due to the time scope of this research. Although the great simplification of the 1D solute transport model, it can give a first general indication of the behaviour of the contaminants.

The groundwater and contaminant flow will not come close to the restriction boundary at the drinking water extractions of Seppe. The flow follows a north direction in upper and middle layers and a north-western movement in the deeper layers. Only the flow starting below -80 m N.A.P. has a small possibility to reach the drinking water extractions at Seppe, but the movement is too slow to exceed the applied boundary restrictions from Arcadis (2012).

New opportunities arise from this research. The groundwater model zero delivers a good starting point for new research and the points of discussion give options to improve the results. The following subjects and components are suitable recommendations and interesting for further research:

- Improving the horizontal hydraulic conductivity parameter and implementing more subsurface parameters into the kriging implementation methodology. This results in an improvement of the cell by cell implementation of the subsurface heterogeneity for the Nuenen Group.
- Expansion of the 1D solute transport model to a 2D and preferably 3D model. This must be combined with a dispersion component in the governing equation.
- Expanding the number of random simulations, to get more insights from the probability distribution curves of the travelled distances and more insight in the flow path behaviour of the random simulations.
- Monitor the contamination concentration values in and around the river Laaksche Vaart. This should give more insights in the real-life situation at the river. It is advised to monitor the presence of contaminants behind the river in the first 30 meters depth. This gives possibilities to validate results concerning the big open top aquifer, which results from the kriging implementation. In case contamination flows further into the river, research is necessary to determine effects on the environment and area of Vosdonk Noord.
- To determine the most likely source zone locations. Locating the cis-1,2-di-chloroethene is interesting because the results of this research present the need for man-made attenuation.
- The development of an automated system to interpret CPTs and create box model alternatives. This could increase the accuracy of the transformation process from CPT to Kriging data. Another advantage of an automated system is the quick and easy processing of big data. The transformation process was conducted by hand and is explained in Chapter 3.1.
- An alternative to the Visual Modflow software should be considered. The importation process of big data and the batch run simulation tool caused many problems, which is explained in Chapter 3.5.

By using the data available and maintaining the reliability of the input, as much insights as possible were gathered for the groundwater flow and solute transport. This is accomplished by the development of an implementation methodology using kriging, which can generate a subsurface parameter data set from point sample data and is ready to be imported accurately in Visual Modflow. This methodology could be useful in other groundwater and solute transport tools but needs the possibility to import cell by cell data. Hence, one of the biggest limitations of the commercial software packages, the “pancake” methodology, is possibly tackled. Definitive validation of this implementation method should result from future monitoring data at the project location and further research on the solute transport model. The generation of the scenarios has led to a small increase in reliability and generated much knowledge, but the hypothesis stated as *“Although the lack of detailed information much knowledge can be gathered in the process of generating multiple stochastic “supported” scenarios of the subsurface and using all these individual scenarios in the models to create reliability in the results”* is refuted considering the small number of scenarios used and the further research needed.

6 Bibliography

- Abu-El-Sha'r, Y. W., & Hatamleh, I. (2007). Using Modflow and MT3D Groundwater Flow and Transport Models As a Management Tool for the Azraq Groundwater System. *Jordan Journal of Civil Engineering*, 1, 20.
- AHN. (2017). AHN2 hoogtebestand. Amersfoort, Gelderland, Netherlands.
- Anderson, M. P. (1984). Movement of Contaminants in Groundwater: Groundwater Transport - Advection and Dispersion. In N. A. Press, *Groundwater Contamination* (pp. 37 - 45). Washington D.C.: National Academy Press.
- Arcadis. (2012). *Gefaseerd Deelsaneringsplan voor aanpak integrale grondwaterverontreiniging cluster Vosdonk-Noord te Etten Leur*. 's-Hertogenbosch: Provincie Noord-Brabant.
- Arcadis. (2014). *Casus Waaldijk bij Hurwenen in het Rivierengebied*. Den Haag: Ministerie van Infrastructuur en Milieu.
- Arcadis. (2014). *Geohydrologisch onderzoek doortrekking A15*. Rotterdam: Arcadis.
- ATSDR. (1990). *Toxicological profile for Ethylene Oxide*. Agency for Toxic Substances and Disease Registry, Public Health Service. Atlanta: U.S. Department of Health and Human Services. Opgehaald van <https://www.atsdr.cdc.gov/ToxProfiles/tp137-c1-b.pdf>
- ATSDR. (1996). *Toxicological profile for 1,2-Dichloroethene*. Agency for Toxic Substances and Disease Registry, Public Health Service. Atlanta: U.S. Department of Health and Human Services. Opgehaald van <https://www.atsdr.cdc.gov/ToxProfiles/tp87-c1-b.pdf>
- ATSDR. (2006). *Toxicological profile for Vinyl Chloride*. Agency for Toxic Substances and Disease Registry, Public Health Service. Atlanta: U.S. Department of Health and Human Services. Opgehaald van <https://www.atsdr.cdc.gov/ToxProfiles/tp20-c1-b.pdf>
- ATSDR. (2014). *Toxicological profile for Tetrachloroethylene*. Agency for Toxic Substances and Disease Registry, Public Health Service. Atlanta: U.S. Department of Health and Human Services. Opgehaald van <https://www.atsdr.cdc.gov/ToxProfiles/tp18-c1-b.pdf>
- ATSDR. (2016). *Toxicological profile for Trichloroethylene*. Agency for Toxic Substances and Disease Registry, Public Health Service. Atlanta: U.S. Department of Health and Human Services. Opgehaald van <https://www.atsdr.cdc.gov/ToxProfiles/tp19-c1-b.pdf>
- Berendsen, H. J. (2005). *Landschap in delen*. Assen: Uitgeverij Van Gorcum. doi:ISBN 90 23241495
- Bot, A. (2011). *Grondwaterzakboekje*. Bot Raadgevend Ingenieur.
- Brabant Water. (2016). Brabant Model. Breda, Noord-Brabant, Netherlands.
- Chu, D. (2004, July 15). The GLOBEC Kriging Software Package EasyKrig3.0. Retrieved from http://globec.who.edu/software/kriging/easy_krig/easy_krig.html
- Clement, T. P., Hooker, B. S., Sun, Y., & Petersen, J. N. (1998). Modeling Multispecies Reactive Transport in Ground Water. *Ground Water Monitoring & Remediation*, 18(2), 79-92. doi:doi:10.1111/j.1745-6592.1998.tb00618.x
- Cooper, R. M., & Istok, J. D. (1988). Geostatistics applied to groundwater contamination I: Methodology. *Jounral Environmental Engineering*, 114(2), 270 - 286.

- Daya, A. A., & Bejari, H. (2015). A comparative study between simple kriging and ordinary kriging for estimating and modeling the Cu concentration in Chehlkureh deposit, SE Iran. *Arabian Journal of Geosciences*, 8(8), 6003 - 6020. doi:10.1007/s12517-014-1618-1
- de Bruijn, R. G. (2012). *Effectenstudie en vergunningaanvraag warmte/koude opslag Docdata hal 4/5/6 Veerweg 16 te Waalwijk*. Amersfoort: Ingenieursbureau Boorsma B.V.
- Deutsch, C. V. (2002). *Geostatistical Reservoir Modelling*. New York: Oxford University Press Inc.
- Dubrule, O. (2003). *Geostatistics for seismic data integration in earth models* (Vol. 6). Tulsa: Society of Exploration Geophysicists.
- Duineveld, M. (2013). *Geohydrologisch vooronderzoek ZuidasDok*. Nijverdal: IBZ.
- Edelman, D. (2016). *Doorlatendheid uit sondeergrafieken*. Haghorst: RVDE.
- Elfeki, A. M., Uffink, G., & Lebreton, S. (2011). Influence of temporal fluctuations and spatial heterogeneity on pollution transport in porous media. *Hydrogeology Journal*, 20, 283 - 297.
- Ellis, L., & Anderson, S. (2017, July 11). *Tetrachloroethene Pathway Map (Anaerobic)*. Opgeroepen op March 2017, van EAWAG: http://eawag-bbd.ethz.ch/tce2/tce2_map.html
- Fitts, C. R. (2013). Chapter 11 - Groundwater Contamination. In C. R. Fitts, *Groundwater Science (Second Edition)* (pp. 499 - 585). Elsevier.
- Franklin, M. (2014). *Solution to Ordinary and Universal Kriging Equations*. San Fransisco: Researchgate.
- Freeze, A. R., & Cherry, J. A. (1979). *Groundwater*. Upper Saddle River: Prentice Hall, Inc.
- Gaganis, P., & Smith, L. (2005). Evaluation of the uncertainty of groundwater model predictions associated with conceptual errors: A per-datum approach to model calibration. *Advances in Water Resources*, 29, 503 - 514.
- Google. (2017). *Etten-Leur Satellite map*. Opgehaald van Maps.google.nl: <https://www.google.nl/maps/place/Etten-Leur/@51.5759679,4.5724798,23109m/data=!3m1!1e3!4m5!3m4!1s0x47c41f694d684e3d:0x554b370557d3f151!8m2!3d51.5868855!4d4.6671384>
- Gringarten, E., & Deutsch, C. V. (2003). *Methodology for Improved Variogram Interpretation and Modeling for Petroleum Reservoir Characterization*. Austen & Alberta: Landmark Graphics Corporation & University of Alberta.
- Grontmij. (2002). *Bijlage 7: Historie Riolerings*. Prinsenbeek: Tritium Advies.
- Grontmij. (2009). *Effectenberekeningen Aanleg kolk plangebied De Kolk in Wapenveld*. Heerde: Gemeente Heerde.
- Harbaugh, A. W. (2005). *MODFLOW-2005, The U.S. Geological Survey*. Virginia: U.S. Geological Survey.
- Heimovaara, T. J., Keijzer, H., & Velstra, J. (2004). Using inverse modelling in combination with a regional groundwater model to visualize spreading of multiple plumes. *FEM_MODFLOW*, 147 - 150.

- Isaaks, E. H., & Srivastava, M. R. (1989). *An Introduction To Applied Geostatistics*. New York: Oxford University.
- Kleijnen, J. P., & van Beers, W. C. (2005). Robustness of Kriging when interpolating in random simulation with heterogeneous variances: Some experiments. *European Journal of Operational Research*, 165, 826 - 834. doi:10.1016/j.ejor.2003.09.037
- Kumar, C. P. (2012). Groundwater Modelling Software – Capabilities and Limitations. *Journal of Environmental Science, Toxicology and Food Technology*, 1(2), 46 - 57. Retrieved from www.iosrjournals.org
- Kumar, C. P. (2013). Numerical Modelling of Ground Water Flow using MODFLOW. *Indian Journal of Science*, 2, 8.
- Lichtenstern, A. (2013). *Kriging methods in spatial statistics*. Department of Mathematics. München: Technische Universität München. Opgehaald van <https://mediatum.ub.tum.de/doc/1173364/1173364.pdf>
- Ma, Y. Z., & Jones, T. A. (2001). Modeling Hole-Effect Variograms of Lithology-Indicator Variables. *International Association for Mathematical Geology*, 33(5), 631 - 648. doi:0882-8121/01/0700-0631\$19.50/1
- Marache, A., Dubost, J., Breysse, D., Denis, A., & Dominique, S. (2009). Understanding subsurface geological and geotechnical complexity at various scales in urban soils using a 3D model. *Georisk: Assessment and Management of Risk for Engineered Systems and Geohazards*, 3(4), 192 - 205. doi:10.1080/17499510802711994
- MathSoft Inc. (2013). The Empirical Variogram. In S. P. Kaluzny, S. C. Vega, T. P. Cardoso, & A. A. Shelly, *S+SpatialStats: Users's Manual for Windows and UNIX* (pp. 68 - 69). Seattle: Springer.
- Mesic Kis, I. (2016). Comparison of Ordinary and Universal Kriging interpolation techniques on a depth variable (a case of linear spatial trend), case study of the Sandrovac Field. *The Mining-Geology-Petroleum Engineering Bulletin*, 31(2), 41 - 58. doi:10.17794/rgn.2016.2.4
- Mondal, N. C., Singh, V., & Sankaran, S. (2011). Groundwater Flow Model for a Tannery Belt in Southern India. *Journal of Water Resource and Protection*, 3, 85 -97.
- Murphy, B. (2014). PyKrige. Corvallis, Oregon, USA.
- Nipshagen, A., & Praamstra, T. (2007). *VOCL Vluchtige chloorkoolwaterstoffen in bodem*. Rijswijk: SKBodem.
- Noce, T. E., & Holzer, T. L. (2003). *Subsurface exploration with the Cone Penetration Testing Truck*. Menlo Park: U.S. Geological Survey.
- Oliver, M. A., & Webster, R. (2014). A tutorial guide to geostatistics: Computing and modelling variograms and kriging. *Catena*, 113, 56 - 69.
- Petitta, M., Pacioni, E., Sbarbati, C., Corvatta, G., Fanelli, M., & Aravena, R. (2013). Hydrodynamic and isotopic characterization of a site contaminated by chlorinated solvents: Chienti River Valley, Central Italy. *Applied Geochemistry*, 32, 164 - 174.
- Robertson, P. K. (1990). Soil classification using the cone penetration test. *Canadian Geotechnical Journal*(27), 151-158. doi:10.1139/t90-014

- Saba, N. u., Umar, R., & Ahmed, S. (2016). Assessment of groundwater quality of major industrial city of Central Ganga plain, Western Uttar Pradesh, India through mass transport modeling using chloride as contaminant. *Groundwater for sustainable Development*, 2 - 3, 154 - 168.
- Samui, P., & Sitharam, T. G. (2011). Application of Geostatistical Models for Estimating Spatial Variability of Rock Depth. *Engineering*, 3, 886 - 894. doi:10.4236/eng.2011.39108
- Tamma Rao, G., Gurunadha Rao, V., Surinaidu, L., Mahesh, J., & Padalu, G. (2011). Application of numerical modeling for groundwater flow and contaminant transport analysis in the basaltic terrain, Bagalkot, India. *Arabian Journal of Geosciences*, 2(2), 1 - 18.
- TNO. (2017, Januari). DINOloket. Utrecht, Utrecht, Netherlands.
- USGS. (2016). *MT3D-USGS: Groundwater Solute Transport Simulator for MODFLOW*. Opgeroepen op December 21, 2016, van USGS Groundwater information: <http://water.usgs.gov/ogw/mt3d-usgs/>
- van Alphen, J. L. (1984). *Sedimentologische interpretatie van de afzettingen van de Nuenen Groep nabij Best*. Leidschendam: Rijksinstituut voor Volksgezondheid en Hygiëne.
- van Beers, W., & Kleijnen, J. (2010). Kriging for interpolation in random simulation. *Journal of the Operational Research Society*, 54, 266 - 262.
- van Genuchten, M. T., & Alves, W. J. (1982). *Analytical Solutions of the One-Dimensional Convective-Dispersive Solute Transport Equation*. Beltsville: United States Department of Agriculture.
- Wang, K., & Huang, G. (2011). Impact of Hydraulic Conductivity on Solute Transport in Highly Heterogeneous Aquifer. *CCTA 2010, Part 1*, 643 - 655.
- Webster, R., & Burgess, T. M. (1980). Optimal interpolation and isarithmic mapping of soil properties III changing drift and universal kriging. *Journal of Soil Science*, 31, 505 - 524.
- Wiedemeier, T., Swanson, M., Moutoux, D., Gordon, E., Wilson, J., Wilson, B., & Hansen, J. (1998). *Technical protocol for evaluating natural attenuation of chlorinated solvents in groundwater*. Washington DC: USEPA Office of Research and Development.
- Yu, C., Kamboj, S., Wang, C., & Cheng, J.-J. (2015). *Data Collection Handbook to Support Modeling Impacts of Radioactive Material in Soil and Building Structures*. Chicago: Argonne National Laboratory.
- Zeng, X., & Wu, J. (2013). Review of the uncertainty analysis of groundwater numerical simulation. *Chin Sci Bull*, 3044 - 3052. doi:10.1007/s11434-013-5950-8
- Zheng, C., & Wang, P. P. (1999). *MT3DMS: A Modular Three-Dimensional Multispecies Transport Model*. Tuscaloosa: University of Alabama.

Appendix A - Groundwater model zero

The development of a simulation model to aid in the solution of a groundwater problem can be broadly viewed as a procedure that includes four sequential steps. These steps are the model construction, model calibration, model selection from among alternative calibrated models, which in a sense is equivalent to model validation, and model prediction of system behaviour under changed conditions or in the future (Gaganis & Smith, 2005). To be able to create such a model and complete these four sequential steps Kumar (2012) explains the, which is used in this Appendix. The open-source software QGIS is used to manage all the components of data during the development of the model.

A.1 Model Objectives

The area Vosdonk Noord at Etten-Leur does not have any useful groundwater models available. The main objective consists of constructing a suitable groundwater model, which is usable for further research. It needs to be usable in combination with a solute transport model and needs to give insights into the current and past behaviour of the groundwater flow. The possibility to import cell by cell parameter data is also an essential requirement. The client Afvalzorg did request to include the historical extractions of the industrial area and the drinking water extraction system at Seppe. The main focus should be on the industrial area of Vosdonk, which contains the contaminant plumes.

A.2 Hydrogeological Characterization

To understand all the processes going on in the groundwater flow, the hydrological condition and surrounding of Vosdonk-Noord at Etten-Leur need characterisation. The Brabant model delivers much information (Brabant Water, 2016). The company Brabant Water, responsible for the drinking water extractions at Seppe, gave accessibility to this model. It consists of a large geohydrological model of the province Brabant. Maps with isohypse around the project location gave insights into the groundwater flow behaviour. An example of the isohypse in the top region of the subsurface is provided in Figure 31.

Besides the isohypse maps from the Brabant model, Dinoloket (TNO, 2017) and monitoring wells from Afvalzorg are available containing data for the hydraulic heads. This data is used to calibrate and validate the groundwater model. The data contains the hydraulic heads ranging from ground level until a depth of maximum -200 m N.A.P. In Table 9 the ID of all the hydraulic head observation points for 2014, 2015 and 2016 are given. The IDs starting with B are from Dinoloket. The other hydraulic head observation points are from Afvalzorg. The add-on, for example -3, indicates the third screen in the monitoring well.

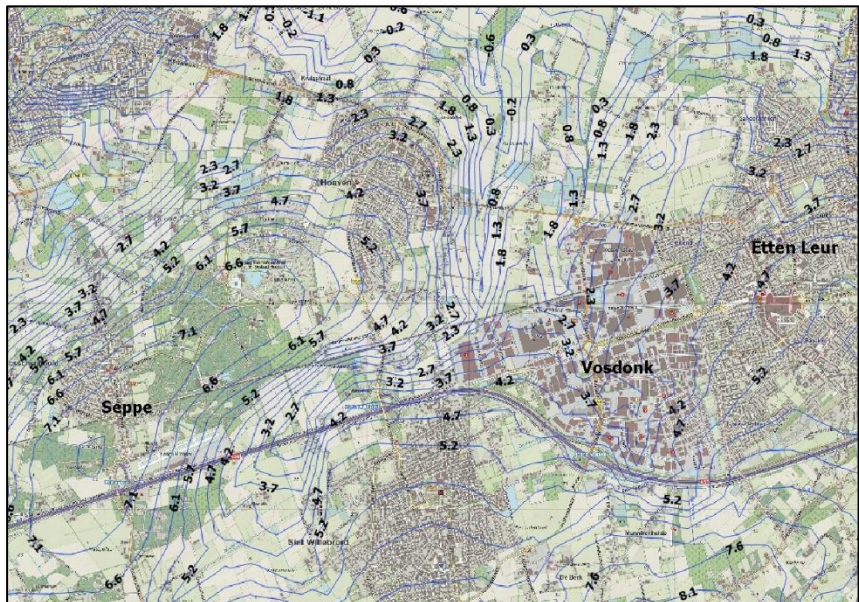


Figure 31: Example of the map with isohypsen in the first subsurface layer from data of the Brabant model

<u>The observation year 2016</u>			<u>The observation year 2015</u>			<u>The observation year 2014</u>		
<i>Well ID</i>	<i>X [m]</i>	<i>Y [m]</i>	<i>Well ID</i>	<i>X</i>	<i>Y</i>	<i>Well ID</i>	<i>X</i>	<i>Y</i>
1619-1	101462	397787	N-09-1	100831	398012	N-09-1	100831	398012
1619-2	101462	397787	N-09-2	100831	398012	N-09-2	100831	398012
1619-3	101462	397787	N-09-3	100831	398012	N-09-3	100831	398012
1619-4	101462	397787	N-13-1	101106	398265	N-13-1	101106	398265
1619-5	101462	397787	N-13-2	101106	398265	N-13-2	101106	398265
2716-1	101597	398125	N-13-3	101106	398266	N-13-3	101106	398266
2716-2	101597	398125	N-13-4	101106	398266	N-13-4	101106	398266
2716-3	101597	398125	N-13-5	101106	398266	N-13-5	101106	398266
2717-2	101514	397963	N-14-1	101445	398392	N-14-1	101445	398392
2717-3	101514	397963	N-14-2	101445	398392	N-14-2	101445	398392
2717-4	101514	397963	N-14-3	101446	398393	N-14-3	101446	398393
2717-5	101514	397963	N-16-1	101846	398477	N-16-1	101846	398477
2931-2	101778	397971	N-19-1	102162	398073	N-19-1	102162	398073
2931-3	101778	397971	N-19-2	102162	398073	N-19-2	102162	398073
2931-4	101778	397971	2714-2	101145	398108	1619-1	101462	397787
N-08-3	101623	397989	2714-3	101145	398108	1619-2	101462	397787
N-09-1	100831	398012	2714-4	101145	398108	1619-3	101462	397787
N-09-2	100831	398012	2717-2	101514	397963	1619-4	101462	397787
N-09-3	100831	398012	2717-3	101514	397963	1619-5	101462	397787
N-10-9	101212	398038	2717-4	101514	397963	2716-1	101597	398125
N-13-1	101106	398265	2717-5	101514	397963	2716-2	101597	398125
N-13-2	101106	398265	2931-2	101778	397971	2716-3	101597	398125
N-13-3	101106	398265	2931-3	101778	397971	N-08-3	101623	397989
N-13-4	101106	398265	2931-4	101778	397971	N-20-1	101238	397925
N-13-5	101106	398265	1619-1	101462	397787	N-20-2	101238	397925
N-14-1	101445	398392	1619-2	101462	397787	N-20-3	101238	397925
N-14-2	101445	398392	1619-3	101462	397787	N-20-4	101238	397925
N-14-3	101445	398392	1619-4	101462	397787	B49F0014-1	97332	397137
N-16-1	101846	398477	1619-5	101462	397787	B49F0017-1	97543	397189
N-19-1	102162	398073	2716-1	101597	398125	B49F0026-1	97722	397242
N-19-2	102162	398073	2716-2	101597	398125	B49F0029-1	97338	397388
N-20-1	101238	397925	2716-3	101597	398125	B49F0173-1	97419	398327
N-20-2	101238	397925	N-08-3	101623	397989	B49F0173-2	97419	398327
N-20-3	101238	397925	N-20-1	101238	397925	B49F0173-3	97419	398327
N-20-4	101238	397925	N-20-2	101238	397925	B49F0173-4	97419	398327
TNO-WP-1	101443	397964	N-20-3	101238	397925	B49F0240-1	97461	397582
TNO-WP-2	101443	397964	N-20-4	101238	397925	B49F0240-2	97461	397582
TNO-WP-3	101443	397964	B49F0014-1	97332	397137	B49F0240-4	97461	397582
TNO-WP-4	101443	397964	B49F0017-1	97543	397189	B49F0448-1	97341	397388
TNO-WP-5	101443	397964	B49F0026-1	97722	397242	B49F0449-1	97716	397240
B49F0014-1	97332	397137	B49F0029-1	97338	397388	B49F0449-2	97716	397240
B49F0017-1	97543	397189	B49F0173-1	97419	398327	B49F0450-1	97419	398325
B49F0026-1	97722	397242	B49F0173-2	97419	398327	B49F1471-1	97351	397477

B49F0029-1	97338	397388	B49F0173-3	97419	398327	B49F1472-1	97102	396979
B49F0173-1	97419	398327	B49F0173-4	97419	398327	B49F1484-1	97795	398910
B49F0173-2	97419	398327	B49F0240-1	97461	397582	B49F1486-1	98722	399365
B49F0173-3	97419	398327	B49F0240-2	97461	397582	B49F1487-1	99160	399400
B49F0173-4	97419	398327	B49F0240-4	97461	397582	B49F1489-1	99277	398918
B49F0240-1	97461	397582	B49F0448-1	97341	397388	B49F1490-1	99299	398045
B49F0240-2	97461	397582	B49F0449-1	97716	397240	B50A0140-1	100940	397900
B49F0240-3	97461	397582	B49F0449-2	97716	397240	B50A1170-1	101299	397569
B49F0240-4	97461	397582	B49F0450-1	97419	398325	B50A1181-1	101382	397943
B49F0448-1	97341	397388	B49F1471-1	97351	397477	B50A1185-1	100108	397048
B49F0449-1	97716	397240	B49F1472-1	97102	396979			
B49F0449-2	97716	397240	B49F1473-1	97938	397249			
B49F0450-1	97419	398325	B49F1484-1	97795	398910			
B49F1471-1	97351	397477	B49F1486-1	98722	399365			
B49F1472-1	97102	396979	B49F1487-1	99160	399400			
B49F1484-1	97795	398910	B49F1489-1	99277	398918			
B49F1486-1	98722	399365	B49F1490-1	99299	398045			
B49F1489-1	99277	398918	B49F1554-1	99256	396660			
B49F1490-1	99299	398045	B50A0140-1	100940	397900			
B50A0140-1	100940	397900	B50A1170-1	101299	397569			
B50A1170-1	101299	397569	B50A1181-1	101382	397943			
B50A1181-1	101382	397943	B50A1185-1	100108	397048			
B50A1185-1	100108	397048						

Table 9: Usable observation points of hydraulic head in 2014, 2015 and 2016.

A.3 Model Conceptualization

The model conceptualisation gives insights into the knowns and unknowns of the model. This step is conducted before the construction of the model. With the concept phase, the extent of the model is also determined. All the components and processes in and around the project location are put into place and an overview of known and more important unknown components of the system become clear.

The conceptual model is presented using two views. A top view with all the components and a section view presenting the subsurface material characteristics. Figure 32 and Figure 33 present the conceptual model. To get insights in the upper subsurface layers in the system mainly CPT data are used. Bore log data characterised the deeper layers. TNO (2017) and the archive of the municipality of Etten-Leur gave access to the subsurface data. The green brackets in Figure 32 indicate a rough estimation of the presence of the contaminants in depth. An exact location of the spread is unknown. The only facts about the contamination are a presence at the industrial side and no presence at the drinking water extractions of Seppe.

The components of the top view of the specified model are presented in Figure 33. Presented are known components consisting of the locations of the drinking water extractions, industrial extractions, rivers and a rough sketch of the land use stating indications on the recharge. The two quite uncertain components are the groundwater flow directions and the contamination plume spreading and locations. An indication is displayed, due to the available Isohypsens from the Brabant Water (2016), and contaminant bore log concentration data from Afvalzorg and Arcadis (2012). Section 5.1 gives a further elaboration on the chosen model extent.

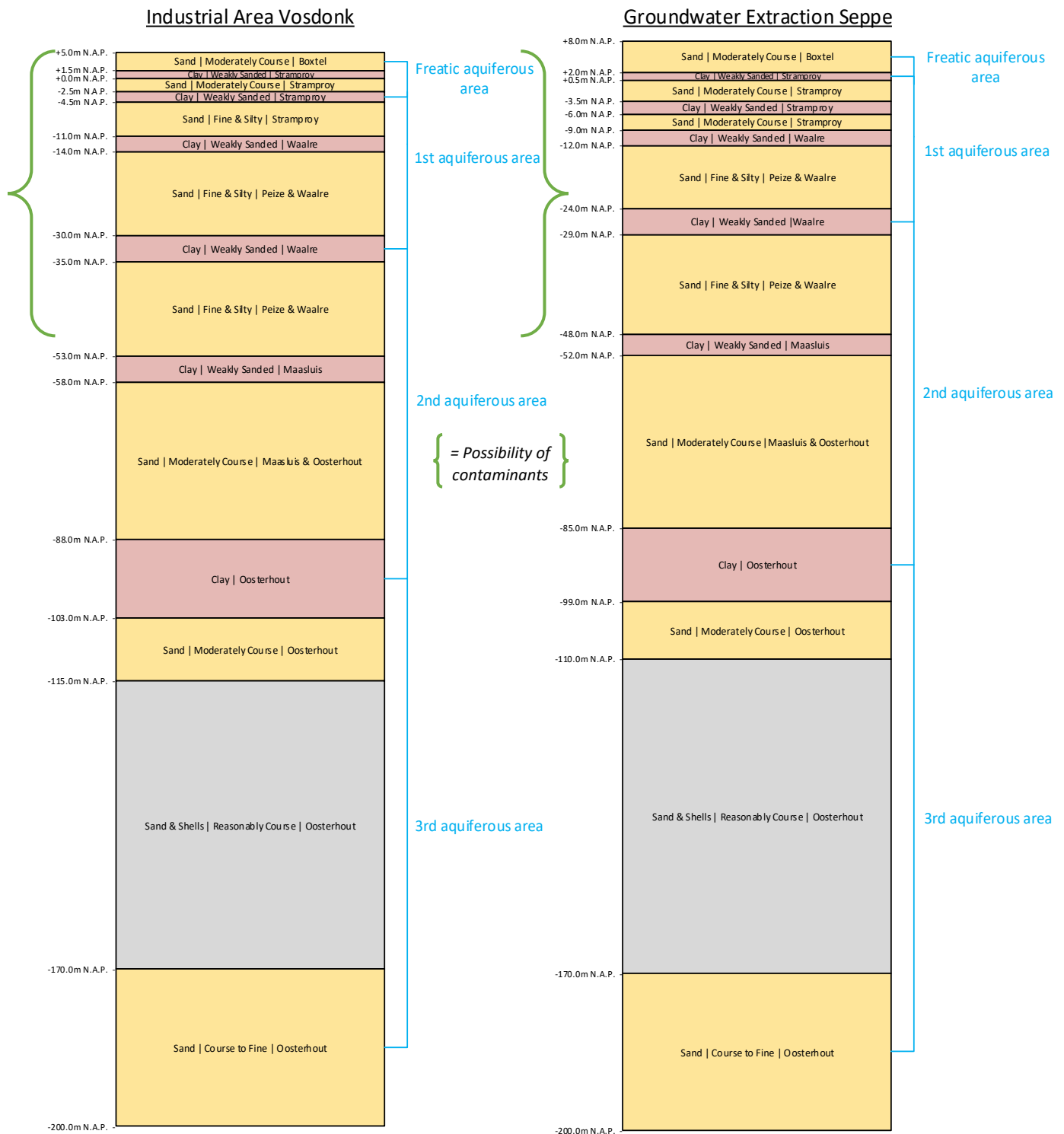


Figure 32: Subsurface material layering characteristics at the industrial area and the drinking water extractions at Seppe

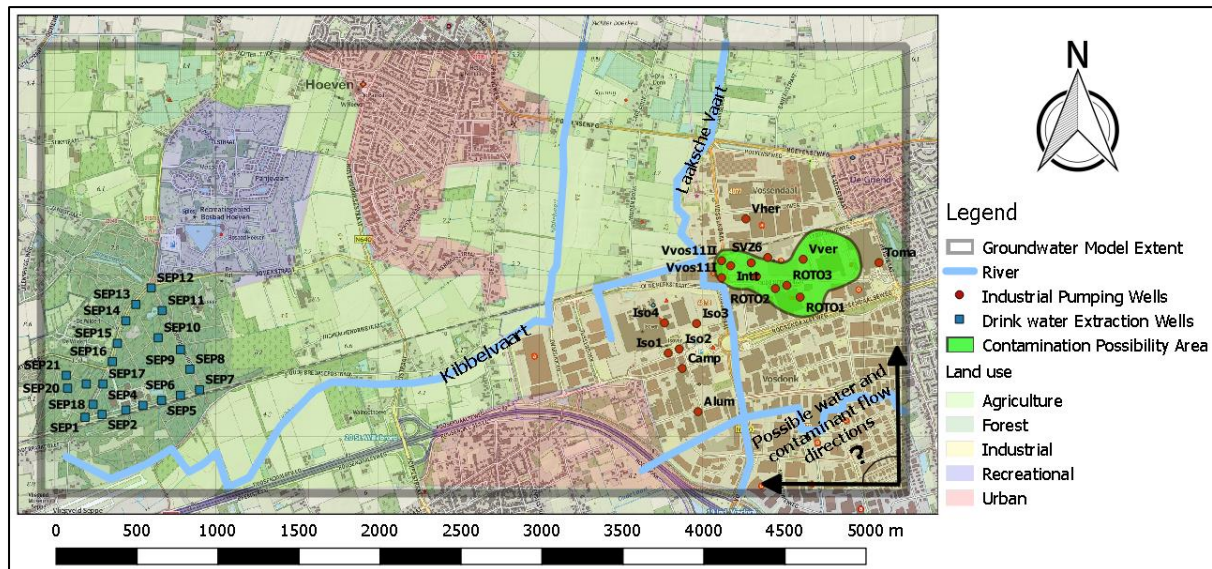


Figure 33: Conceptual top view model.

A.4 Modelling Software Selection

As explained in Chapter 1.1, the most used software to model groundwater flow and solute transport are respectively MODFLOW and the MT3D model. This research suits this software looking at comparable case studies of for example Tamma et al. (2011) and the availability of Visual MODFLOW, a package using the MODFLOW model. This package is preferred by the client Afvalzorg and is available at the company Orvion, which made it the most logical and suitable choice for creating groundwater model zero. The commercial modelling software uses the three-dimensional governing equations for groundwater flow as given in Chapter 2.1.

A.5 Model Design

The next step in the process of setting up the groundwater model consists of the model design, which focusses on the input parameters. All input including the model grid size and discretisation, layer elevations, boundary conditions, subsurface parameter data and transient extraction schedules are defined and implemented. After this, the model is ready for the calibration.

A.5.1 Model grid

To be able to create a hydrological model the scope and grid are specified. The conceptual model determined the first indication of the dimensions of the model. This consists of dimensions of 5340 by 2760 by 200 meters. In the conceptual model of Figure 33, the border of the model extent is displayed. The left boundary of the model is located close to the left of the drinking water extractions of Seppe, which is acceptable as the main focus of the groundwater model is around the industrial area. The right border is also chosen close to the last industrial extraction well TOMA. This extraction well has not been active from 1978 and consisted of a small discharge. There are also clear indications, gathered from the conceptual phase, that the groundwater flow has a west to north direction of flow throughout the extent. This means the right border of the model extent should not create problems for current and future modelling. The north and south border have a decent distance to the industrial area and Seppe extractions to prevent boundary problems. With these choices for the model area, the size of the model is as small as possible. This is favourable for the time duration of the simulations.

The discretisation of the model is a very important part as this determines how heavy the calculations get. The vertical layering for the groundwater model zero was already gathered from Figure 32. A 20-meter discretisation is applied to the X- and Y-direction, which means the layers have a 20 by 20-meter top view discretisation of cells. This is the most detailed possibility considering the limitation in Visual Modflow for the number of rows and columns.

A.5.2 Boundary conditions

Three types of boundary conditions are implemented in the model. Constant head, river and recharge boundary conditions. The constant head boundary conditions are used at the edges of the model, the river boundary conditions implement the Laaksche Vaart and Kibbelvaart and the recharge boundary condition specifies the net inflow at the top layer of the model.

Hydraulic head specifications of the Brabant model specify the boundaries at the edge of the model (Brabant Water, 2016). Using the values from different isohypse maps at specific depths, related to N.A.P. and located at the boundary of the model, quantification was easily possible. Some locations needed fine tuning, but no calibration on this area was necessary.

Waterschap Brabantse Delta delivered the river data for the model area. The influencers turned out to be, as expected, the Laaksche Vaart and Kibbelvaart. The exact locations and corresponding properties were delivered. The information consists of the dimensions of the river, the water level at multiple places, estimated model conductivity values below the river and the elevation of the bottom of the rivers. In Figure 34 and Table 10 an overview is given of the implemented parameters including the locations. In between the implemented data points, it is assumed that depths, water levels and dimension decrease or increase linearly. The Laaksche Vaart consists of small spillways, which explains the sudden jump between some points at the locations of the branches. Conductivity values are calculated by the Visual Modflow software using the implemented parameter values. In Figure 34 number 1 to 4 represent the Kibbelvaart and number 5 to 11 the Laaksche Vaart including some important branches.

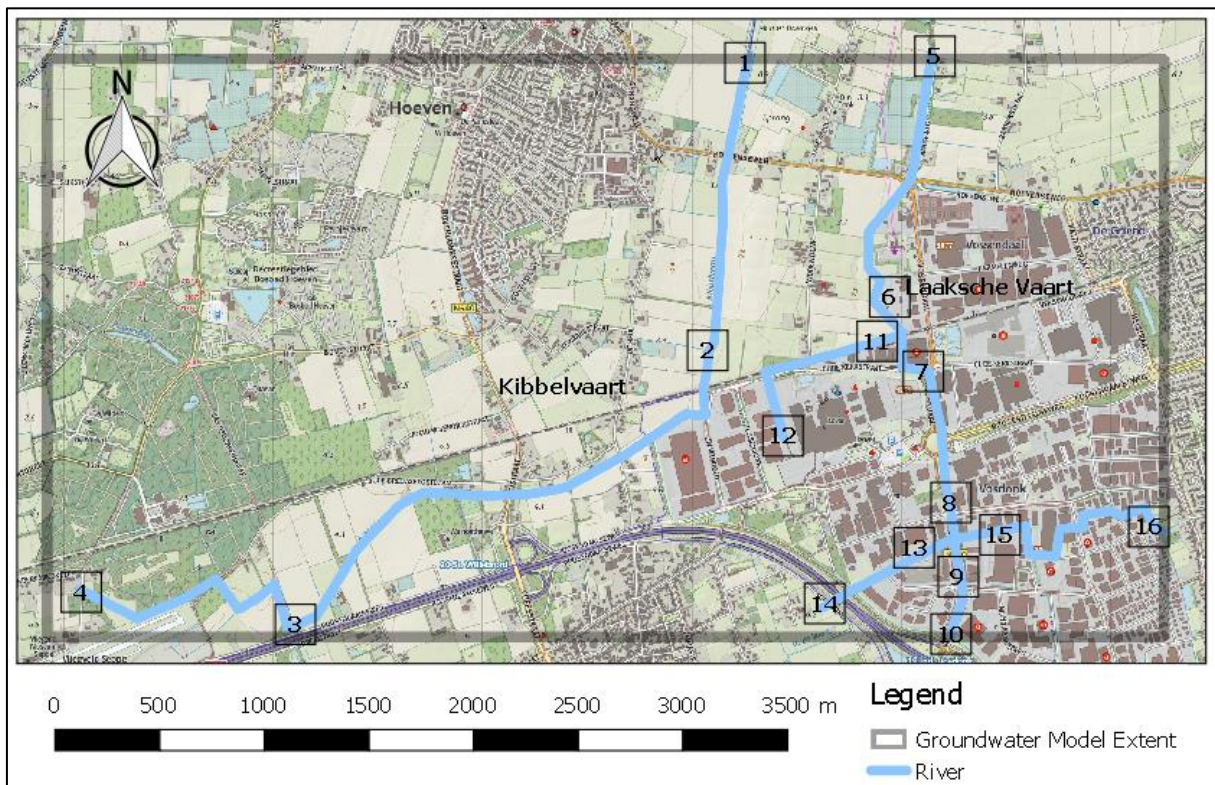


Figure 34: River data point locations for implementation in Visual Modflow.

Data Number	River Stage (m N.A.P.)	River Bottom (m N.A.P.)	River bottom thickness (m)	K _z River Bottom (m/d)	River Width (m)
1	0.15	-0.5	0.1	0.1	2.5
2	0.92	0.1	0.1	0.1	2.6
3	2.35	2.1	0.05	0.1	1.0
4	7.4	7.26	0.05	0.1	0.5
5	0.45	0.05	0.1	0.1	2.5
6	1.2	0.7	0.1	0.1	2.5
7	1.85	1.27	0.1	0.1	2.0
8	2.9	2.35	0.1	0.1	1.7
9	2.7	2.28	0.1	0.1	1.7
10	4	3.03	0.1	0.1	1.7
11	1.85	1.27	0.1	0.1	0.6
12	2.6	2.25	0.1	0.1	0.6
13	2.7	2.28	0.1	0.1	1.0
14	4.2	4.05	0.05	0.1	1.0
15	2.7	2.3	0.1	0.1	1.5
16	4.0	3.7	0.1	0.1	1.5

Table 10: Parameter properties of the river boundary condition.

The recharge boundary conditions applied to the top layer of the groundwater model contains multiple polygons with assigned quantities. Inside this boundary condition, the precipitation surplus is implemented, which means this condition already includes the evaporation. Brabant Water (2016) was able to deliver areas of 200 by 200 meters with the average precipitation surplus in the model area. A first estimate of the values was made using this data. An overview of the classification of the polygons is presented in Figure 35. Each of these classes has an individual value for the precipitation surplus. The final values for each class are shown in Paragraph 6 in Table 15, because of the necessity for some calibration in these values to model the groundwater flow in the first couple of layers correct.

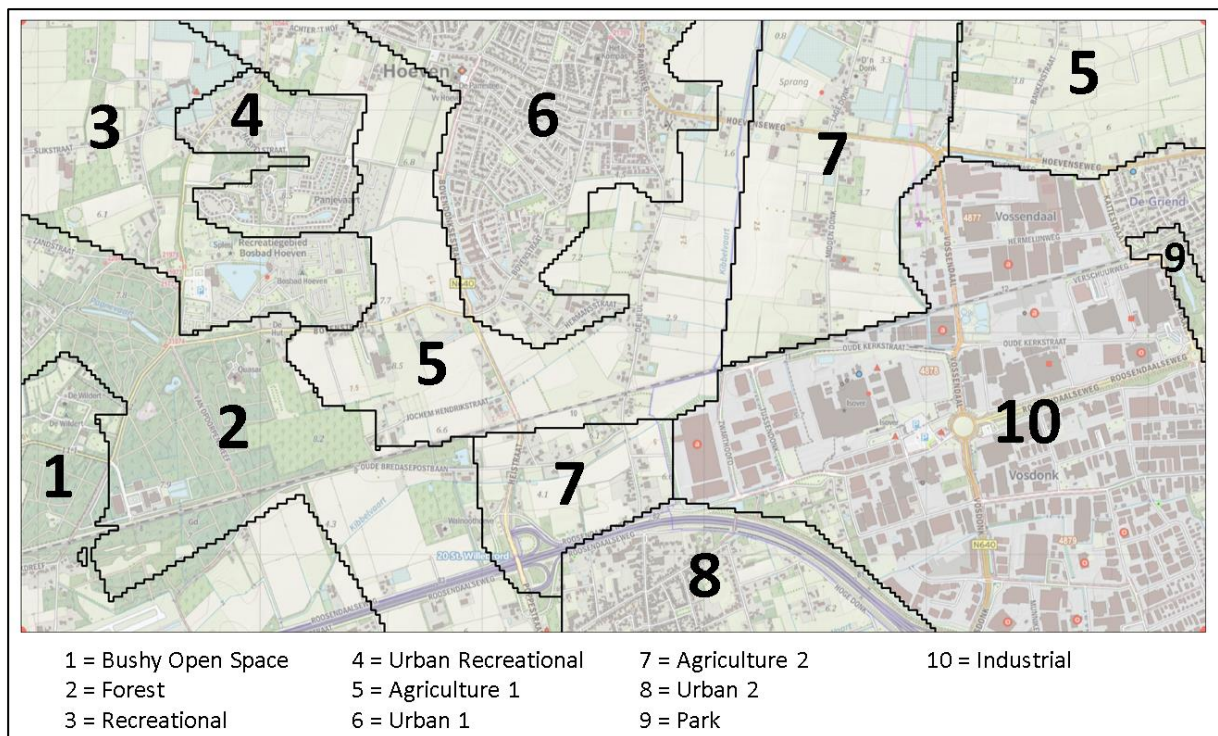


Figure 35: Recharge boundary zones with classification.

A.5.3 Subsurface parameters

Literature delivered the initial subsurface parameters for the hydraulic conductivity and porosity. The conceptual model identified the formation of each layer. Layer formation knowledge is especially gathered using the REGIS II model from TNO (2017). The storage coefficient, S_s , and specific yield, S_y , are kept constant for the standard values of Visual Modflow. The values are $S_s = 1E-5 \text{ m}^{-1}$ and $S_y = 0.2$. These average values are accurate enough looking at the goals and scope of further research with the model. If necessary, it is possible to decide to implement them in further research. Table 11 gives the vertical and horizontal hydraulic conductivity, porosity and effective porosity values for each formation. These values are implemented in the model and are considered the initial parameter values before the start of the calibration. The quantification of the porosity and effective porosity is based on Yu, Kamboj, Wang, and Cheng (2015, p. 32).

It is important to mention the project location of the sources differs from the project location of the research. The values from the sources can differ at Etten-Leur. The literature study was conducted to get global insights in the properties of the formations in the model area. In the calibration, no strict rules to keep within a close range of this values is applied. Changes are mainly verified by the gathered hydraulic head data as presented in Table 9.

Layer	K_z	K_{xy}	Por.	Eff. Por.	Source (K_z and K_{xy})
<i>Formation of Oosterhout (Clay)</i>	0.007	0.07	0.45	0.10	(de Bruijn, 2012, pp. 3-5)
<i>Formation of Oosterhout (Sand)</i>	6	15	0.40	0.30	(Berendsen, 2005, p. 132) (Arcadis, 2014, p. 13) (Grontmij, 2009, p. 6)
<i>Formation of Oosterhout (Shell)</i>	10	30	0.40	0.35	(Bot, 2011)
<i>Formation of Maasluis (Clay)</i>	0.002	0.02	0.45	0.10	(de Bruijn, 2012, pp. 3-5)
<i>Formation of Maasluis (Sand)</i>	3	6	0.40	0.30	(Berendsen, 2005, p. 132) (Grontmij, 2009, p. 6)
<i>Formation of Peize and Waalre (Sand)</i>	5	25	0.40	0.30	(Duineveld, 2013, p. 5)
<i>Formation of Waalre (Clay)</i>	0.0055	0.055	0.45	0.10	(de Bruijn, 2012, pp. 3-5)
<i>Formation of Boxtel (Sand)</i>	2	5.5	0.40	0.30	(Grontmij, 2009, p. 6)
<i>Formation of Stramproy (Sand)</i>	5	13	0.40	0.30	(Arcadis, 2014, p. 30) Layers deeper situated, so lower values to be indicated.
<i>Formation of Stramproy (Clay)</i>	0.006	0.06	0.45	0.10	(de Bruijn, 2012, pp. 3-5)

Table 11: Subsurface parameter values of the present formations in the model.

The groundwater model zero consists of 15 layers. In Figure 36 and Figure 37 section views are presented on the layering of the system. The colouring indicates the classes of parameter values. This layering is based on Figure 32, as was mentioned previously. The corresponding initial values for each layer are given in Table 12.

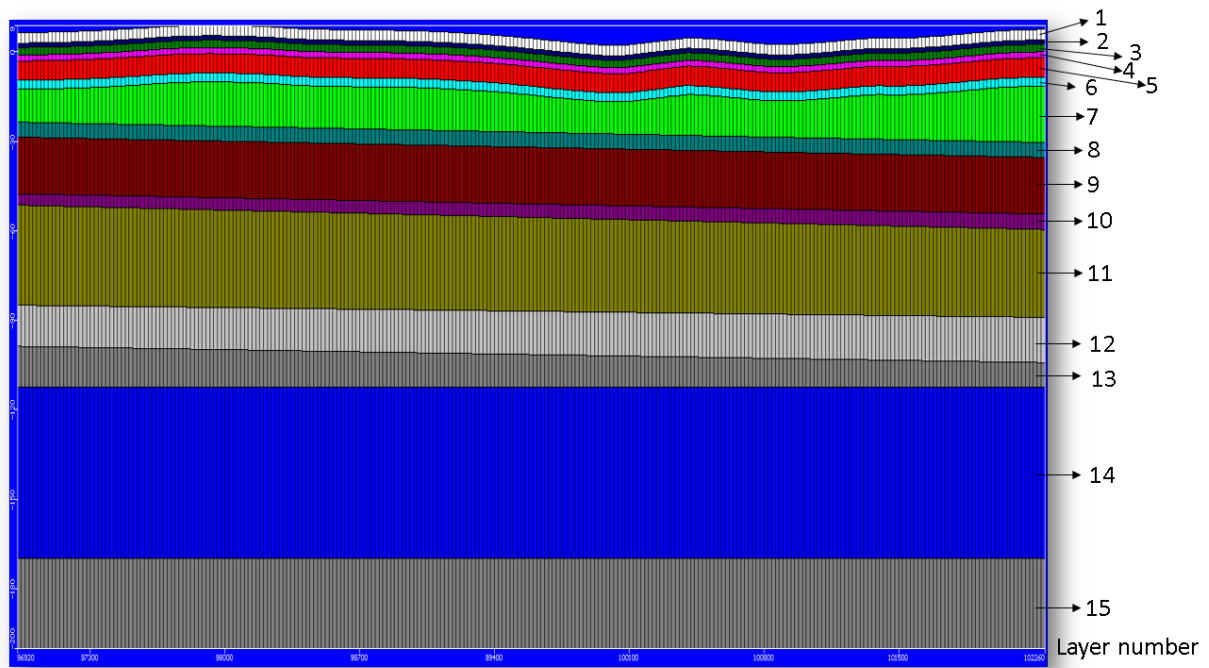


Figure 36: Section view with class colouring of the hydraulic conductivities.

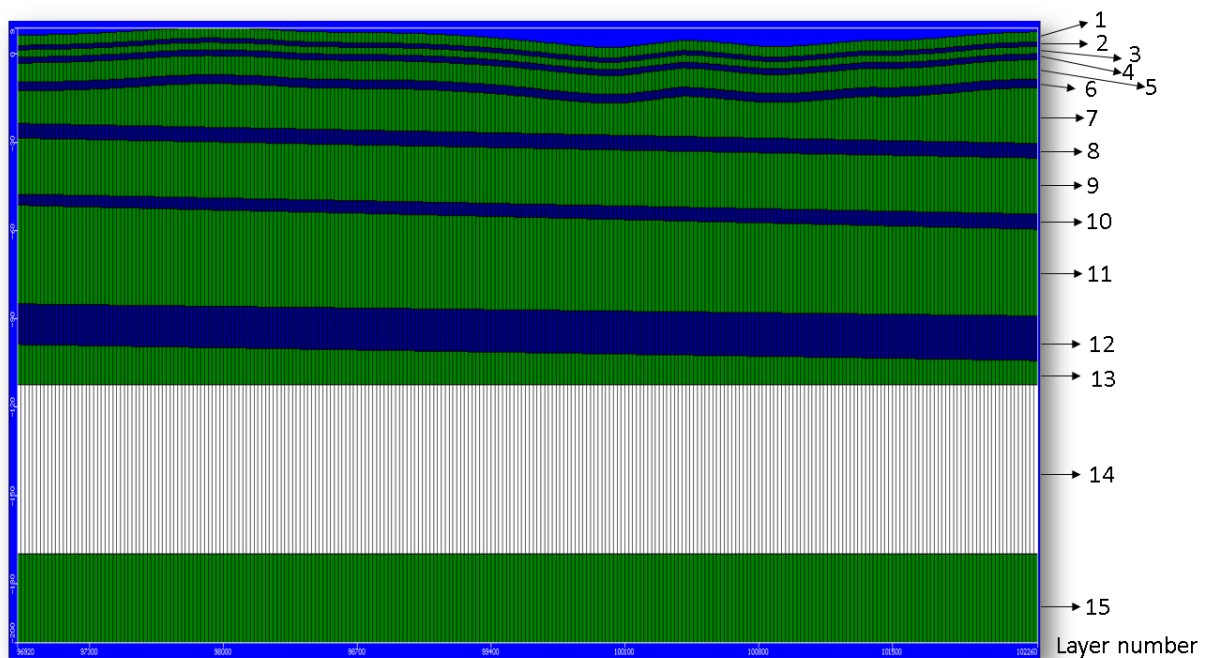


Figure 37: Section view with class colouring of the Porosity and Effective Porosity.

Layer	K _z	K _{xy}	Por.	EffP.	Layer	K _z	K _{xy}	Por.	EffP.
1	2	5.5	0.40	0.30	9	5	25	0.40	0.30
2	0.006	0.06	0.45	0.10	10	0.002	0.02	0.45	0.10
3	5	13	0.40	0.30	11	3	6	0.40	0.30
4	0.006	0.06	0.45	0.10	12	0.007	0.07	0.45	0.10
5	5	13	0.40	0.30	13	6	15	0.40	0.30
6	0.0055	0.055	0.45	0.10	14	10	30	0.40	0.35
7	5	25	0.40	0.30	15	6	15	0.40	0.30
8	0.0055	0.055	0.45	0.10					

Table 12: Initial subsurface parameter values.

A.5.4 Ground and layering height levels

The implementation of the layer height of the models' layers is done using the subsurface levels from the conceptual model. The two locations presented in Figure 32 form the basis for the layer heights. In the deeper layers, most differences in depth are found over the x-direction. Layer 8, 10 and 12, as presented in Figure 36 and Figure 37, have a slight depth movement over the horizontal distance. The ground level behaviour forms the basis for the first six layers. To keep a nice and even thickness the layer heights follow the height level differences from the top surface data.

The ground level behaviour is based on the online data source of AHN (2017). The data map of AHN2 for the model extent is given in Figure 38. Over the entire model area, points with ground level data related to the N.A.P. level have been collected. It was important to collect data points of the locations, without buildings or trees. These are not filtered out from this data source. Making that mistake could give inaccurate ground level values. The Visual Modflow software contains the import function, which made it possible to import each data point and perform an interpolation over these values. The simple kriging function from Visual Modflow was chosen to conduct this interpolation. This behaviour of movement in vertical direction could easily be transferred to the layers below, creating the nice even layers presented in Figure 36 and Figure 37



Figure 38: AHN ground level data map (AHN, 2017).

A.5.5 Extraction well's transient schedules

Afvalzorg and Brabant Water were able to deliver respectively the industrial and drinking water extraction schedules from 1976 until 2016 with intervals of one year. This means a transient system is set up for the groundwater model zero using these extraction schedules as a guideline. An extra transient step of 1 year is added before the start of 1976, which does not include any extractions. If needed, this can be used as a baseline situation. Not every industrial extraction has been active over the specified full time. Figure 39b and Table 13 give an overview of the activity. This presents insights on the behaviour of the industrial extraction. All individual drinking water wells have been active in every year specified. They all consist of equal capacity. Every single drinking water well has the same behaviour as presented in the graph of Figure 39a, which illustrated drinking water extraction well SEP15 as an example. In Figure 33 the locations of all the wells are presented.

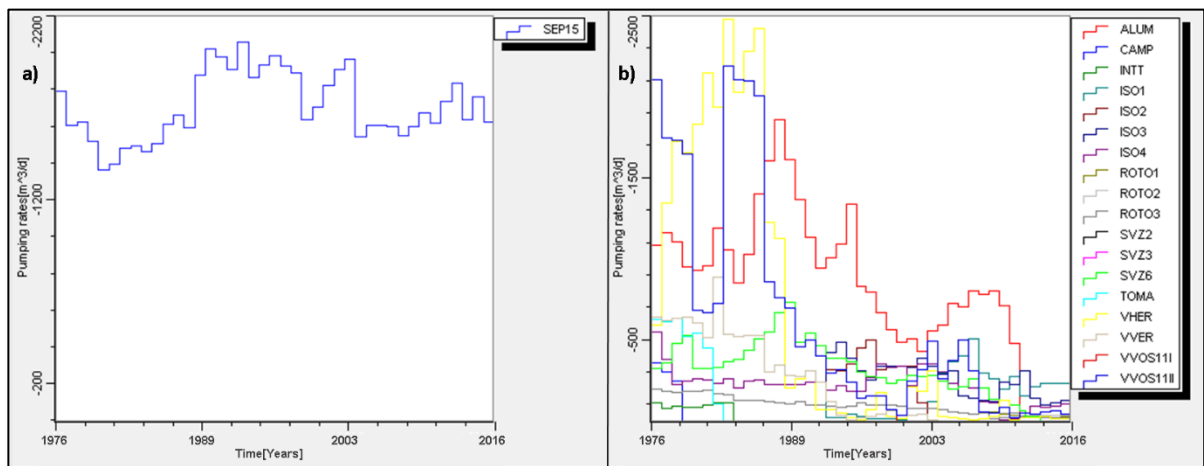


Figure 39: Drink water and Industry extraction well schedules.

Well	Activity	Well	Activity
ALUM	1976 - 2011	ROTO3	1976 - 2016
CAMP	1976 - 1978	SVZ2	1976 - 2012.5
INTT	1976 - 1983	SVZ3	1976 - 2012.5
ISO1	1976 - 2000, 2003 - 2016	SVZ6	1976 - 2012.5
ISO2	1976 - 2002	TOMA	1976 - 1982
ISO3	1976 - 2016	VHER	1976 - 2016
ISO4	1976 - 2016	VVER	1976 - 2003
ROTO1	1976 - 2016	VVOS11I	1976 - 1999
ROTO2	1976 - 2016	VVOS11II	1976 - 2016

Table 13: Active years of the industrial extraction wells.

A.6 Model Calibration

With the finished model design, calibration of the model is necessary to construct a match between model and field conditions. The calibration of the model is conducted using mainly the hydraulic conductivity parameters. For the top layers, calibration with the recharge boundary condition was necessary. Calibration is performed using the hydraulic heads of 2016. This dataset is presented in Table 9. The optimal fit between the calculations of the model and the field data are gathered using the calibration graph in Visual Modflow. Figure 40 presents the results of the calibration.

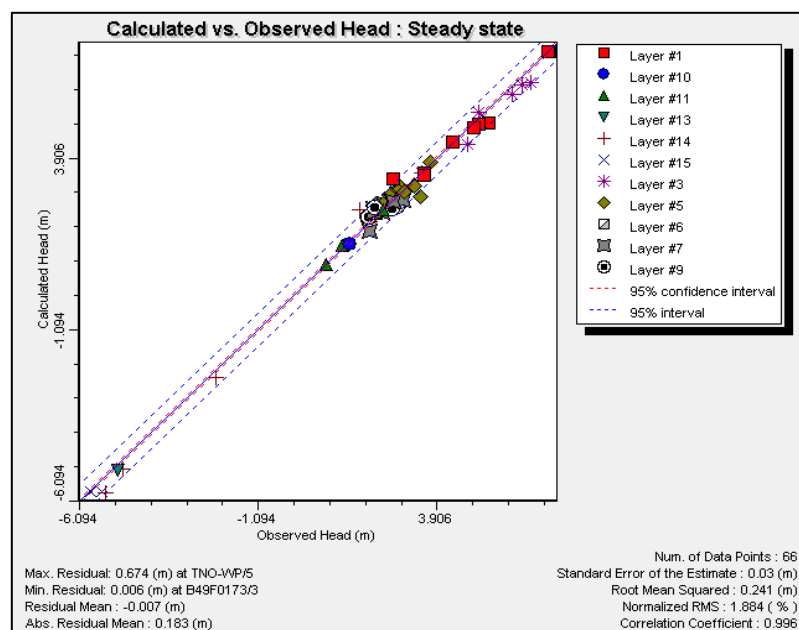


Figure 40: Calibration results for groundwater model zero.

The calibration shows a nice fit using all 66 hydraulic head data points, which reaches a root mean square error (RMS) of 1.884%. Due to the availability of a few data points over a model with a large area this percentage needs to be as small as possible and certainly below 5%.

To accomplish this calibration, many changes had to be made in the calibration parameter values. Table 14 and Table 15 present the parameter quantification corresponding to the calibrated model. During the calibration, the vertical hydraulic conductivity influenced the model output the most. The horizontal conductivity was a very difficult parameter creating limited changes to model output. This made it a dangerous parameter to conduct calibration with, but to reach this accuracy the variations in the horizontal hydraulic conductivity were needed. At last, the recharge values affected the model output especially in layer 1 to layer 3. The hydraulic conductivity parameters were unable to compensate the negative differences between model output and measurement data in these top layers. This meant more recharge in the top layers was needed to compensate this negative difference.

Layer	K_{Z,Initial}	K_{XY,Initial}	K_{Z,Calibr.}	K_{XY,Calibr.}	Layer	K_{Z,Initial}	K_{XY,Initial}	K_{Z,Calibr.}	K_{XY,Calibr.}
1	2	5.5	1	5	9	5	25	2	10
2	0.006	0.06	0.001	0.01	10	0.002	0.02	0.009	0.09
3	5	13	1	5	11	3	6	3	15
4	0.006	0.06	0.0005	0.005	12	0.007	0.07	0.005	0.05
5	5	13	3	10	13	6	15	3	6
6	0.0055	0.055	0.0008	0.008	14	10	30	8	17
7	5	25	3	12	15	6	15	3	6
8	0.0055	0.055	0.002	0.02					

Table 14: Subsurface parameter values after model calibration.

Recharge Class	Recharge (mm/year)	Recharge Class	Recharge (mm/year)
Bushy Open Space (1)	125	Urban 1 (6)	170
Forest (2)	300	Agriculture 2 (7)	75
Recreational (3)	250	Urban 2 (8)	120
Urban Recreational (4)	225	Park (9)	325
Agriculture 1 (5)	175	Industrial (10)	70

Table 15: Recharge class values after model calibration. Class locations presented in Figure 35.

A.7 Model Verification and future monitoring

The final step is the model verification. This consists of the calibrated model using hydraulic head field data from previous years. A comparison of this field data is made using the model input from the calibrated model. The validation is conducted using the hydraulic head data sets of 2014 and 2015 presented in Table 9. These years are chosen because they are the most complete datasets from older years. The results of the verification are given in Figure 41.

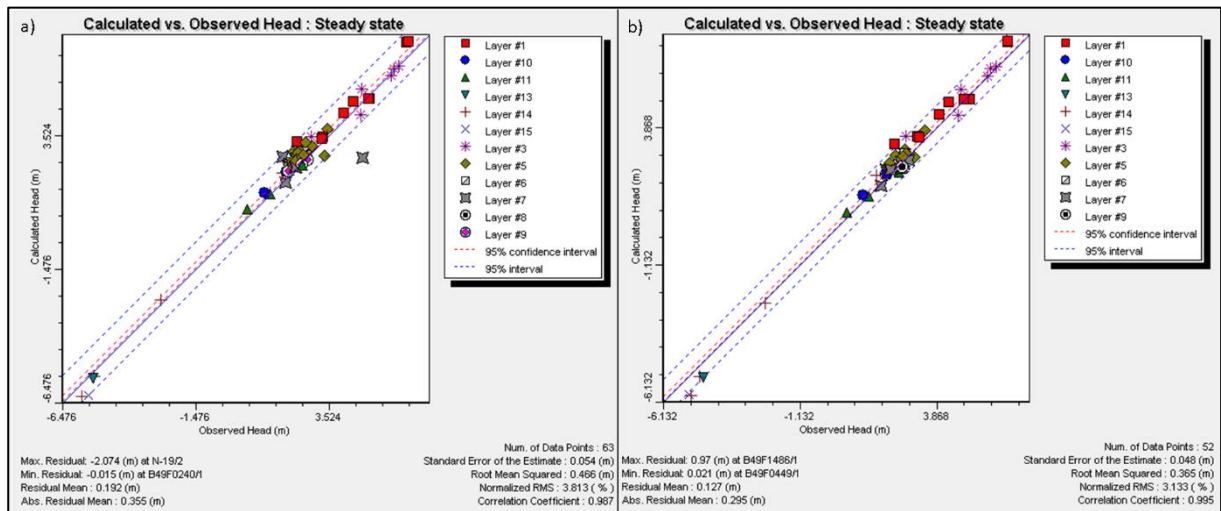


Figure 41: Model validation results. With a) for the year 2015 and b) for the year 2014.

The verification is less accurate, but still comfortably within the 5% root mean square error. This indicates a successful verification. Figure 41 presents a large outlier in the validation of 2015. The location of this outlier is presented in Figure 42. This hydraulic head field data point is located close to the boundary, which could have caused this difference. The presence of the park and some surface water near to the data point could also have resulted in a mistake or invalid measurement. Without the outlier, the validation result of 2015 improves with another 0.3%. For the outlier, indications are available that it is caused by data collection effects or by model boundary effects.

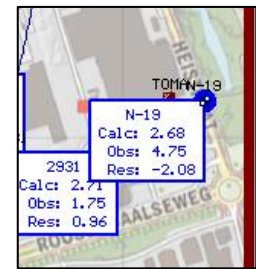


Figure 42: Validation 2015 outlier.

The final step consists of hydraulic head monitoring. Over the coming years, changes at the industrial site are collected in the form of data and can be compared to the model output. As explained in Chapter 1.1 and by Kumar (2012), errors in the predictive model, even though small, can result in gross errors in solutions projected forwarded in time. A constant comparison of future field conditions with the model predictions is achieved, by performing monitoring and validation during the upcoming years.

A.8 Groundwater model zero resulting layer overview

The finished model can do the predictive simulation. Different scenarios can be created and the output can be compared. Having performed all the build up steps, the groundwater model zero is ready and accepted for the research and implementations of respectively the 1D solute transport and kriging methodology. Figure 43 to Figure 57 presents an overview of all the groundwater layers with their hydraulic head in the year 2016 to give insights in the most recent groundwater flow situation.



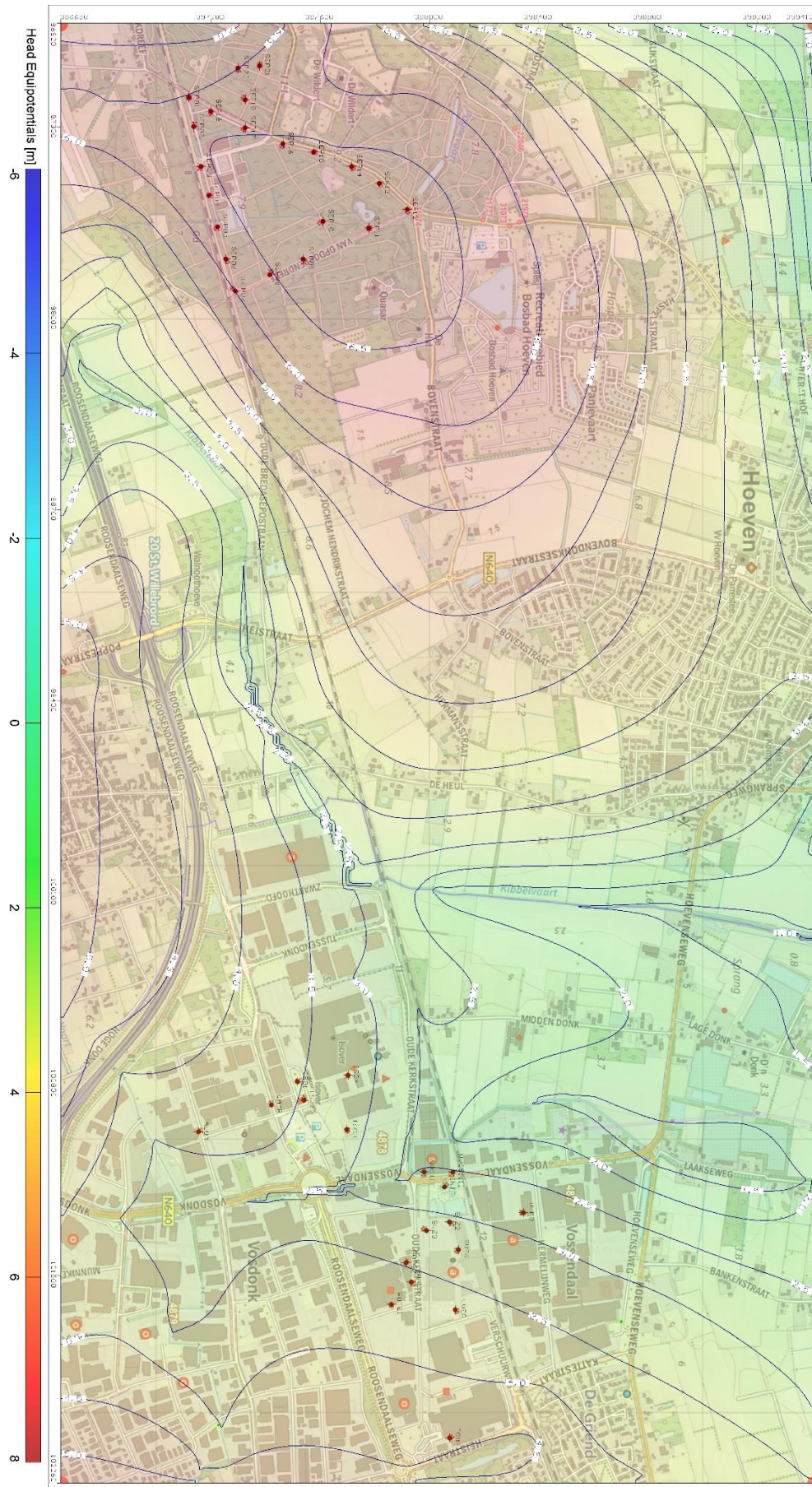
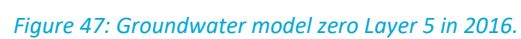
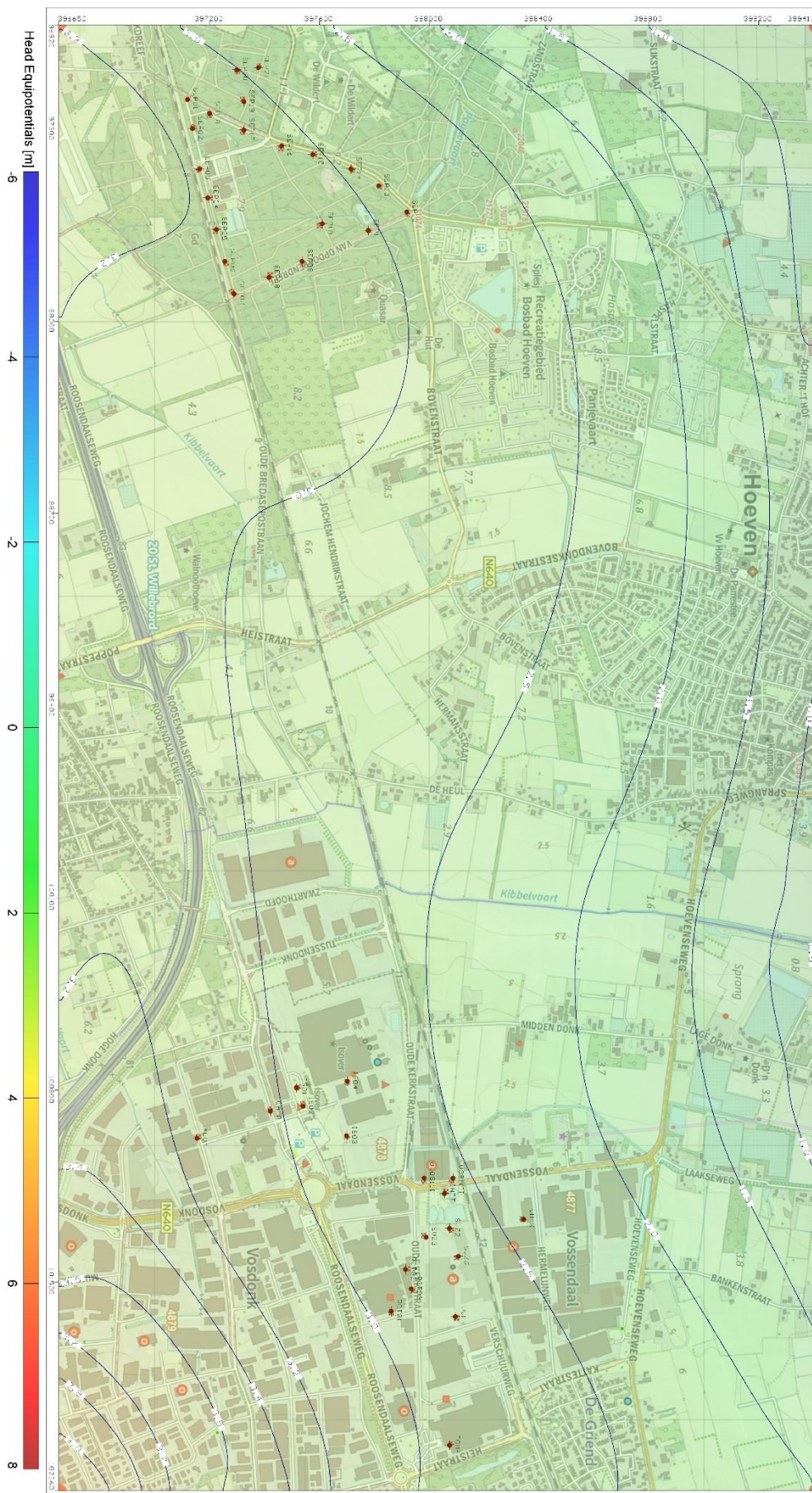


Figure 44: Groundwater model zero Layer 2 in 2016.

Figure 45: Groundwater model zero Layer 3 in 2016.





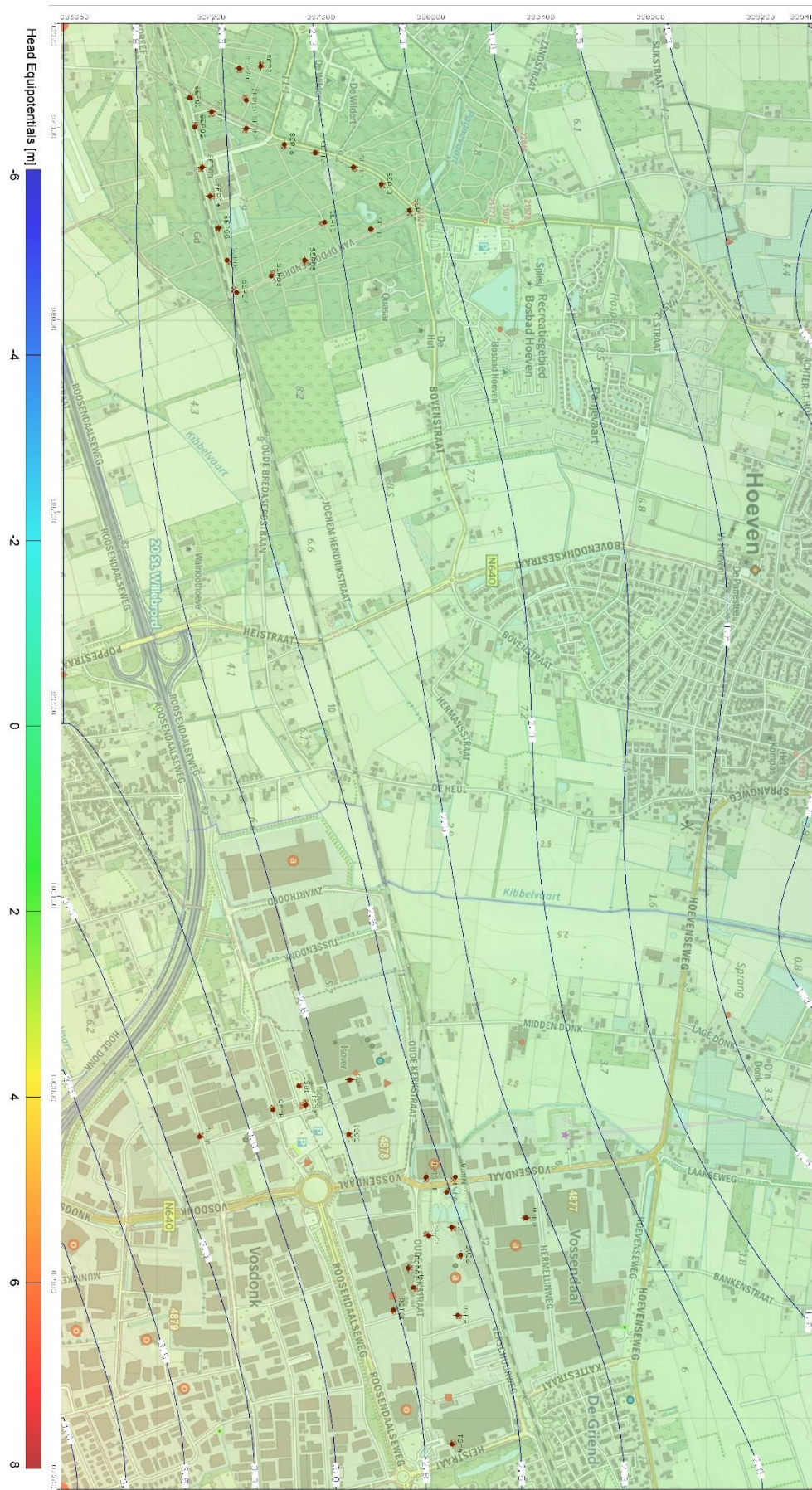


Figure 49: Groundwater model zero Layer 7 in 2016.

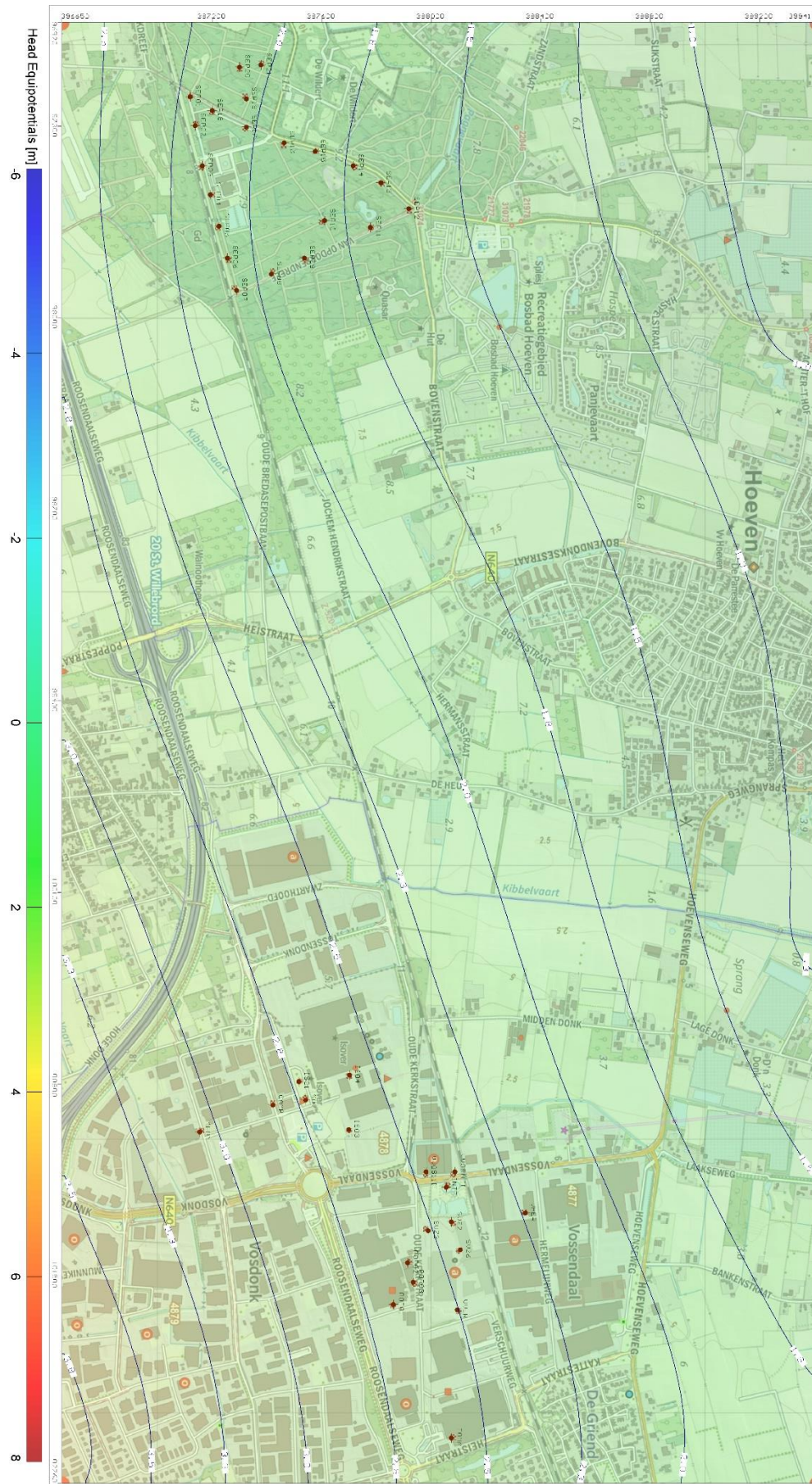


Figure 50: Groundwater model zero Layer 8 in 2016.

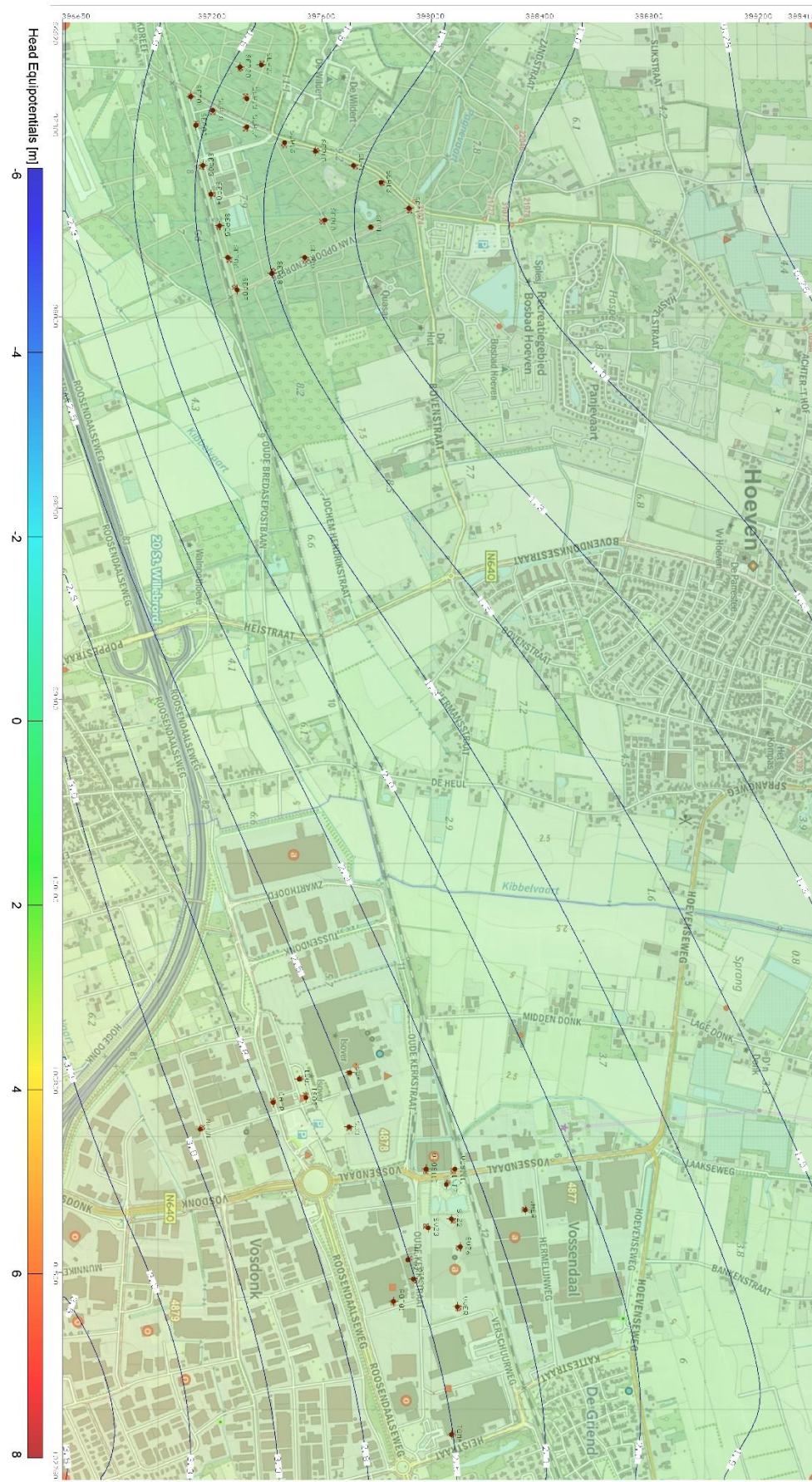


Figure 51: Groundwater model zero Layer 9 in 2016.

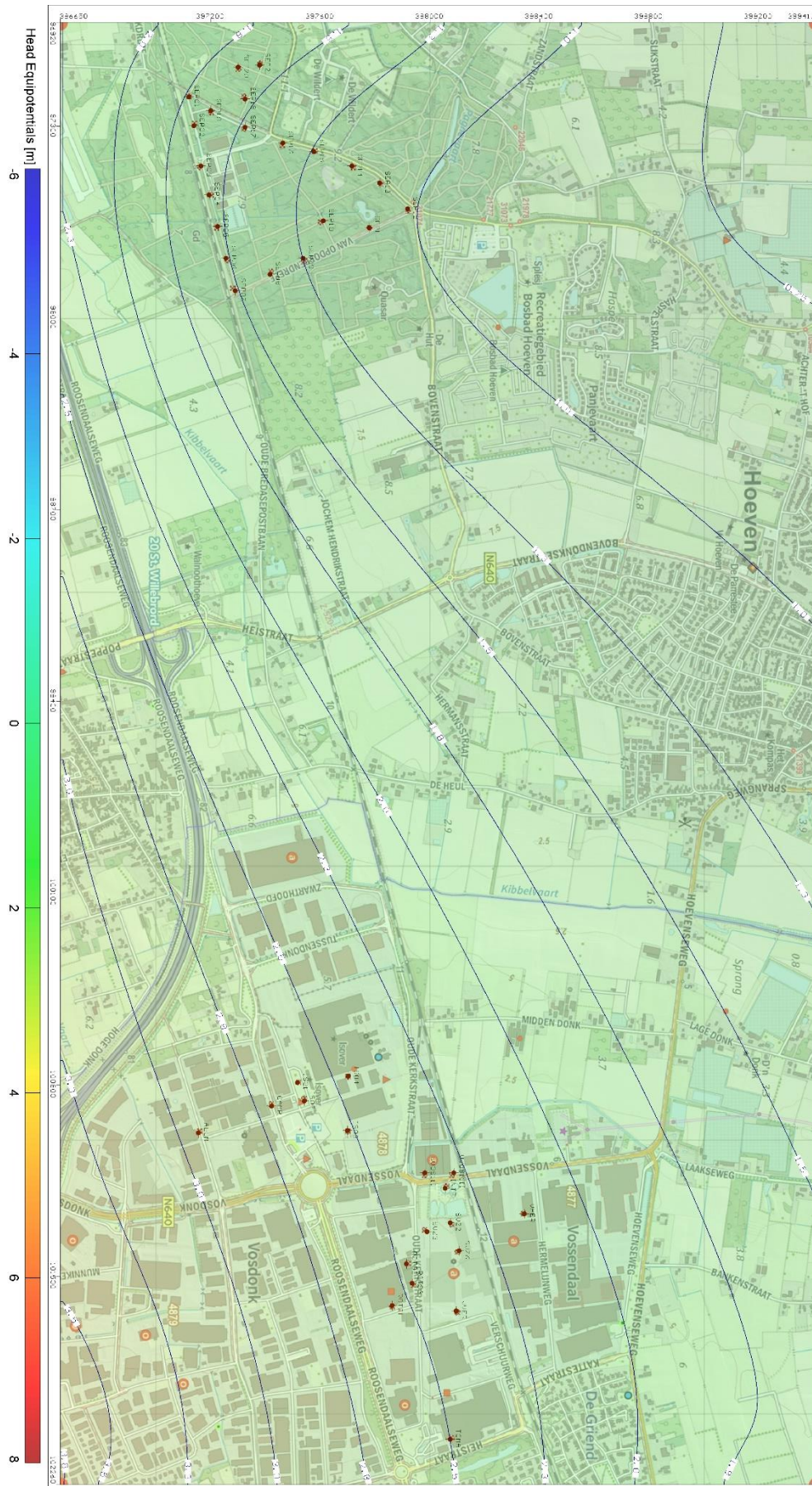


Figure 52: Groundwater model zero Layer 10 in 2016.

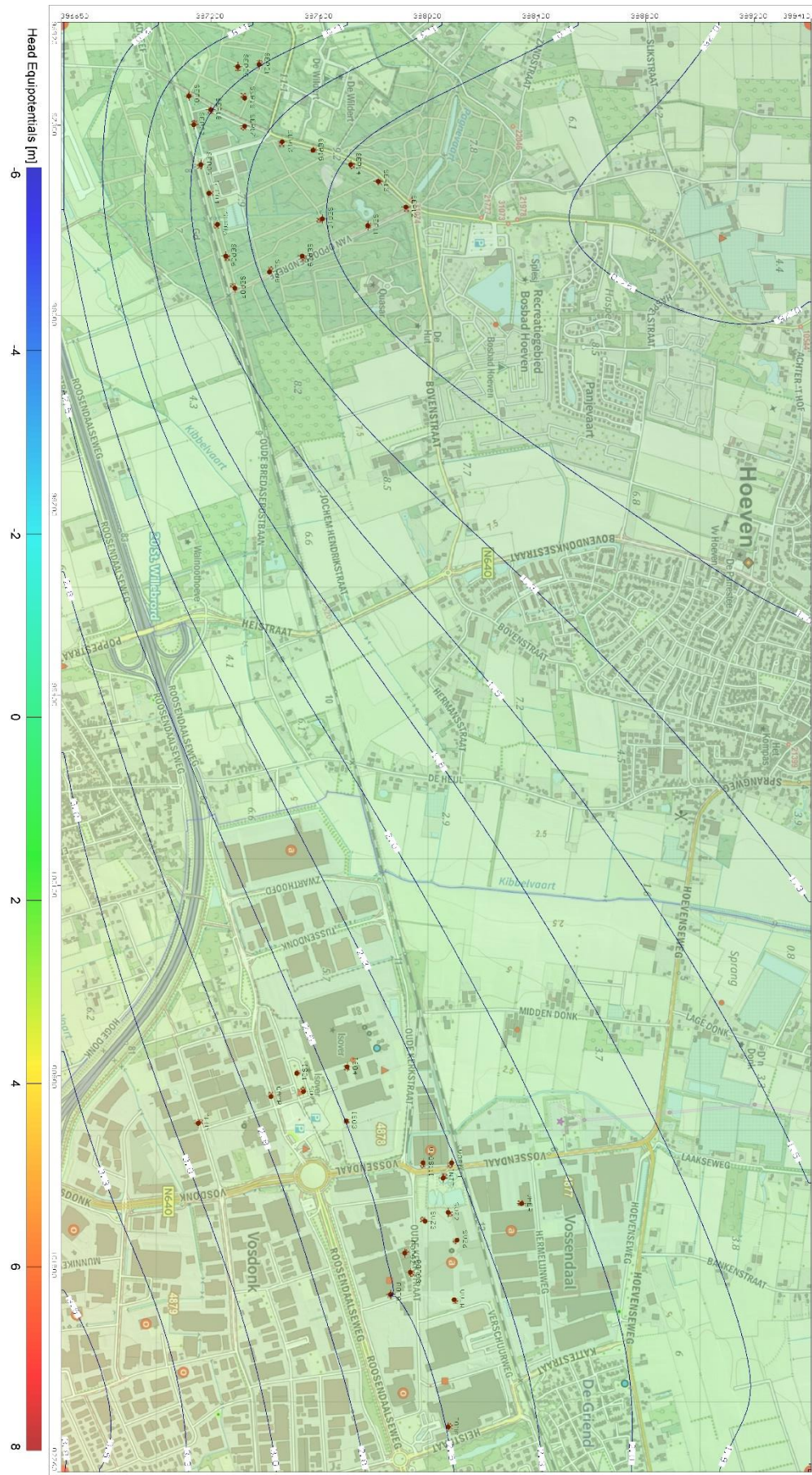


Figure 53: Groundwater model zero Layer 11 in 2016.





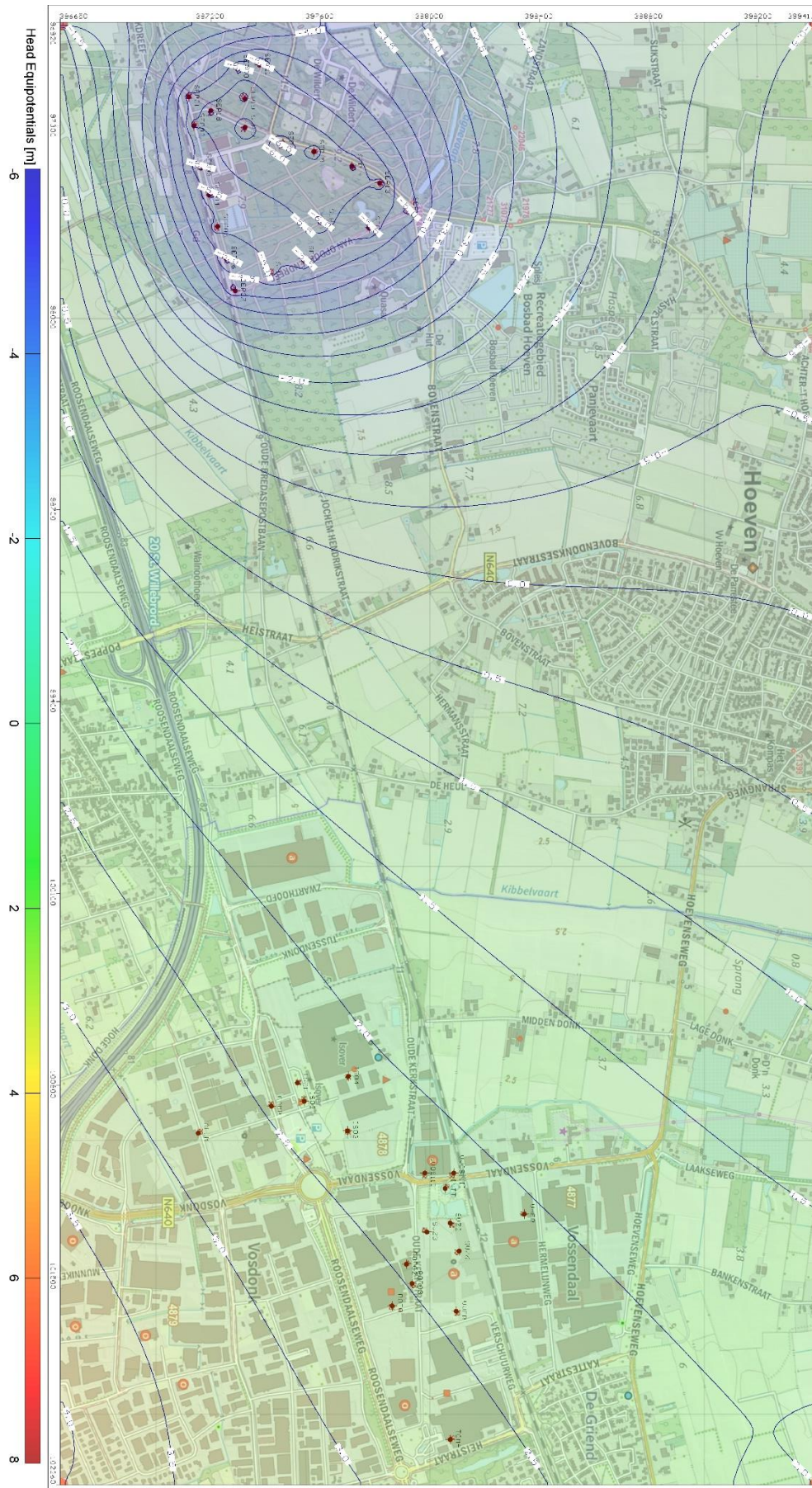


Figure 56: Groundwater model zero Layer 14 in 2016.



Appendix B - Box model alternatives

Alternative	1	2	3	4	5
Short sentence	3SMd2 3SiS1.1 2CSi0.9 2SiC0.6 1C0.4	2SMd2 1CSi0.5 1C2.5	1SMd2 1SiS2.5 1SiC0.5	1SMd1 1SiS0.5 1SiC3.5	1SMd1.2 2SiS0.9 1CSi0.7 1SiC0.5 2C1.1
Layer 1	SMd	SMd	SMd	SMd	CSi
Thickness 1	0.9	0.9	2	1	0.7
Layer 2	CSi	CSi	SiC	SSi	SMd
Thickness 2	0.7	0.5	0.5	0.5	1.2
Layer 3	SiS	C	SiS	SiC	C
Thickness 3	0.3	2.5	2.5	3.5	1.3
Layer 4	SiC	SMd			SiS
Thickness 4	0.3	1.1			0.5
Layer 5	SMd				SiC
Thickness 5	0.7				0.5
Layer 6	C				SiS
Thickness 6	0.4				0.4
Layer 7	SiS				C
Thickness 7	0.4				0.4
Layer 8	SiC				
Thickness 8	0.3				
Layer 9	SiS				
Thickness 9	0.4				
Layer 10	CSi				
Thickness 10	0.2				
Layer 11	SMd				
Thickness 11	0.4				
Total Thickness	5	5	5	5	5
Average Kz	0.116	0.026	0.959	0.152	0.035
Average Kx/Ky	14.921	8.392	21.580	4.933	8.197
Average Eff. Por.	0.237	0.190	0.260	0.185	0.194
Average Por.	0.419	0.430	0.405	0.440	0.429

Table 16: Box model alternative 1 to 5.

Alternative	6	7	8	9	10
Short sentence	1SCr0.8 1SMd2 1SiS0.3 1SiS0.8 1SiC0.5 1C0.9	2SCr1.2 2SMd0.9 1SiS0.5 1SiS0.2 2CSi0.7 1C1.5	1SCr3 1SiC0.5 1C1.5	1SCr0.8 2SMd2.5 3SiS1 1SiC0.5 1C0.2	1SMd0.5 4SiS1.5 2SiS0.5 1CSi0.2 3SiC1.5 1C0.8
Layer 1	SMd	SiS	SiC	C	SMd
Thickness 1	2	0.5	0.5	0.2	0.5
Layer 2	SiS	C	SCr	SiS	SSi
Thickness 2	0.3	1.5	3	0.4	0.5
Layer 3	SiC	SCr	C	SiC	SiS
Thickness 3	0.5	0.6	1.5	0.5	0.4
Layer 4	SCr	SSi		SMd	SiC
Thickness 4	0.8	0.2		1	0.3
Layer 5	SSi	SMd		SiS	CSi
Thickness 5	0.5	0.4		0.4	0.2
Layer 6	C	CSi		SMd	SiC
Thickness 6	0.9	0.4		1.5	0.3
Layer 7		SMd		SiS	SiS
Thickness 7		0.5		0.2	0.4
Layer 8		CSi		SCr	SiC
Thickness 8		0.3		0.8	0.9
Layer 9		SCr			SiS
Thickness 9		0.6			0.2
Layer 10					C
Thickness 10					0.8
Layer 11					SiS
Thickness 11					0.5
Total Thickness	5	5	5	5	5
Average Kz	0.070	0.041	0.041	0.235	0.059
Average Kx/Ky	17.045	13.519	18.109	24.302	7.614
Average Eff. Por.	0.236	0.217	0.225	0.267	0.194
Average Por.	0.419	0.424	0.415	0.407	0.430

Table 17: Box model alternative 6 to 10.

Alternative	11	12	13	14	15
Short sentence	2SMd4.5 1SiC0.5	1SCr2 1SMd0.5 1SiC0.8 2C1.7	1SMd1 1SSi0.8 1CSi0.7 1C2.5	2SMd2.5 2SiS1.5 1SSi1	1SCr0.2 2CSi0.5 1SiC0.5 4C3.4
Layer 1	SMd	C	SMd	SSi	C
Thickness 1	3.5	0.5	1	1	1.5
Layer 2	SiC	SMd	C	SMd	SCr
Thickness 2	0.5	0.5	2.5	0.5	0.2
Layer 3	SMd	C	CSi	SiS	C
Thickness 3	1	1.2	0.7	0.5	0.7
Layer 4		SiC	SSi	SMd	Csi
Thickness 4		0.8	0.8	2	0.4
Layer 5		SCr		SiS	C
Thickness 5		2		1	0.2
Layer 6					SiC
Thickness 6					0.5
Layer 7					C
Thickness 7					1
Layer 8					CSi
Thickness 8					0.5
Layer 9					
Thickness 9					
Layer 10					
Thickness 10					
Layer 11					
Thickness 11					
Total Thickness	5	5	5	5	5
Average Kz	0.981	0.036	0.024	5.309	0.016
Average Kx/Ky	27.455	13.458	4.783	22.083	1.082
Average Eff. Por.	0.285	0.208	0.170	0.265	0.131
Average Por.	0.405	0.425	0.440	0.410	0.448

Table 18: Box model alternative 11 to 15.

Alternative	16	17	18	19	20
Short sentence	1SCr3.3 2SMd0.8 2C0.9	2SiS1 1SSi1.5 1SiC0.5 3C1.8	1SCr4 1SMd1	1SCr0.3 2SMd1 4C3.5 1P0.2	1SCr2.5 2SSi1.3 2C1.2
Layer 1	SMd	C	SCr	C	SSi
Thickness 1	0.4	0.5	4	0.5	1
Layer 2	C	SiS	SMd	P	SCr
Thickness 2	0.6	0.5	1	0.2	2.5
Layer 3	SMd	SiC		C	C
Thickness 3	0.4	0.5		2.8	0.7
Layer 4	C	SiS		SMd	SSi
Thickness 4	0.3	0.7		0.3	0.3
Layer 5	SCr	C		C	C
Thickness 5	3.3	0.8		0.1	0.5
Layer 6		SSi		SCr	
Thickness 6		1.5		0.3	
Layer 7		C		C	
Thickness 7		0.5		0.1	
Layer 8				SMd	
Thickness 8				0.7	
Layer 9					
Thickness 9					
Layer 10					
Thickness 10					
Layer 11					
Thickness 11					
Total Thickness	5	5	5	5	5
Average Kz	0.066	0.030	30.877	0.012	0.051
Average Kx/Ky	27.761	4.910	38.400	4.916	16.857
Average Eff. Por.	0.264	0.171	0.300	0.166	0.237
Average Por.	0.409	0.438	0.400	0.455	0.425

Table 19: Box model alternative 16 to 20.

Alternative	21	22	23	24	25
Short sentence	1SCr1.5 2SMd3.5	2SCr1 1SMd0.5 1Si0.5 1C3	2SMd1.5 2Si1.8 2SSi0.9 2C0.8	1SMd0.3 1Si0.8 2SSi1.4 1SiC0.3 3C1.8 P0.4	2SCr1 1SMd0.7 1Si0.5 1SSi1 1SiC0.3 3C1.1 1P0.3
Layer 1	SMd	SMd	SiS	SSi	SSi
Thickness 1	0.5	0.5	0.6	1	1
Layer 2	SCr	SCr	SMd	SMd	C
Thickness 2	1.5	0.5	0.8	0.3	0.2
Layer 3	SMd	SiS	SiS	SiC	SiC
Thickness 3	3	0.5	1.2	0.3	0.4
Layer 4		SCr	C	SiS	SMd
Thickness 4		0.5	0.3	0.8	0.7
Layer 5		C	SSi	C	SiS
Thickness 5		3	0.5	0.6	0.5
Layer 6			C	SSi	C
Thickness 6			0.5	0.4	0.4
Layer 7			SSi	C	SCr
Thickness 7			0.4	0.2	0.5
Layer 8			SMd	P	C
Thickness 8			0.7	0.4	0.5
Layer 9				C	P
Thickness 9				1	0.3
Layer 10					SCr
Thickness 10					0.5
Layer 11					
Thickness 11					
Total Thickness	5	5	5	5	5
Average Kz	19.556	0.022	0.070	0.011	0.015
Average Kx/Ky	34.400	7.986	15.377	5.434	12.729
Average Eff. Por.	0.300	0.175	0.232	0.194	0.227
Average Por.	0.400	0.430	0.417	0.475	0.455

Table 20: Box model alternative 21 to 25.

Alternative	26	27	28	29	30
Short sentence	2SCr3.6 1SMd0.3 1C0.6 1P0.5	2SCr1.4 2SMd3.1 1C0.5	2SCr2.5 1SMd0.7 1Si1 1SSi0.8	1SCr1 2SMd1.9 1Si1 1C1 1P0.1	1SCr1.5 2SMd0.5 2C2.5 1P0.5
Layer 1	SCr	SMd	SCr	SMd	C
Thickness 1	0.2	2.7	1.5	0.5	0.5
Layer 2	P	SCr	SiS	SiS	SCr
Thickness 2	0.5	0.7	1	1	1.5
Layer 3	SMd	SMd	SSi	C	SMd
Thickness 3	0.3	0.4	0.8	1	0.3
Layer 4	C	SCr	SCr	P	C
Thickness 4	0.6	0.7	1	0.1	2
Layer 5	SCr	C	SMd	SCr	P
Thickness 5	3.4	0.5	0.7	1	0.25
Layer 6				SMd	SMd
Thickness 6				1.4	0.2
Layer 7					P
Thickness 7					0.25
Layer 8					
Thickness 8					
Layer 9					
Thickness 9					
Layer 10					
Thickness 10					
Layer 11					
Thickness 11					
Total Thickness	5	5	5	5	5
Average Kz	0.010	0.115	6.874	0.030	0.010
Average Kx/Ky	29.713	28.985	28.058	21.058	10.896
Average Eff. Por.	0.290	0.280	0.274	0.253	0.214
Average Por.	0.456	0.405	0.408	0.420	0.475

Table 21: Box model alternative 26 to 30.

Appendix C - Alternative scenario variability quantification

Alt	Kz_min	Kz_max	Kxy_min	Kxy_max	EffP_min	EffP_max	P_min	P_max
1	0.12	8.96	14.92	18.97	0.24	0.26	0.42	0.41
2	0.03	7.23	8.39	13.11	0.19	0.25	0.43	0.41
3	0.96	8.98	21.58	22.97	0.26	0.27	0.41	0.40
4	0.15	4.05	4.93	6.91	0.19	0.24	0.44	0.42
5	0.03	5.64	8.20	12.62	0.19	0.23	0.43	0.41
6	0.07	0.81	17.04	19.87	0.24	0.26	0.42	0.41
7	0.04	8.67	13.52	19.03	0.22	0.25	0.42	0.41
8	0.04	12.13	18.11	23.27	0.23	0.26	0.42	0.41
9	0.23	10.43	24.30	26.24	0.27	0.28	0.41	0.40
10	0.06	5.00	7.61	10.24	0.19	0.23	0.43	0.41
11	0.98	11.84	27.45	29.26	0.29	0.29	0.41	0.40
12	0.04	11.10	13.46	19.18	0.21	0.25	0.43	0.41
13	0.02	1.49	4.78	7.05	0.17	0.21	0.44	0.43
14	5.31	11.07	22.08	24.07	0.27	0.28	0.41	0.40
15	0.02	5.99	1.08	3.29	0.13	0.22	0.45	0.42
16	0.07	15.77	27.76	31.52	0.26	0.28	0.41	0.40
17	0.03	0.19	4.91	6.93	0.17	0.20	0.44	0.43
18	30.88	30.88	38.40	38.40	0.30	0.30	0.40	0.40
19	0.01	6.63	4.92	8.18	0.17	0.23	0.46	0.43
20	0.05	2.18	16.86	19.09	0.24	0.24	0.43	0.42
21	19.56	19.56	34.40	34.40	0.30	0.30	0.40	0.40
22	0.02	7.82	7.99	11.85	0.18	0.24	0.43	0.41
23	0.07	7.41	15.38	18.44	0.23	0.25	0.42	0.41
24	0.01	5.14	5.43	8.42	0.19	0.23	0.48	0.44
25	0.01	9.12	12.73	18.23	0.23	0.26	0.46	0.43
26	0.01	19.67	29.71	32.58	0.29	0.30	0.46	0.43
27	0.12	15.36	28.98	30.98	0.28	0.29	0.41	0.40
28	6.87	14.72	28.06	29.98	0.27	0.28	0.41	0.40
29	0.03	10.18	21.06	23.53	0.25	0.27	0.42	0.41
30	0.01	9.35	10.90	15.81	0.21	0.26	0.48	0.44
31	20.00	20.00	40.00	40.00	0.30	0.30	0.40	0.40
32	8.00	8.00	32.00	32.00	0.30	0.30	0.40	0.40
33	5.00	5.00	20.00	20.00	0.25	0.25	0.40	0.40
34	0.75	0.75	6.00	6.00	0.20	0.20	0.45	0.45
35	0.30	0.30	2.50	2.50	0.20	0.20	0.45	0.45
36	0.05	0.05	0.50	0.50	0.15	0.15	0.45	0.45
37	0.005	0.005	0.05	0.05	0.10	0.10	0.45	0.45
38	0.0005	0.0005	0.001	0.001	0.44	0.44	0.90	0.90

Table 22: Alternative minimum and maximum scenario variability quantification.

Appendix D - The Kriging Calibration Figures

D.1 Horizontal Hydraulic Conductivity

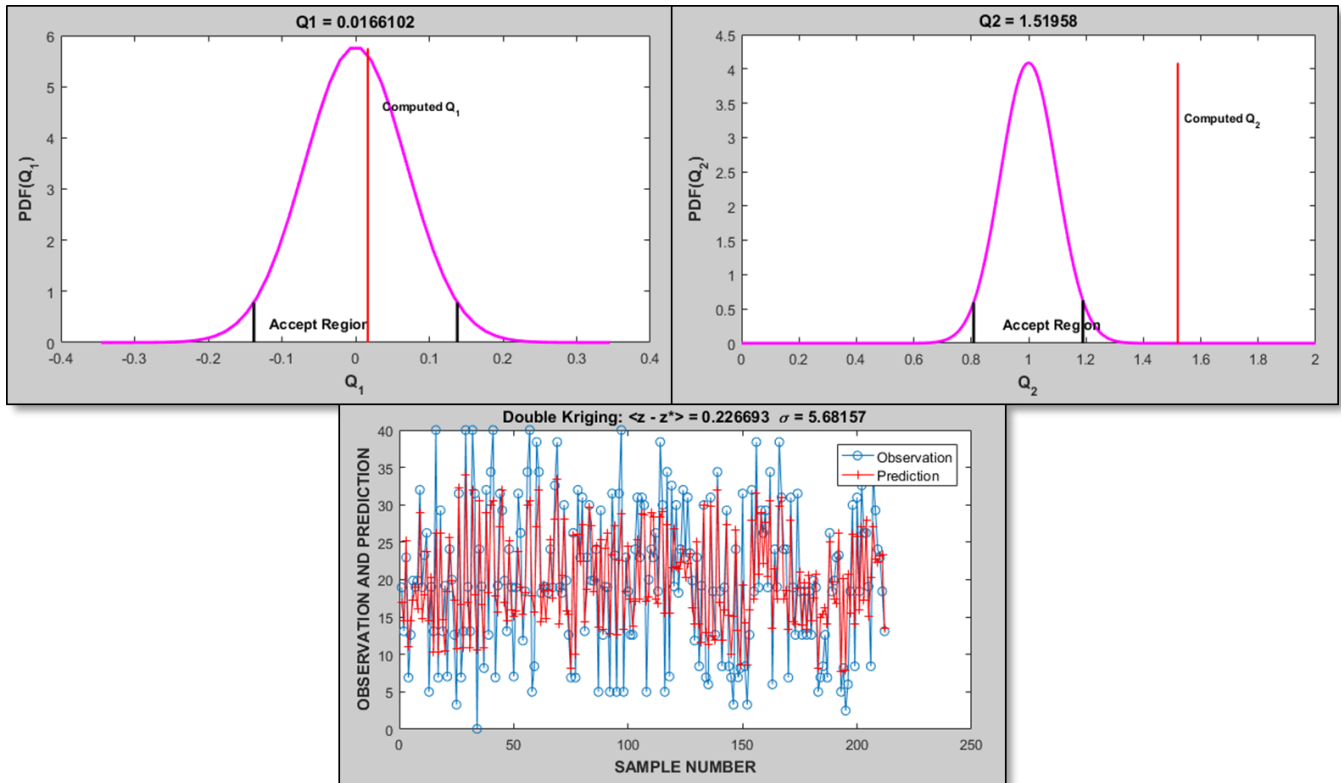


Figure 58: Horizontal hydraulic conductivity kriging calibration.

D.2 Vertical Hydraulic Conductivity

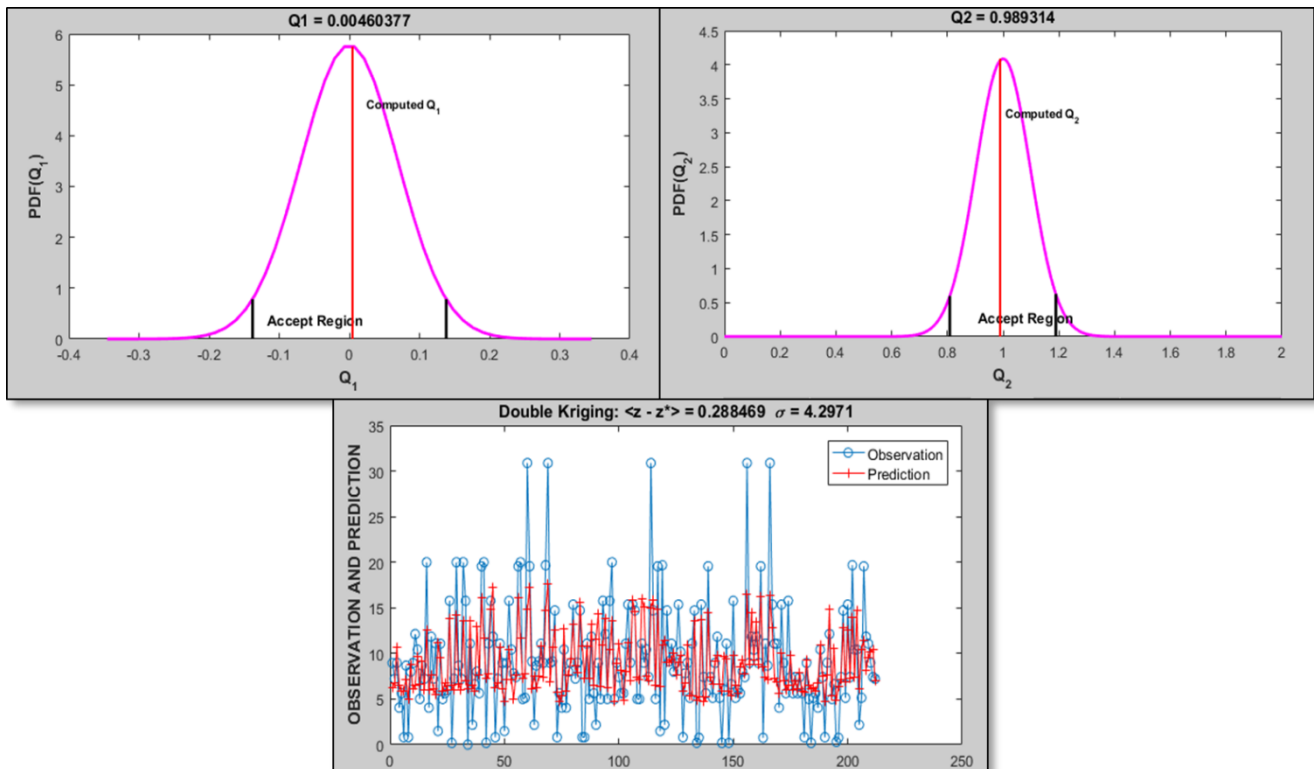


Figure 59: Vertical hydraulic conductivity kriging calibration.

D.3 Porosity

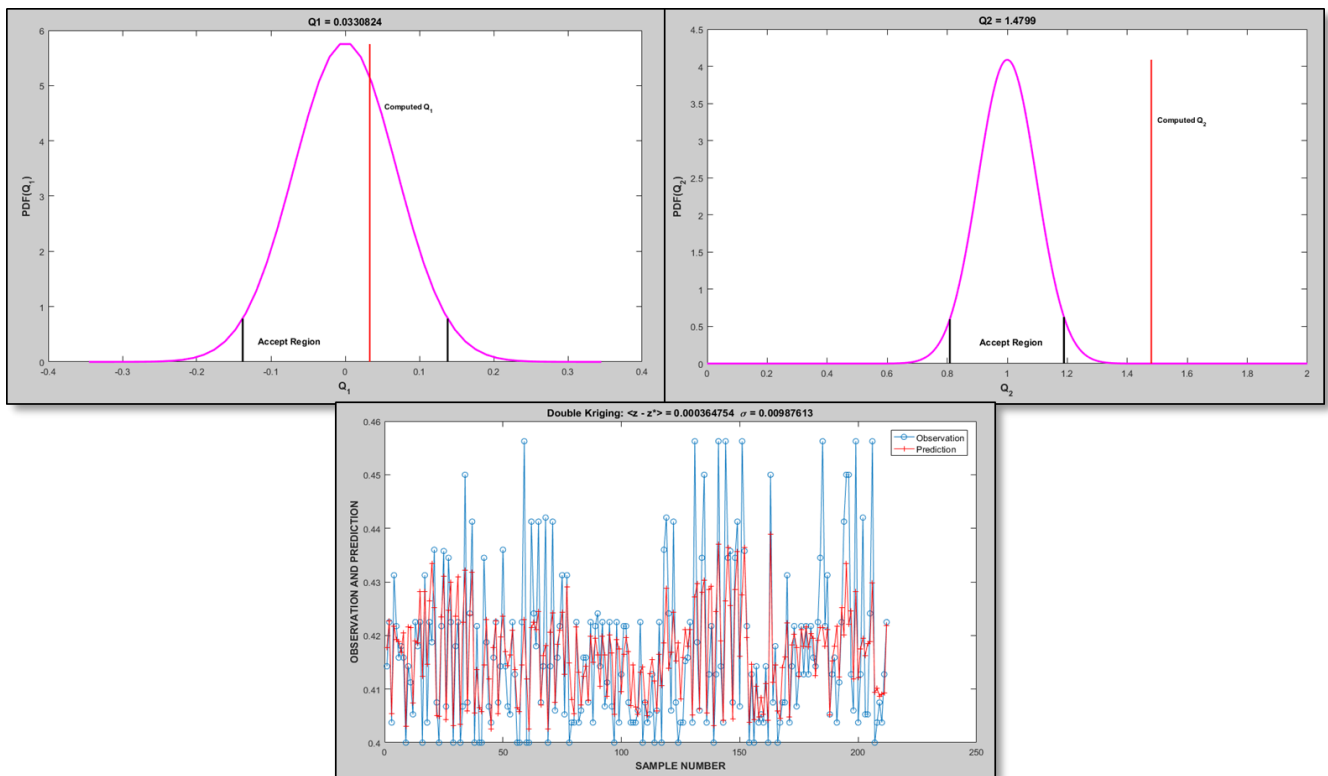


Figure 60: Porosity kriging calibration.

D.4 Effective Porosity

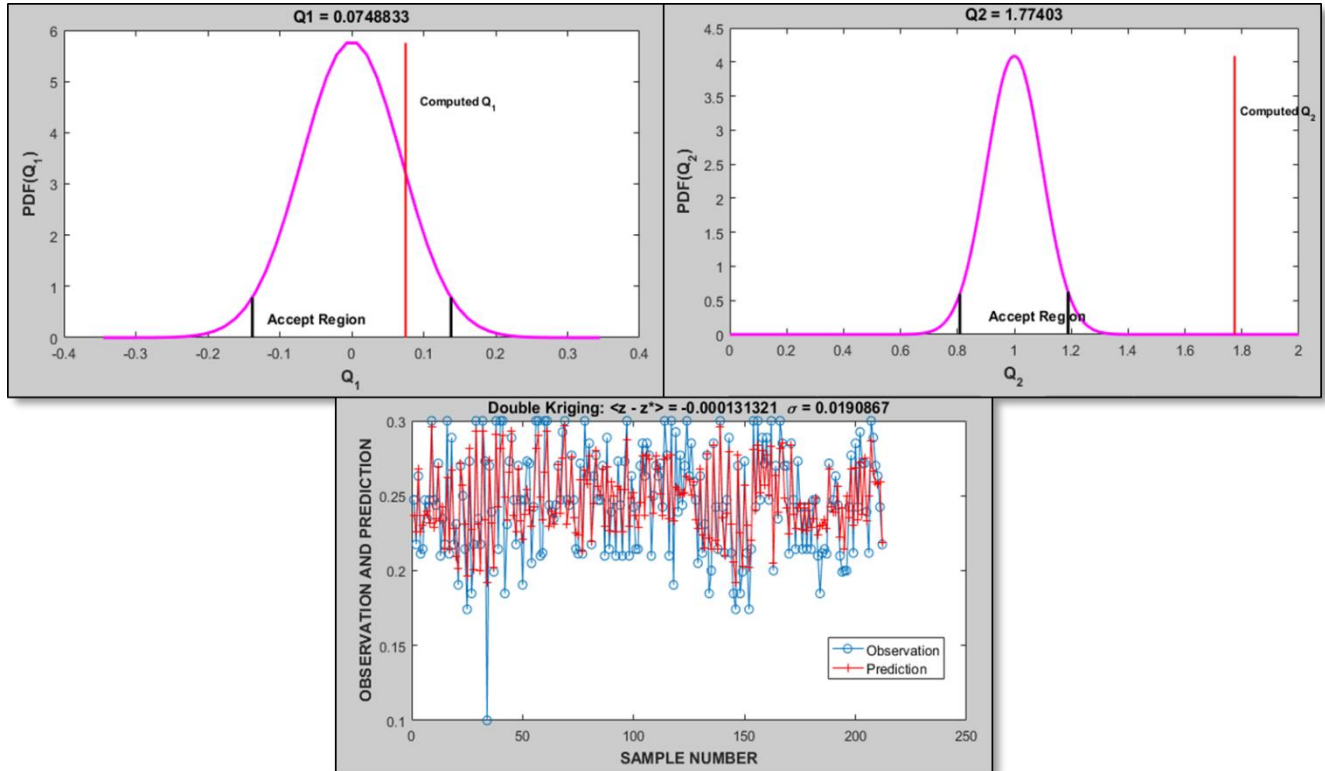


Figure 61: Effective porosity kriging calibration.

Appendix E - Orvion assessment of biological degradation constants

Assessment of biological degradation constants at Vosdonk Noord

The biological degradation of PER (tetrachloroethene) and TRI (trichloroethene) is a very specific process called "reductive dechlorination". With reductive dechlorination, the bacteria use the chlorinated solvents as a terminal electronacceptor. This process only occurs under highly reduced anaerobic conditions by specialized bacteria from the chloroflexi group. The degradation is a sequential decay process in which several lesser chlorinated intermediates occur. This process is illustrated in Figure A.

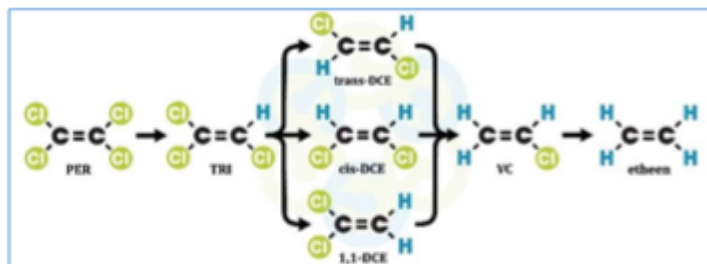


Figure A. Reductive dechlorination is a sequential decay process

Anaerobic bacteria, such as *Dehalobacter*, *Geobacter*, *Desulfitobacterium* and many others are capable of partial reductive dechlorination, from PER and TRI to cis- and trans-DCE. Only *Dehalococcoides* species are capable to degrade cis- and trans-DCE to vinyl chloride and finally to the unchlorinated and harmless ethene molecule. In practice, this means that in many mildly reduced (iron- or sulfate reducing) aquifers, which are common in The Netherlands, partial degradation tot cis-DCE occurs frequently, but complete dechlorination to ethene is rare and slow.

Orvion has performed molecular biological screening of two samples (both shallow and deep groundwater) from Vosdonk, Etten-Leur. Two methods have been used:

- A screening of the complete bacterial composition, by Next Generation Sequencing
- A quantitative analysis of the most important dechlorinating organisms, by ORVIdetect qPCR

The results of these analyses are provided in Figure B. The results show that the bacterial composition of the shallow groundwater (sample S560, well C1201, x to y m-SL) is different from the deep groundwater (sample S568, well 2714, 25-27 m-SL). In the shallow sample, bacteria from the chloroflexi group are not present. In the deep groundwater, bacteria of the chloroflexi group form 1% of the total bacteria, of which 81% is from the group of *Dehalococcoidia*. This shows that in the deep groundwater, there is potential for complete dechlorination.

The ORVIdetect qPCR analyses, which have been performed on five wells (see appendix analysecertificaat) show that:

- Complete reductive dechlorination to harmless end products occurs in two out of five wells; the numbers of *Dehalococcoides* and VC-reductase in these two wells are low and therefore indicate that this process is slow
- In four out of five wells, micro-aerophilic degradation of CIS and VC has been shown to occur (presence of the *etnE* gene); the very low numbers indicate this process is very slow
- Bacteria of the genus *Geobacter* are present in three out of five wells, in low numbers

Let *nature* do the job

These results show that there is a potential for biological dechlorination, which can be characterized as follows:

- In source zones with pure product PER or TRI, partial degradation to DCE can be expected to occur at a slow rate
- complete reductive dechlorination may not take place everywhere, but can be expected to occur in some places, at a slow rate, especially in the deep(er), more reduced groundwater
- micro-aerophilic dechlorination of CIS and VC can be expected to occur, but only at a very slow rate

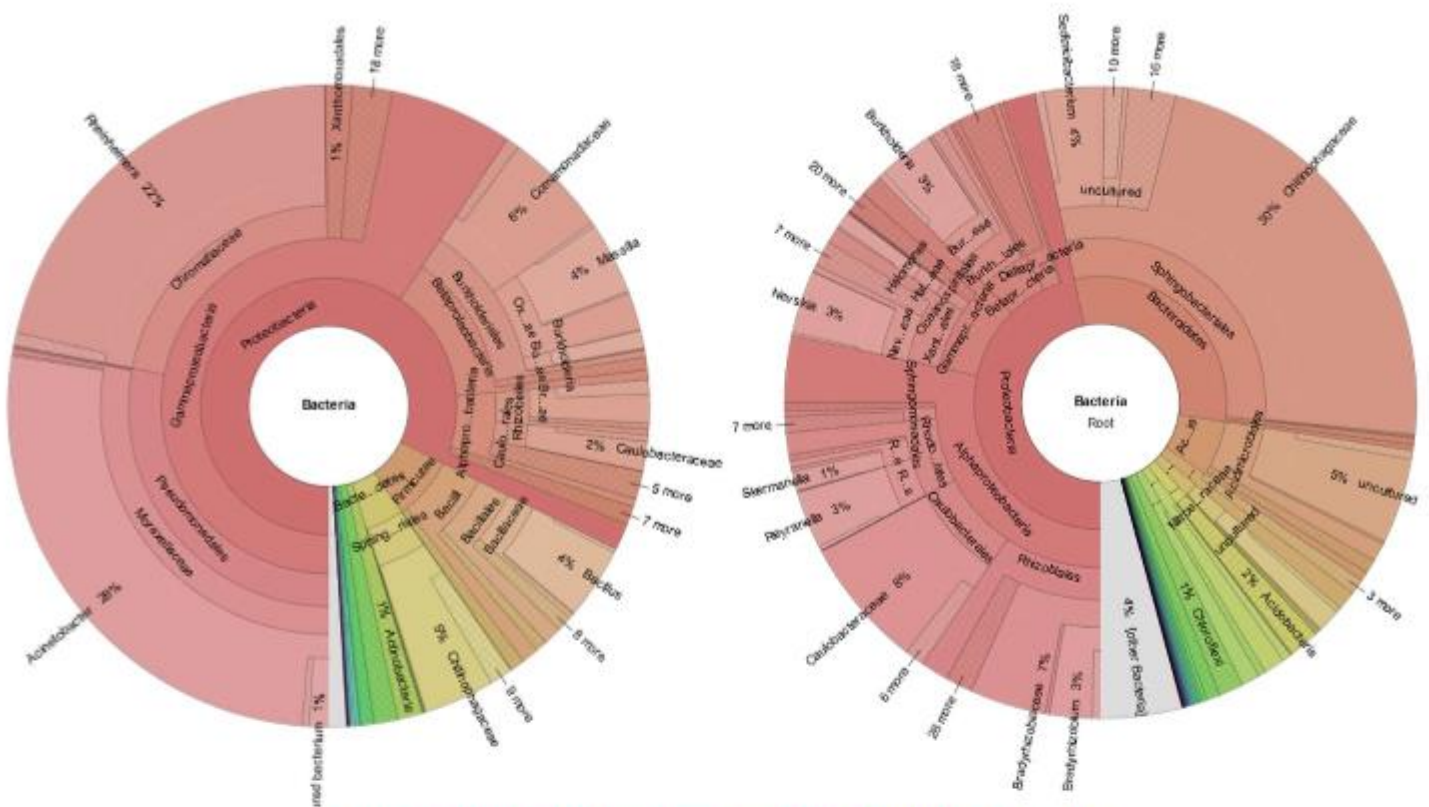


Figure B. Results of the quantitative analysis by the ORVIDetect qPCR.

Afvalzorg
t.a.v. de heer Peter Assenberg
Postbus 2
1566 ZG Assendelft

Betreft: ORVIDetect analysecertificaat
Datum: 30 januari 2017
Onze referentie: P0172
Uw referentie:
Versienummer 2

Beste heer Assenberg,

Hierbij ontvangt u het ORVIDetect analysecertificaat ten behoeve van uw project (Vosdonk-Noord te Etten-Leur). In deze versie zijn de resultaten van de nieuw ontwikkelde analyses op etnC en etnE toegevoegd.

Mocht u hieromtrent nog vragen hebben neem dan gerust contact met ons op.

Met vriendelijke groeten,



Ir. T.F.J. Verschuuren
Orvion B.V.

Analysecertificaat

Aangeleverde monsters

De door u aangegeven omschrijvingen voor de monsters zijn overgenomen in dit analyserapport.

Monster-nummer	Monsternaam	Monstercode Orvion	Monstersoort	Datum bemonstering
001	C1201	S560D05	Water	29-11-2016
002	2716	S561D05	Water	29-11-2016
003	N10 37-39	S564D02	Water	29-11-2016
004	N10 74-75	S565D02	Water	29-11-2016
005	N10 123-125	S566D02	Water	29-11-2016
006	2714 12-14	S567D02	Water	29-11-2016
007	2714 25-27	S568D03	Water	29-11-2016
008	2714 48-50	S569D02	Water	29-11-2016
009	2717 13-15	S570D02	Water	29-11-2016
010	2931 15-16	S571D02	Water	29-11-2016

Resultaten ORVIdetect analyses

In geval van niet aangetoond (N.A.) is de detectielimiet van de analyse vermeld.

ORVIdetect analyse	Artikelnr.	Eenheid*	001	002	003	004	005
Totaal bacteriën	P070P071	cellen/ml	$7,3 \cdot 10^5$	$3,7 \cdot 10^4$	$2,4 \cdot 10^5$	$9,8 \cdot 10^4$	$9,2 \cdot 10^4$
detectielimiet		cellen/ml					
Dehalococcoides sp.	P068P069	cellen/ml	N.A.	N.A.	$1,3 \cdot 10^3$	N.A.	N.A.
detectielimiet		cellen/ml	97	330		120	26
Geobacter sp.	P180P181	cellen/ml	$2,4 \cdot 10^2$	N.A.	$2,8 \cdot 10^2$	$1,0 \cdot 10^1$	N.A.
detectielimiet		cellen/ml		143			2
Dehalobacter sp.	P110P111	cellen/ml	N.A.	N.A.	N.A.	N.A.	N.A.
detectielimiet		cellen/ml	160	340	200	120	80
VC-reductase type 1	P134P135	kopieën/ml	$7,8 \cdot 10^3$	N.A.	N.A.	N.A.	N.A.
detectielimiet		kopieën/ml		143	$2,1 \cdot 10^3$	$1,3 \cdot 10^3$	870
VC-reductase type 2	P128P129	kopieën/ml	$3,5 \cdot 10^1$	N.A.	N.A.	N.A.	N.A.
detectielimiet		kopieën/ml		143	36	43	26
etnC	P258P259	kopieën/ml	$5,7 \cdot 10^1$	$1,9 \cdot 10^2$	$6,8 \cdot 10^1$	$7,4 \cdot 10^1$	8
detectielimiet		kopieën/ml					
etnE	P262P263	kopieën/ml	N.A.	N.A.	N.A.	N.A.	N.A.
detectielimiet		kopieën/ml	42	143	36	43	26

* Uitgangspunt voor kwantificatie is dat elke cel één DNA kopie bevat

ORVIdetect analyse	Artikelnr.	Eenheid*	006	007	008	009	010
Totaal bacteriën	P070P071	cellen/ml	1,1·10⁵	3,0·10⁵	1,1·10⁵	3,8·10³	1,8·10⁵
<i>detectielimiet</i>		cellen/ml					
Dehalococcoides sp.	P068P069	cellen/ml	N.A.	N.A.	N.A.	N.A.	1,7·10³
<i>detectielimiet</i>		cellen/ml	56	66	13	22	
Geobacter sp.	P180P181	cellen/ml	2,4·10¹	8,5·10¹	5,1·10²	N.A.	7,2·10²
<i>detectielimiet</i>		cellen/ml				22	
Dehalobacter sp.	P110P111	cellen/ml	N.A.	N.A.	N.A.	N.A.	N.A.
<i>detectielimiet</i>		cellen/ml	110	170	83	61	210
VC-reductase vcrA	P134P135	kopieën/ml	N.A.	N.A.	N.A.	N.A.	8,4·10⁴
<i>detectielimiet</i>		kopieën/ml	1,2·10 ³	1,8·10 ³	900	670	
VC-reductase bvcA	P128P129	kopieën/ml	N.A.	N.A.	N.A.	N.A.	4,1·10²
<i>detectielimiet</i>		kopieën/ml	56	66	13	22	
etnC	P258P259	kopieën/ml	4,9·10¹	1,0·10²	1,8·10¹	3,0·10¹	3,0·10¹
<i>detectielimiet</i>		kopieën/ml					
etnE	P262P263	kopieën/ml	N.A.	N.A.	N.A.	N.A.	N.A.
<i>detectielimiet</i>		kopieën/ml	56	66	30	22	21

* Uitgangspunt voor kwantificatie is dat elke cel één DNA kopie bevat

Appendix F - Matlab Scripts

F.1 DataPrep_Random script

Clear Command window and workspace

```
clear, clc
```

Import Data files

```
Alt = xlsread('Alternatives_EasyKrig3D.xlsx');  
Data = xlsread('CPT_Data_interpretation.xlsx');
```

Applying alternative values to the box data

```
for nn = 1:22  
  
    % Generating the random values between zero and 1  
    % Each alternative is assigned a unique random value.  
    rand1 = rand(1), rand2 = rand(1), rand3 = rand(1), rand4 = rand(1),  
    rand5 = rand(1), rand6 = rand(1), rand7 = rand(1), rand8 = rand(1),  
    rand9 = rand(1), rand10 = rand(1), rand11 = rand(1), rand12 = rand(1),  
    rand13 = rand(1), rand14 = rand(1), rand15 = rand(1), rand16 = rand(1),  
    rand17 = rand(1), rand18 = rand(1), rand19 = rand(1), rand20 = rand(1),  
    rand21 = rand(1), rand22 = rand(1), rand23 = rand(1), rand24 = rand(1),  
    rand25 = rand(1), rand26 = rand(1), rand27 = rand(1), rand28 = rand(1),  
    rand29 = rand(1), rand30 = rand(1)  
  
    % Preparation of the data structure in matrix form  
    Kz = [Data(:,1),Data(:,2),Data(:,4),zeros(length(Data(:,1)),1)];  
    Kxy = [Data(:,1),Data(:,2),Data(:,4),zeros(length(Data(:,1)),1)];  
    EffP = [Data(:,1),Data(:,2),Data(:,4),zeros(length(Data(:,1)),1)];  
    Por = [Data(:,1),Data(:,2),Data(:,4),zeros(length(Data(:,1)),1)];  
  
    % Replacement of the alternative number with the corresponding  
    % parameter value  
    for ii = 1:length(Data(:,1))  
        if Data(ii,5) == 1  
            Kz(ii,4) = Alt(1,2)+(rand1*(Alt(1,6)-Alt(1,2)));  
            Kxy(ii,4) = Alt(1,3)+(rand1*(Alt(1,7)-Alt(1,3)));  
            EffP(ii,4) = (Alt(1,4)+Alt(1,8))/2;  
            Por(ii,4) = (Alt(1,5)+Alt(1,9))/2;  
        elseif Data(ii,5) == 2  
            Kz(ii,4) = Alt(2,2)+(rand2*(Alt(2,6)-Alt(2,2)));  
            Kxy(ii,4) = Alt(2,3)+(rand2*(Alt(2,7)-Alt(2,3)));  
            EffP(ii,4) = (Alt(2,4)+Alt(2,8))/2;  
            Por(ii,4) = (Alt(2,5)+Alt(2,9))/2;  
        elseif Data(ii,5) == 3  
            Kz(ii,4) = Alt(3,2)+(rand3*(Alt(3,6)-Alt(3,2)));  
            Kxy(ii,4) = Alt(3,3)+(rand3*(Alt(3,7)-Alt(3,3)));  
            EffP(ii,4) = (Alt(3,4)+Alt(3,8))/2;  
            Por(ii,4) = (Alt(3,5)+Alt(3,9))/2;  
        elseif Data(ii,5) == 4  
            Kz(ii,4) = Alt(4,2)+(rand4*(Alt(4,6)-Alt(4,2)));  
            Kxy(ii,4) = Alt(4,3)+(rand4*(Alt(4,7)-Alt(4,3)));  
            EffP(ii,4) = (Alt(4,4)+Alt(4,8))/2;  
            Por(ii,4) = (Alt(4,5)+Alt(4,9))/2;  
        end  
    end  
end
```

```

elseif Data(ii,5) == 5
    Kz(ii,4) = Alt(5,2)+(rand5*(Alt(5,6)-Alt(5,2)));
    Kxy(ii,4) = Alt(5,3)+(rand5*(Alt(5,7)-Alt(5,3)));
    EffP(ii,4) = (Alt(5,4)+Alt(5,8))/2;
    Por(ii,4) = (Alt(5,5)+Alt(5,9))/2;
elseif Data(ii,5) == 6
    Kz(ii,4) = Alt(6,2)+(rand6*(Alt(6,6)-Alt(6,2)));
    Kxy(ii,4) = Alt(6,3)+(rand6*(Alt(6,7)-Alt(6,3)));
    EffP(ii,4) = (Alt(6,4)+Alt(6,8))/2;
    Por(ii,4) = (Alt(6,5)+Alt(6,9))/2;
elseif Data(ii,5) == 7
    Kz(ii,4) = Alt(7,2)+(rand7*(Alt(7,6)-Alt(7,2)));
    Kxy(ii,4) = Alt(7,3)+(rand7*(Alt(7,7)-Alt(7,3)));
    EffP(ii,4) = (Alt(7,4)+Alt(7,8))/2;
    Por(ii,4) = (Alt(7,5)+Alt(7,9))/2;
elseif Data(ii,5) == 8
    Kz(ii,4) = Alt(8,2)+(rand8*(Alt(8,6)-Alt(8,2)));
    Kxy(ii,4) = Alt(8,3)+(rand8*(Alt(8,7)-Alt(8,3)));
    EffP(ii,4) = (Alt(8,4)+Alt(8,8))/2;
    Por(ii,4) = (Alt(8,5)+Alt(8,9))/2;
elseif Data(ii,5) == 9
    Kz(ii,4) = Alt(9,2)+(rand9*(Alt(9,6)-Alt(9,2)));
    Kxy(ii,4) = Alt(9,3)+(rand9*(Alt(9,7)-Alt(9,3)));
    EffP(ii,4) = (Alt(9,4)+Alt(9,8))/2;
    Por(ii,4) = (Alt(9,5)+Alt(9,9))/2;
elseif Data(ii,5) == 10
    Kz(ii,4) = Alt(10,2)+(rand10*(Alt(10,6)-Alt(10,2)));
    Kxy(ii,4) = Alt(10,3)+(rand10*(Alt(10,7)-Alt(10,3)));
    EffP(ii,4) = (Alt(10,4)+Alt(10,8))/2;
    Por(ii,4) = (Alt(10,5)+Alt(10,9))/2;
elseif Data(ii,5) == 11
    Kz(ii,4) = Alt(11,2)+(rand11*(Alt(11,6)-Alt(11,2)));
    Kxy(ii,4) = Alt(11,3)+(rand11*(Alt(11,7)-Alt(11,3)));
    EffP(ii,4) = (Alt(11,4)+Alt(11,8))/2;
    Por(ii,4) = (Alt(11,5)+Alt(11,9))/2;
elseif Data(ii,5) == 12
    Kz(ii,4) = Alt(12,2)+(rand12*(Alt(12,6)-Alt(12,2)));
    Kxy(ii,4) = Alt(12,3)+(rand12*(Alt(12,7)-Alt(12,3)));
    EffP(ii,4) = (Alt(12,4)+Alt(12,8))/2;
    Por(ii,4) = (Alt(12,5)+Alt(12,9))/2;
elseif Data(ii,5) == 13
    Kz(ii,4) = Alt(13,2)+(rand13*(Alt(13,6)-Alt(13,2)));
    Kxy(ii,4) = Alt(13,3)+(rand13*(Alt(13,7)-Alt(13,3)));
    EffP(ii,4) = (Alt(13,4)+Alt(13,8))/2;
    Por(ii,4) = (Alt(13,5)+Alt(13,9))/2;
elseif Data(ii,5) == 14
    Kz(ii,4) = Alt(14,2)+(rand14*(Alt(14,6)-Alt(14,2)));
    Kxy(ii,4) = Alt(14,3)+(rand14*(Alt(14,7)-Alt(14,3)));
    EffP(ii,4) = (Alt(14,4)+Alt(14,8))/2;
    Por(ii,4) = (Alt(14,5)+Alt(14,9))/2;
elseif Data(ii,5) == 15
    Kz(ii,4) = Alt(15,2)+(rand15*(Alt(15,6)-Alt(15,2)));
    Kxy(ii,4) = Alt(15,3)+(rand15*(Alt(15,7)-Alt(15,3)));
    EffP(ii,4) = (Alt(15,4)+Alt(15,8))/2;
    Por(ii,4) = (Alt(15,5)+Alt(15,9))/2;
elseif Data(ii,5) == 16
    Kz(ii,4) = Alt(16,2)+(rand16*(Alt(16,6)-Alt(16,2)));
    Kxy(ii,4) = Alt(16,3)+(rand16*(Alt(16,7)-Alt(16,3)));

```

```

    EffP(ii,4) = (Alt(16,4)+Alt(16,8))/2;
    Por(ii,4) = (Alt(16,5)+Alt(16,9))/2;
elseif Data(ii,5) == 17
    Kz(ii,4) = Alt(17,2)+(rand17*(Alt(17,6)-Alt(17,2)));
    Kxy(ii,4) = Alt(17,3)+(rand17*(Alt(17,7)-Alt(17,3)));
    EffP(ii,4) = (Alt(17,4)+Alt(17,8))/2;
    Por(ii,4) = (Alt(17,5)+Alt(17,9))/2;
elseif Data(ii,5) == 18
    Kz(ii,4) = Alt(18,2)+(rand18*(Alt(18,6)-Alt(18,2)));
    Kxy(ii,4) = Alt(18,3)+(rand18*(Alt(18,7)-Alt(18,3)));
    EffP(ii,4) = (Alt(18,4)+Alt(18,8))/2;
    Por(ii,4) = (Alt(18,5)+Alt(18,9))/2;
elseif Data(ii,5) == 19
    Kz(ii,4) = Alt(19,2)+(rand19*(Alt(19,6)-Alt(19,2)));
    Kxy(ii,4) = Alt(19,3)+(rand19*(Alt(19,7)-Alt(19,3)));
    EffP(ii,4) = (Alt(19,4)+Alt(19,8))/2;
    Por(ii,4) = (Alt(19,5)+Alt(19,9))/2;
elseif Data(ii,5) == 20
    Kz(ii,4) = Alt(20,2)+(rand20*(Alt(20,6)-Alt(20,2)));
    Kxy(ii,4) = Alt(20,3)+(rand20*(Alt(20,7)-Alt(20,3)));
    EffP(ii,4) = (Alt(20,4)+Alt(20,8))/2;
    Por(ii,4) = (Alt(20,5)+Alt(20,9))/2;
elseif Data(ii,5) == 21
    Kz(ii,4) = Alt(21,2)+(rand21*(Alt(21,6)-Alt(21,2)));
    Kxy(ii,4) = Alt(21,3)+(rand21*(Alt(21,7)-Alt(21,3)));
    EffP(ii,4) = (Alt(21,4)+Alt(21,8))/2;
    Por(ii,4) = (Alt(21,5)+Alt(21,9))/2;
elseif Data(ii,5) == 22
    Kz(ii,4) = Alt(22,2)+(rand22*(Alt(22,6)-Alt(22,2)));
    Kxy(ii,4) = Alt(22,3)+(rand22*(Alt(22,7)-Alt(22,3)));
    EffP(ii,4) = (Alt(22,4)+Alt(22,8))/2;
    Por(ii,4) = (Alt(22,5)+Alt(22,9))/2;
elseif Data(ii,5) == 23
    Kz(ii,4) = Alt(23,2)+(rand23*(Alt(23,6)-Alt(23,2)));
    Kxy(ii,4) = Alt(23,3)+(rand23*(Alt(23,7)-Alt(23,3)));
    EffP(ii,4) = (Alt(23,4)+Alt(23,8))/2;
    Por(ii,4) = (Alt(23,5)+Alt(23,9))/2;
elseif Data(ii,5) == 24
    Kz(ii,4) = Alt(24,2)+(rand24*(Alt(24,6)-Alt(24,2)));
    Kxy(ii,4) = Alt(24,3)+(rand24*(Alt(24,7)-Alt(24,3)));
    EffP(ii,4) = (Alt(24,4)+Alt(24,8))/2;
    Por(ii,4) = (Alt(24,5)+Alt(24,9))/2;
elseif Data(ii,5) == 25
    Kz(ii,4) = Alt(25,2)+(rand25*(Alt(25,6)-Alt(25,2)));
    Kxy(ii,4) = Alt(25,3)+(rand25*(Alt(25,7)-Alt(25,3)));
    EffP(ii,4) = (Alt(25,4)+Alt(25,8))/2;
    Por(ii,4) = (Alt(25,5)+Alt(25,9))/2;
elseif Data(ii,5) == 26
    Kz(ii,4) = Alt(26,2)+(rand26*(Alt(26,6)-Alt(26,2)));
    Kxy(ii,4) = Alt(26,3)+(rand26*(Alt(26,7)-Alt(26,3)));
    EffP(ii,4) = (Alt(26,4)+Alt(26,8))/2;
    Por(ii,4) = (Alt(26,5)+Alt(26,9))/2;
elseif Data(ii,5) == 27
    Kz(ii,4) = Alt(27,2)+(rand27*(Alt(27,6)-Alt(27,2)));
    Kxy(ii,4) = Alt(27,3)+(rand27*(Alt(27,7)-Alt(27,3)));
    EffP(ii,4) = (Alt(27,4)+Alt(27,8))/2;
    Por(ii,4) = (Alt(27,5)+Alt(27,9))/2;
elseif Data(ii,5) == 28

```

```

        Kz(ii,4) = Alt(28,2)+(rand28*(Alt(28,6)-Alt(28,2)));
        Kxy(ii,4) = Alt(28,3)+(rand28*(Alt(28,7)-Alt(28,3)));
        EffP(ii,4) = (Alt(28,4)+Alt(28,8))/2;
        Por(ii,4) = (Alt(28,5)+Alt(28,9))/2;
elseif Data(ii,5) == 29
    Kz(ii,4) = Alt(29,2)+(rand29*(Alt(29,6)-Alt(29,2)));
    Kxy(ii,4) = Alt(29,3)+(rand29*(Alt(29,7)-Alt(29,3)));
    EffP(ii,4) = (Alt(29,4)+Alt(29,8))/2;
    Por(ii,4) = (Alt(29,5)+Alt(29,9))/2;
elseif Data(ii,5) == 30
    Kz(ii,4) = Alt(30,2)+(rand30*(Alt(30,6)-Alt(30,2)));
    Kxy(ii,4) = Alt(30,3)+(rand30*(Alt(30,7)-Alt(30,3)));
    EffP(ii,4) = (Alt(30,4)+Alt(30,8))/2;
    Por(ii,4) = (Alt(30,5)+Alt(30,9))/2;
elseif Data(ii,5) == 31
    Kz(ii,4) = Alt(31,2);
    Kxy(ii,4) = Alt(31,3);
    EffP(ii,4) = Alt(31,4);
    Por(ii,4) = Alt(31,5);
elseif Data(ii,5) == 32
    Kz(ii,4) = Alt(32,2);
    Kxy(ii,4) = Alt(32,3);
    EffP(ii,4) = Alt(32,4);
    Por(ii,4) = Alt(32,5);
elseif Data(ii,5) == 33
    Kz(ii,4) = Alt(33,2);
    Kxy(ii,4) = Alt(33,3);
    EffP(ii,4) = Alt(33,4);
    Por(ii,4) = Alt(33,5);
elseif Data(ii,5) == 34
    Kz(ii,4) = Alt(34,2);
    Kxy(ii,4) = Alt(34,3);
    EffP(ii,4) = Alt(34,4);
    Por(ii,4) = Alt(34,5);
elseif Data(ii,5) == 35
    Kz(ii,4) = Alt(35,2);
    Kxy(ii,4) = Alt(35,3);
    EffP(ii,4) = Alt(35,4);
    Por(ii,4) = Alt(35,5);
elseif Data(ii,5) == 36
    Kz(ii,4) = Alt(36,2);
    Kxy(ii,4) = Alt(36,3);
    EffP(ii,4) = Alt(36,4);
    Por(ii,4) = Alt(36,5);
elseif Data(ii,5) == 37
    Kz(ii,4) = Alt(37,2);
    Kxy(ii,4) = Alt(37,3);
    EffP(ii,4) = Alt(37,4);
    Por(ii,4) = Alt(37,5);
else
    Kz(ii,4) = Alt(38,2);
    Kxy(ii,4) = Alt(38,3);
    EffP(ii,4) = Alt(38,4);
    Por(ii,4) = Alt(38,5);
end
end
end

```


Export of the generated box data points

```
dlmwrite(sprintf('Kz_rand%d.txt', nn), Kz); %Vertical hydraulic conductivity
dlmwrite(sprintf('Kxy_rand%d.txt', nn), Kxy); %Horizontal hydraulic conductivity
dlmwrite(sprintf('EffP_min.txt', nn), EffP); %Effective Porosity
dlmwrite(sprintf('Por_min.txt', nn), Por); %Porosity

end
```

Published with MATLAB® R2016a

F.2 Kriging_VisualPrep_Layer1 script

Clear Workspace and Command Window

```
clear, clc
```

For loop batch process

```
for count = 1:22
```

Loading the Hydraulic Conductivity Data

```
filenameKz = sprintf('Kz_rand%d.mat', count)
filenameKxy = sprintf('Kxy_rand%d.mat', count)
Kz_rand = load(filenameKz);
Kxy_rand = load(filenameKxy);
```

Generating table from 3D Kriging Data

```
krig3D_Kz = Kz_rand.data.out.krig.Vg; %Assigning Kz kriging dataset
krig3D_Kxy = Kxy_rand.data.out.krig.Vg; %Assigning Kxy kriging dataset

% Reserving array parameter space
row = [];
column = [];
layer = [];
Kz = [];
Kxy = [];

% Assigning the kriging cell values to the appropriate model location
% parameter values (row, column, layer = xcell, ycell, zcell)
for ii = 5 %In this case layer 1 (5 = layer 1, 4 = layer 2, etc.)
    for kk = linspace(1,123,123)
        for jj = linspace(1,123,123)
            y=139-jj;
            row = [row y];
            x=kk+144;
            column = [column x];
            z=6-ii;
            layer = [layer z];
            aa = krig3D_Kz(jj, kk, ii);
            if aa == 0
                aa = aa +0.003;
            else
                aa = aa;
```

```

        end
        Kz = [Kz aa];
        bb = krig3D_Kxy(jj, kk, ii);
        if bb == 0
            bb = bb + 0.003;
        else
            bb = bb;
        end
        Kxy = [Kxy bb];
    end
end

% Remaining values already present in the model per layer

% It is necessary to add these values to the dataset as Visual Modflow
% only accepts importation of values of the layer in case every
% cell in the model can be assigned a parameter value.
ModelKxy = [2.5; 6; 0.005; 12; 12];
ModelKz = [0.1; 1; 0.0005; 3; 3];
for ll = 5
    for nn = linspace(1, 123, 123)
        for mm = linspace(1, 15, 15)
            y = mm;
            row = [row y];
            x = nn + 144;
            column = [column x];
            z = 6 - ll;
            layer = [layer z];
            cc = ModelKz(6 - ll);
            Kz = [Kz cc];
            dd = ModelKxy(6 - ll);
            Kxy = [Kxy dd];
        end
    end
end

for ll = 5
    for nn = linspace(1, 144, 144)
        for mm = linspace(1, 138, 138)
            y = mm;
            row = [row y];
            x = nn;
            column = [column x];
            z = 6 - ll;
            layer = [layer z];
            cc = ModelKz(6 - ll);
            Kz = [Kz cc];
            dd = ModelKxy(6 - ll);
            Kxy = [Kxy dd];
        end
    end
end
end

```

Creating Output table and exporting to .txt

```
    Krig_InputVisual_layer =  
    [transpose(row),transpose(column),transpose(layer),transpose(kxy),transpose(kxy),transpose(kz)  
    ];  
  
    %dlmwrite(sprintf('K_rand%d_layer1.txt', count), Krig_InputVisual_layer);  
  
end
```

Published with MATLAB® R2016a

F.3 Flowdata_ran function

```
function [v3D, x2D, x3D, TStart, TSTEP] = FlowData_Ran(DataFile)  
% This function loads in the shapefile containing the flowline data  
% exported from Visual Modflow. It orders the components necessary  
% for the 1D solute transport model and generates 2D and 3D travelled  
% distance and velocity data of the behaviour of the flowline between the  
% successive time steps about the start coordinate of the flowline.  
  
% Loading in shapefile data and sorting time elapsed in chronologic order.  
shpfile = shaperead([DataFile, '.shp']);  
[~,index] = sortrows([shpfile.TRAVELTIME].'); shpfile = shpfile(index); clear index  
  
% Assigning coordinate, travel time and start time data to a variable  
X = [shpfile.X];  
Y = [shpfile.Y];  
Z = [shpfile.Z];  
TTIME = [shpfile.TRACKTIME];  
STIME = [shpfile.SIMULTIME];  
  
X1 = X;  
Y1 = Y;  
Z1 = Z;  
  
% Conducting the calculations for successive time step data.  
for ii = 1:length(X1)-1  
    x2D(ii) = sqrt((X1(ii+1)-X1(ii))^2+(Y1(ii+1)-Y1(ii))^2);  
    for jj = 1:length(x2D)  
        x3D(jj) = sqrt((x2D(jj))^2+(Z1(jj+1)-Z1(jj))^2);  
    end  
end  
  
% Calculating velocity data and assigning start time and time step to a variable  
TSTEP = TTIME(2); % Timestep  
v3D = x3D / TSTEP; % Velocity data  
TStart = 1975+(STIME(1)/365.25); % Start year  
end
```

Published with MATLAB® R2016a

F.4 Flowline1_RandomSimu script

clear workspace

```
clear
clc
```

Reserving Probability values arrays

```
Prob_values_PER = [];
Prob_values_TRI = [];
Prob_values_CIS = [];
Prob_values_VC = [];
Prob_values_ET = [];

% PER = Tetrachloroethene
% TRI = Trichloroethene
% CIS = CIS-1,2-Di-Chloroethene
% VC = vinyl Chloride
% ET = Ethene
```

Multiple simulation counter

```
for count = 1:22
```

Calling Flow line data (Krigmax = number 21 and Krigmin is number 22)

```
DataFile = sprintf('Flow1_Krig%d',count);
[v3D, x2D, x3D, Tstart, TSTEP] = FlowData_Ran(DataFile);
```

Define overall variables

```
xmin = 0; % Start travelled distance (m)
xmax = sum(x3D); % End travelled distance (m)
N = size(x3D,2); % Total amount of Nodes
dt = TSTEP; % Stepsize (days)
t = []; % Start travelled time (d)
v = v3D; % Waterflow velocity (m/d)
dx = x3D; % Waterflow travelled distances (m)
```

Contaminant specific variables

```
R_PER = 5.8; R_TRI = 2.605; R_CIS = 2.74; R_VC = 1.66; R_ET = 1; %Retardation coefficients
(-)
u_PER = 0.00126; u_TRI = 0.0001; u_CIS = 0.0000001; u_VC = 0.0006; u_ET = 0.00; %Decay in
1/days
Ycoeff_TRI = 0.79; Ycoeff_CIS = 0.74; Ycoeff_VC = 0.64; Ycoeff_ET = 0.45; %Yield coefficients
(-)
u_2MonthFactor = 60.875; %because 1 timestep is two months | 60.875 days.
```

Discretizing the domain

```
x = [];
x(1) = 0;
for ii = 1:length(dx)
```



```

x(ii+1) = x(ii) + dx(ii);
end
x = [xmin - dx(1), x, xmax + dx(N)]; %Adding the 2 ghost nodes

```

Initial conditions (\mu g/L)

```

c0_PER = 27; c0_TRI = 1900; c0_CIS = 27000; c0_VC = 170; c0_ET = 0.0;
c_PER = zeros(length(x),N); % Constructing the data array
c_PER(2,:) = c0_PER; % Inserting the initial condition value.
c_TRI = zeros(length(x),N);
c_TRI(2,1) = c0_TRI;
c_CIS = zeros(length(x),N);
c_CIS(2,1) = c0_CIS;
c_VC = zeros(length(x),N);
c_VC(2,1) = c0_VC;
c_ET = zeros(length(x),N);
c_ET(2,1) = c0_ET;

% Specifying the initial condition array of the following step
c_up_PER = c_PER; c_up_TRI = c_TRI; c_up_CIS = c_CIS; c_up_VC = c_VC; c_up_ET = c_ET;

```

Explicit Forward Difference Calculations

```

nsteps = N+55*6; % Extra calculation steps are added to create the effect of continuing
calculations over the discretised domain
for nn = 1 : nsteps

    % Boundary conditions (Neumann boundary)
    c_PER(1,nn) = c_PER(3,nn); c_TRI(1,nn) = c_TRI(3,nn); c_CIS(1,nn) = c_CIS(3,nn);
    c_VC(1,nn) = c_VC(3,nn); c_ET(1,nn) = c_ET(3,nn);
    c_PER(N+3,nn) = c_PER(N+1,nn); c_TRI(N+3,nn) = c_TRI(N+1,nn); c_CIS(N+3,nn) =
c_CIS(N+1,nn);
    c_VC(N+3,nn) = c_VC(N+1,nn); c_ET(N+3,nn) = c_ET(N+1,nn);

    % Restating initial conditions for the ending of contaminant spread
    % (Back of the contaminant plume) Initial conditions all zero
    % concentration
    if nn > ((2023-2001)*6)
        c_PER(2,nn) = 0; c_TRI(2,nn) = 0; c_CIS(2,nn) = 0; c_VC(2,nn) = 0; c_ET(2,nn)=0;
    end

    % Calculating the advection values of each contaminant
    for jj = 2 : N+1
        Adv(jj,nn) = (-v(jj-1)*dt/dx(jj-1));
    end

    Adv_PER = Adv/R_PER; Adv_TRI = Adv/R_TRI; Adv_CIS = Adv/R_CIS;
    Adv_VC = Adv/R_VC; Adv_ET = Adv/R_ET;

    % Calculate the FOU scheme derived from the governing equation
    for kk = 2 : N + 2
        c_up_PER(kk,nn) = c_PER(kk,nn) + Adv_PER(kk-1,nn) * (c_PER(kk,nn) - c_PER(kk-
1,nn)) - ((u_PER*c_PER(kk,nn))*u_2MonthFactor);
        c_up_TRI(kk,nn) = c_TRI(kk,nn) + Adv_TRI(kk-1,nn) * (c_TRI(kk,nn) - c_TRI(kk-
1,nn)) - ((u_TRI*c_TRI(kk,nn))*u_2MonthFactor) +
(((Ycoeff_TRI*u_PER)*c_PER(kk,nn))*u_2MonthFactor);
    end
end

```

```

        c_up_CIS(kk,nn) = c_CIS(kk,nn) + Adv_CIS(kk-1,nn) * (c_CIS(kk,nn) - c_CIS(kk-1,nn)) - ((u_CIS*c_CIS(kk,nn))*u_2MonthFactor) +
        (((Ycoff_CIS*u_TRI)*c_TRI(kk,nn))*u_2MonthFactor);
        c_up_VC(kk,nn) = c_VC(kk,nn) + Adv_VC(kk-1) * (c_VC(kk,nn) - c_VC(kk-1,nn)) -
        ((u_VC*c_VC(kk,nn))*u_2MonthFactor) + (((Ycoff_VC*u_CIS)*c_CIS(kk,nn))*u_2MonthFactor);
        c_up_ET(kk,nn) = c_ET(kk,nn) + Adv_ET(kk-1) * (c_ET(kk,nn) - c_ET(kk-1,nn)) -
        ((u_ET*c_ET(kk,nn))*u_2MonthFactor) + (((Ycoff_ET*u_VC)*c_VC(kk,nn))*u_2MonthFactor);
    end

    % Updating and saving the time and concentration values
    t(nn+1) = t(nn) + dt;
    c_PER(:,nn+1) = c_up_PER(:,nn); c_TRI(:,nn+1) = c_up_TRI(:,nn); c_CIS(:,nn+1) =
c_up_CIS(:,nn);
    c_VC(:,nn+1) = c_up_VC(:,nn); c_ET(:,nn+1) = c_up_ET(:,nn);

    % Renewing the initial conditions (Continues spill of contaminant of PER)
    c_PER(2,nn+1) = c0_PER;

end

```

Figures

```

year_start = TStart; % Start year for plotting
year_end = max(year_start+(t/365.25)); % End year for plotting
year = 2041; % Year of interest for plotting
year_fig = ((year - year_start)*365.25)/dt; % years elapsed from start

figure(1), hold on
pltX_PER = plot(x(2:N+2),c_PER(2:N+2,year_fig),'b-');
pltX_TRI = plot(x(2:N+2),c_TRI(2:N+2,year_fig),'y-');
pltX_VC = plot(x(2:N+2),c_VC(2:N+2,year_fig),'c-');
pltX_ET = plot(x(2:N+2),c_ET(2:N+2,year_fig),'r-');
plot(x(N+2),c_PER(N+2,year_fig),'.k','markersize',10);
plot(x(N+2),c_TRI(N+2,year_fig),'.k','markersize',10);
plot(x(N+2),c_VC(N+2,year_fig),'.k','markersize',10);
plot(x(N+2),c_ET(N+2,year_fig),'.k','markersize',10);
xlim([0, 370])
ylim([0 inf])
title_tekst1 = sprintf('Flowline 1 | Kriging: Concentration over the distance in %d',
year);
title(title_tekst1)
legend('Tetrachloroethene', 'Trichloroethene', 'Vinyl Chloride', 'Ethene','River
Location','Location','best')
ylabel('Concentration (\mug/L)')
xlabel('Distance (m)')
set(gca,'YTickLabel',num2str(get(gca,'YTick').'))
hold off

figure(2), hold on
pltX_CIS = plot(x(2:N+2),c_CIS(2:N+2,year_fig),'m-');
plot(x(N+2),c_CIS(N+2,year_fig),'.k','markersize',10);
xlim([0, 370])
ylim([0 inf])
title_tekst2 = sprintf('Flowline 1 | Kriging: Concentration over the distance in %d',
year);
title(title_tekst2)
legend('Cis-1,2-Di-chloroethene','River Location','Location','best')

```

```

ylabel('Concentration (\mug/L)')
xlabel('Distance (m)')
set(gca,'YTickLabel',num2str(get(gca,'YTick').'))
hold off

figure(3), hold on
pltX_PER = plot(x(2:N+2),c_PER(2:N+2,year_fig),'b-');
pltX_TRI = plot(x(2:N+2),c_TRI(2:N+2,year_fig),'y-');
pltX_CIS = plot(x(2:N+2),c_CIS(2:N+2,year_fig),'m-');
pltX_VC = plot(x(2:N+2),c_VC(2:N+2,year_fig),'c-');
pltX_ET = plot(x(2:N+2),c_ET(2:N+2,year_fig),'r-');
xlim([0, x((length(x)-1))])
legend('Tetrachloroethene', 'Trichloroethene', 'Cis-1,2-Di-chloroethene', 'Vinyl
Chloride', 'Ethene', 'Location', 'best')
ylabel('Concentration (\mug/L)')
xlabel('Distance (m)')
set(gca,'YTickLabel',num2str(get(gca,'YTick').'))
hold off

Chosen_distance = 175; %Specified distance of interest to plot
Distance_point = find(x(2:N+2)>Chosen_distance,1,'first')+1; % Integer value in the
array/matrix coinciding with the specified distance
Distance_travel = x(Distance_point); % Distance travelled of the flowline coinciding
with the integer value (m)
distance_plot = Chosen_distance; % Number of specified distance to be inserted in
title

figure(4), hold on
pltT_PER = plot(year_start+(t/365.25),c_PER(Distance_point,:), 'b-');
pltT_TRI = plot(year_start+(t/365.25),c_TRI(Distance_point,:), 'y-');
pltT_VC = plot(year_start+(t/365.25),c_VC(Distance_point,:), 'c-');
pltT_ET = plot(year_start+(t/365.25),c_ET(Distance_point,:), 'r-');
xlim([year_start 2066])
xaxis = [2004 2010 2016 2026 2036 2046 2056 2066];
title_tekst3 = sprintf('Flowline 1 | Kriging: Concentration over the time at %d meters',
distance_plot);
title(title_tekst3)
legend('Tetrachloroethene', 'Trichloroethene', 'Vinyl Chloride',
'Ethene', 'Location', 'best')
ylabel('Concentration (\mug/L)')
xlabel('Time (years)')
set(gca,'YTickLabel',num2str(get(gca,'YTick').'))
set(gca,'XTick',xaxis)
set(gca,'XTickLabel',[2004 2010 2016 2026 2036 2046 2056 2066])
hold off

figure(5), hold on
pltT_CIS = plot(year_start+(t/365.25),c_CIS(Distance_point,:), 'm-');
xlim([2004 2066])
ylim([0 inf])
xaxis = [2004 2010 2016 2026 2036 2046 2056 2066];
title_tekst4 = sprintf('Flowline 1 | Kriging: Concentration over the time at %d meters',
distance_plot);
title(title_tekst4)
legend('Cis-1,2-Di-Chloroethene', 'Location', 'best')
ylabel('Concentration (\mug/L)')
xlabel('Time (years)')
set(gca,'YTickLabel',num2str(get(gca,'YTick').'))

```

```

set(gca,'XTick',xaxis)
set(gca,'XTickLabel',[2004 2010 2016 2026 2036 2046 2056 2066])
hold off

figure(6), hold on
pltT_PER = plot(year_start+(t/365.25),c_PER(Distance_point,:), 'b-');
pltT_PER = plot(year_start+(t/365.25),c_TRI(Distance_point,:), 'y-');
pltT_PER = plot(year_start+(t/365.25),c_CIS(Distance_point,:), 'm-');
pltT_PER = plot(year_start+(t/365.25),c_VC(Distance_point,:), 'c-');
pltT_PER = plot(year_start+(t/365.25),c_ET(Distance_point,:), 'r-');
xlim([year_start 2066])
legend('Tetrachloroethene', 'Trichloroethene', 'Cis-1,2-Di-Chloroethene', 'Vinyl
Chloride', 'Ethene', 'Location', 'best')
ylabel('Concentration (\mug/L)')
xlabel('Time (years)')
set(gca,'YTickLabel',num2str(get(gca,'YTick').'))
hold off

```

Generating Values for the distance distribution

```

limit = 0.1; % Detection limit of the measurements (mug/L)
Prob_point_PER = find(c_PER(2:N+2,year_fig)<limit,1,'first'); % Searching for the first
value below the detection limit.
if isempty(Prob_point_PER)==1 % In case there is no concentration below the limit
    Prob_point_PER = length(x)-2; % travelled distance is the max distance on the
flowline
end
Prob_dist_PER = x(Prob_point_PER +1); % Gathering the travelled distance data point
Prob_values_PER = [Prob_values_PER Prob_dist_PER]; % Saving all the travelled distances
from the simulations to one array.

Prob_point_TRI = find(c_TRI(2:N+2,year_fig)<limit,1,'first');
if isempty(Prob_point_TRI)==1
    Prob_point_TRI = length(x)-2;
end
Prob_dist_TRI = x(Prob_point_TRI+1);
Prob_values_TRI = [Prob_values_TRI Prob_dist_TRI];

Prob_point_CIS = find(c_CIS(2:N+2,year_fig)<limit,1,'first');
if isempty(Prob_point_CIS)==1
    Prob_point_CIS = length(x)-2;
end
Prob_dist_CIS = x(Prob_point_CIS+1);
Prob_values_CIS = [Prob_values_CIS Prob_dist_CIS];

Prob_point_VC = find(c_VC(2:N+2,year_fig)<limit,1,'first');
if isempty(Prob_point_VC)==1
    Prob_point_VC = length(x)-2;
end
Prob_dist_VC = x(Prob_point_VC+1);
Prob_values_VC = [Prob_values_VC Prob_dist_VC];

Prob_point_ET = find(c_ET(2:N+2,year_fig)<limit,1,'first');
if isempty(Prob_point_ET)==1
    Prob_point_ET = length(x)-2;
end
Prob_dist_ET = x(Prob_point_ET+1);
Prob_values_ET = [Prob_values_ET Prob_dist_ET];

```


end

Probability Distribution Figures

```
figure (7)
hold on
pd_PER = fitdist(transpose(Prob_values_PER),'kernel','kernel','normal','Bandwidth',6);
pd_TRI = fitdist(transpose(Prob_values_TRI),'kernel','kernel','normal','Bandwidth',6);
pd_CIS = fitdist(transpose(Prob_values_CIS),'kernel','kernel','normal','Bandwidth',6);
pd_VC = fitdist(transpose(Prob_values_VC),'kernel','kernel','normal','Bandwidth',6);
pd_ET = fitdist(transpose(Prob_values_ET),'kernel','kernel','normal','Bandwidth',6);

x_pdf = 0:1:400;
y_PER = pdf(pd_PER,x_pdf);
y_TRI = pdf(pd_TRI,x_pdf);
y_CIS = pdf(pd_CIS,x_pdf);
y_VC = pdf(pd_VC,x_pdf);
y_ET = pdf(pd_ET,x_pdf);

plot(x_pdf,y_PER,'Color','b')
plot(x_pdf,y_TRI,'Color','y')
plot(x_pdf,y_CIS,'Color','m')
plot(x_pdf,y_VC,'Color','c')
plot(x_pdf,y_ET,'Color','r')
line([320.8835 320.8835],[0 0.07],'Color','k','Linewidth',1,'LineStyle','--')
line([0 400],[0 0],'Color','k','Linewidth',2)
legend('Tetrachloroethene', 'Trichloroethene', 'Cis-1,2-Di-Chloroethene', 'Vinyl Chloride',
'Ethene', 'Average River Location','Location','best')
ylabel('Probability (-)')
xlabel('Travelled distance (m)')
title_text_prob = sprintf('Flowline 1: Probability of the travelled distance in %d', year);
title(title_text_prob)

hold off
```

Published with MATLAB® R2016a

This Page is Intentionally Left Blank



AFVALZORG

